Diversity of compressional mechanisms among SiO_2 polymorphs: case of coesite and cristobalite

Der Bayreuther Graduiertenschule für Mathematik und Naturwissenschaften

zur Erlangung der Würde eines
Doktors der Naturwissenschaften
- Dr. rer. nat. -

Dissertation

vorgelegt von
Ana Černok, MSc
aus Pančevo (Serbien)

Bayreuth, 2015

Die vorliegende Arbeit wurde in der Zeit von Juli 2011 bis Juni 2015 in Bayreuth am Lehrstuhl Bayerisches Geoinstitut (BGI) unter Betreuung von Herrn Professor Dr. Leonid Dubrovinsky angefertigt.

Vollständiger Abdruck der von der Bayreuther Graduirtenschule für Mathematik und Naturwissenschaften (BayNAT) der Universität Bayreuth genehmigten Dissertation zur Erlangung des akademischen Grades eines Doktors der Naturwissenschaften (Dr.rer.nat.).

Dissertation eingereicht am: 11.06.2015

Zulassung durch das Leitungsgremium: 12.06.2015

Wissenschaftliches Kolloquium: 10.12.2015

Amtierender Direktor: Prof. Dr. Stephan Kümmel

Prüfungsausschuss:

Prof. Dr. Leonid Dubrovinsky	(Erstgutachter)
Prof. Dr. Falko Langenhorst	(Zweitgutachter)
Prof. Dr. Daniel Frost	(Vorsitz)
Prof. Dr. Sander van Smaalen	

"We shall not cease from exploration. And the end of all our exploring will be to arrive where we started and know the place for the first time."

T. S. Eliot

ACKNOWLEDGMENTS

I am thankful to my supervisor Prof. Leonid Dubrovinsky for making it all possible and for showing extreme patience throughout this time. Although it has not been the smoothest road for either of us, I hope it has rewarded us both with useful experiences. To Prof. Natalia Dubrovinskaia I want to thank for the opportunity to have a nice overseas collaboration. Dear collaborators who helped throughout the projects are greatly acknowledged for all their contributions, discussions and help in analyzing data and reading the drafts: Razvan, Elena, Hanns-Peter, but most of all Tiziana, whom I cannot thank enough for her unreserved engagement. Tinka, thank you so much for accepting to deal with my frustrating samples and not to give up on them! That has revived my enthusiasm! Many people make scientific work at BGI easier by offering their unselfish help, whom I would like to acknowledge: Alex, Sven, Hubert, Rafael, Andreas, Nobu, Stefan, Lydia and Petra.

My PhD was initially financed by The Elite Network of Bavaria, within the program *Oxides*, to whom I thank for all the support, including travels and useful soft skill courses. During this period Prof. Hans Keppler, as a member in my committee, was very helpful in communing difficulites and progress of the thesis. Last several months of my thesis were made possible by the support provided by the University of Bayreuth Graduate School (*Feuerwehrfonds*), as well as by the research and travel stipend arranged by the Women´s representative & Equal Opportunities Department of the University of Bayreuth. I would like to express my deepest gratitude to Dr. Thomas Gollan from the *Feuerwehrfonds* for all his kindness and help, when it was burning the most! It gave me the opportunity to finish the most exciting part of my PhD. I sincerely appreciate all the patience and help I received from Mr. Christian Wagner from the Foreign Office in Bayreuth (Ausländeramt) in numerous visa issues I had throughout my stay.

Bayreuth has been *my village* and I have been living here so gladly over the past four years. It always felt like coming back home whenever I was on a bus or a train approaching Bayreuth. This period has not only brought numerous dear colleagues who made my time spent at BGI more pleasant, but it also turned some of them into good friends. Giovanni, Asyie, Mattia, Kanchana, Natalia, Matteo, Riko, and Ines (in the order I met you ☺), thank you for creating the good spirit and making the time spent here feels like an adventure colored by green in springs and white in winters. I bring with me some great memories of us going skiing, kayaking, hiking, biking, or simply drinking & dining and chatting. My hope is that I have managed to be a good friend to you as well, and I would be very happy to make it last after the *Bayreuther Zeiten* are over. The often monotonous University life was *charged balanced* with friends I met by actually taking some free time in life! Sara City, Oxsana & Fan, *motshakeram* for introducing me to the world of belly dance and sharing the positive energy anywhere you are! Kati za Zvati, *asante* for many unforgettable moments and stories we have been through together! Nebojsa, Blanca and David, *hvala* for establishing sort of Serbian kafana in the neighborhood from time to time!

The last, but not the least, I want to say **Thank you!** for all the support by distant friends, not only regarding my PhD time but also throughout the past ten years since I moved abroad. It is you who make me feel at home anywhere I go, may it be Pančevo, Belgrade, Vienna or New York. Thank you for making it true that devoted friendships can grow over distance and time. I might not have always said the exact words, but I truly admired each and every occasion on which we spent some quality time toghether. Feeling welcomed whenever I come (back), or keeping in touch meanwhile – this is what means *The World* to me! The list of your names would be way too long to write here, kind of showing off how many dear friends I have seeded around the globe☺! But if these words have touched your heart, then you know for sure you have been fullfilling mine over the past decade. **Thank you!**

My dearest aunt Magda and closest uncle Dragutin, who now live oceans away, have been encouraging me by setting good examples ever since my childhood when we all lived few blocks away. I am very devoted to them and here I would love to express my deepest gratitude for all their kindness.

I feel glad for coming to an end of what is considered the final step in formal education. The past four years were a challenging roller-coaster in many segments of my life. I particularly cherish these years for making it an experience I could have hardly imagine having, and most certainly an experience I would have likely chosen to skip if only I had known the way it will go. But having it now behind me, I feel rewarded with the most valuable lesson there is to learn: by going through the circumstances we perceive as undesirable we learn to grow within ourselves and to pay attention to beautiful and important qualities of life. Only by stepping out of our comfort zone we break free and, eventually, we find our peace by turning unpleasant fears into comfortable reality. **Metta**.

"Well if you can't get what you love
You learn to love the things you've got
If you can't be what you want
You learn to be the things you're not
If you can't get what you need
You learn to need the things that stop you dreaming
All the things that stop you dreaming

(...and make you live Here and Now ☺)"

Passenger

Dedicated to my family

Ima već nešto duže od 10 godina kako sam se upustila u avanturu, napustivši svoju zemlju u traganju za onim što se uz ove reči ostvaruje. No, ovaj poslednji deo puta nije ni po čemu veći niti važniji od starih raskrsnica i staza koje su do njega dovele. Ja sam od onih kojima se odabir zanimanja s izuzetnom lakoćom iznedrio još u najranijem detinjstvu. Izbor moje profesije zapravo nikada i nije bio izbor, već prirodan i iskren sled najranije radoznalosti. To moje zanimanje, nauka, gologija, isto je ono bezimeno zanimanje koje sam još kao dete imala u dvorištu naše porodične kuće u Prolom Banji. Moji baka i deka su gotovo celo dvorište udomili tako što su prostor oteli od gromada stena. A danas toj steni znam i ime – zove se andezit i iz nje potiču izvori lekovite Prolom vode. Odrastanje u Prolom Banji je za mene imalo razmere svojevrsnog carstva u kojem se život odvijao u potpunom skladu sa prirodom. Sve drugo što bih rekla bilo bi manje blizu istine – moje detinjstvo je bilo čarobno. I iz njega su ostali putokazi kojima sam se u svakoj narednoj etapi odrastanja uvek vodila, i s lakoćom vraćala onda kad bih izgubila samopouzdanje. Čini mi se da sam usidrena u svojim najranijim igrarijama plovila u sve većim koncentričnim krugovima – Petnica, Beč, Bajrojt, USA & Japan – uvek kretajući sa istog izvora. Tako je moje detinjstvo u Prolomu ostalo trajni odraz inspiracije i entuzijazma.

Rad posvećujem onima koji su mi sve ovo omogućili:

Mojoj mami Dragici i mom bratu Vladimiru,

Sa najdubljim poštovanjem mom deki Milivoju,

I sa čarobnim sećanjem na moju baku Ljubicu.

"Čovjek nije drvo, i vezanost je njegova nesreća, oduzima mu hrabrost, umanjuje sigurnost…U tome i jeste sve – vraćati se! S jedne tačke na zemlji čeznuti, polaziti i ponovo stizati. Bez te tačke za koju si vezan, ne bi volio ni nju ni drugi svijet, ne bi imao odakle da pođeš jer ne bi bio nigde. A nisi nigde ni ako imaš samo nju. Jer tada ne misliš o njoj, ne čezneš, ne voliš. A to nije dobro. Treba da misliš, da čezneš, da voliš. Onda, spremi se na put…jer je čovjek mlad sve dok se ne boji da započne!"

Derviš i smrt (Hasan)

ABSTRACT

Silica, SiO_2, exists in a wide range of pressure and temperature conditions, accommodating its simple chemical composition by numerous polymorphs. More than 30 stable or metastable phases of silica are known, most of which occur at ambient to moderate pressures (<9 GPa). Understanding polymorphism and densification mechanisms in silica is not only important from a geomaterial point of view, but it also has relevant implications in material sciences, technology and industry (glass, ceramics, etc.). The pathways of phase transitions are often influenced by thermodynamically metastable polymorphs that intermediate or hinder formation of thermodynamically stable phases.

This work is focused on understanding high pressure behaviour of two important silica minerals, coesite and cristobalite. Both of them are framework silicates comprised of fully polymerized corner sharing SiO_4 tetrahedra. Coesite, thermodynamically stable above ca. 2.5 GPa and at temperatures in excess of 500 °C, hereafter referred to as coesite-I, is the densest known polymorph with silicon atoms tetrahedrally coordinated to oxygen. It can be found as a high-pressure mineral in rocks related to meteorite impact sites, in ultra-high pressure metamorphic rocks or in kimberlites (mantle derived rocks). Cristobalite is a high-temperature (> 1470 °C), low-pressure polymorph of silica that has a subordinate and rather exotic terrestrial occurrence among silica phases (volcanic rocks, chert, etc.), but it is the predominant SiO_2 polymorph in various planetary materials (meteorites, lunar rocks, interplanetary dust particles, etc.). Exact pathways of pressure-induced transitions in coesite and cristobalite, as well as the structures of their high-pressure polymorphs have been poorly understood until now, despite being investigated by a number of studies over the past 30 years.

In this study, the response of coesite and cristobalite to compression was investigated at pressures exceeding 50 GPa using diamond-anvil cells by means of *in situ* Raman spectroscopy, synchrotron single-crystal X-ray diffraction, and analyses of the recovered samples by various techniques. Structural and Raman spectroscopic studies reveal that coesite-I (monoclinic *C*2/c, *Z*=16) undergoes two phase transitions (I->II->III) and does not become amorphous at least up to ~51 GPa. A reversible, displacive phase transition to coesite-II *(P*2_1/n*)* near 23 GPa is likely driven by the extreme shortening (0.05 Å or 3.2%) of the shortest and the most compressible Si-O bond, related to the stiff 180º Si-O-Si angle. The unit cell of the novel polymorph is doubled along the *b*-axis with respect to that of the initial coesite-I and contains all Si atoms in tetrahedral coordination. Further Si-O compression down to an extremely short distance of ~1.52 Å prompts subsequent structural changes, with the formation of a triclinic phase at ~31 GPa, coesite-III. The second transition (coesite-II to

coesite-III) is also reversible but with a large hysteresis. According to the abrupt change in Raman spectra this is likely a first order phase transition which leads to a very distinct structure with the lowest-symmetry. Despite all the efforts, the structure of the polymorph coesite-III remains unresolved. Samples recovered from the quasi-hydrostatic experiments carried out up to ~51 GPa, show the structure of the initial coesite, but those compressed between the diamond anvils (uniaxial stress) appear amorphous. The very short Si-O bond found in coesite-I and its high compressibility is a good example of how such bonds are restricted to the (almost) linear Si-O-Si geometry, and appear highly unfavorable in other Si-O-Si arrangements. Uncommon for other silica polymorphs, coesite-I demonstrates high-pressure behaviour governed by two simultaneous compressional mechanisms: polyhedral tilting along with Si-O-Si bond-angle reduction on the one hand and Si-O bond-length compression with polyhedral distortion on the other hand.

Regarding α-cristobalite, the study demonstrates that it responds differently to high pressures depending on the degree of the hydrostaticity. Under highly hydrostatic conditions, the initial structure of cristobalite is preserved. When the crystal experiences even slight stresses during an experiment, transformation sequence leads to cristobalite X-I at ~11 GPa – a monoclinic $P2_1/n$ polymorph with silicon atoms in octahedral coordination. The structure and formation of this novel polymorph was a long-standing enigma up to now. The likely reconstructive transition that involves increase in coordination number of silicon from four in cristobalite to its six-fold coordinated polymorph does not require any thermal activation; however, the high-pressure polymorph cannot be preserved at ambient conditions. No other silica polymorph was found to transform to an octahedra-based structure on cold compression at such low pressures (~11 GPa) and this structure could be accommodated in a (quasi)-hydrostatic environment where temperature is not sufficient to form the thermodynamically stable stishovite. In non-hydrostatic conditions in the presence of uniaxial stress, cristobalite eventually transforms to seifertite-like SiO_2, which is quenchable. Thus, according to our results, presence of seifertite may not always require the minimum shock pressures equal to that of thermodynamic equilibrium (~80 GPa) as it can be clearly formed at much lower pressures.

Both coesite and cristobalite follow the same densification path initially by undergoing a displacive phase transition to a slightly distorted structure of reduced symmetry. The most striking difference in response to compression of coesite and cristobalite is their reaction to (uniaxial) stress: coesite becomes amorphous when compressed in non-hydrostatic conditions; cristobalite, on the other hand, transforms directly to quenchable seifertite, a post-stishovite polymorph of silica. This may have important implications on occurrence and preservation of coesite and cristobalite in natural samples which have been exposed to non-hydrostatic compression, such as impact-related terrestrial rocks or

shocked meteorites. Crystalline or amorphous metastable phases derived from coesite or cristobalite under high-pressure conditions are of particular interest because they are often used as potential tracers of peak transient pressures (stress) reached in processes such as impacts or faulting. The novel metastable polymorphs reveal compressional mechanism of silica minerals and set important constraints on the very complex phase diagram of SiO_2.

ZUSAMMENFASSUNG

Trotz seiner einfachen chemischen Zusammensetzung zeigt Silizium-dioxid, SiO_2, eine Vielfalt an Polymorphen in einem breiten Druck-Temperatur Bereich. Mehr als 30 verschiedene Polymorphe sind bei niedrigen bis mäßigen Drucken (< 9 GPa) bekannt. Die Mechanismen der Verdichtung und Polymorphentstehung unter hohen Drucken ist sowohl in den Geowissenschaften als auch in den Materialwissenschaften, sowie in industriellen und technologischen Anwendungen, wie zum Beispiel bei der Glass- oder Keramikherstellung von Bedeutung. Die Umwandlungswege und Bildung von thermodynamisch stabilen Phasen werden oft durch die Entstehung von metastabilen Polymorphen beeinflusst oder verhindert.

Diese Arbeit befasst sich mit dem Hochdruckverhalten zweier wichtiger SiO_2 Polymorphen, Coesit und Cristobalit. Beide Mineralien gehören zu der Gruppe der Gerüstsilikate, welche aus SiO_4 Tetraedern bestehen, die alle vier Sauerstoffatome mit den benachbarten Tetraedern teilen. Coesit (weiterhin als coesit-I bezeichnet) ist ab ca. 2.5 GPa und 500 °C thermodynamisch stabil und es ist das dichteste SiO_2 Mineral mit vierfach koordinierten Siliziumatomen. Coesit-I ist als Hochdruckmineral in Impaktgesteinen, hochdruck-metamorphen Geisteinen, oder Kimberliten (ultramafische Gesteine aus dem Oberen Erdmantel) vorhanden. Cristobalit ist ein Hochtemperatur- (> 1470 °C), Tiefdruckmineral das auf der Erde nur untergeordnet zu finden ist; zum Beispiel in Vulkaniten und Hornstein. Jedoch ist Cristobalit in verschiedenen außerirdischen Materialien, wie z. B. Meteoriten, Mondgesteinen und Interstellarer Staub das häufigste SiO_2 Polymorph. Obwohl das Hochdruckverhalten dieser zwei Mineralien über 30 Jahre untersucht wurde, sind weder die konkreten Umwandlungswege, noch die Strukturen von Polymorphen die unter hohem Druck entstehen bekannt.

Die Umwandlungen von Coesit und Cristobalit wurden in dieser Arbeit mit Hilfe Experimenten in Diamantstempelzellen bei Drucken von mehr als 50 GPa bei Raumtemperatur untersucht. Die Hauptanalysemethoden die in dieser Studie genutzt wurden sind *in situ* Ramanspektroskopie und Einkristallstrukturanalyze mit Synchrotron-Röntgenbeugung. Die rückgewonnenen Proben wurden mittels verschiedenen Messverfahren analysiert. Ramanspektroskopische- sowie Röntgenbeugung-Untersuchungen an den Coesit-Einkristalle (monoklin *C*2/c, *Z*=16), zeigen zwei kristalline Phasenumwandlungen (I->II->III), die Amorphisierung bis mind. 51 GPa ausschließen. Der erste Phasenübergang zu Coesit-II ($P2_1/n$) findet bei ca. 23 GPa statt. Dabei handelt sich um eine reversible, displazive Umwandlung, die durch extreme Verkürzung (0.05 Å or 3.2%) der kürzesten und kompressibelsten Si-O Bindung, die an starrem 180° Si-O-Si Winkel verknüpft ist, verursacht

wird. Die Einheitszelle des Coesit-II wird dabei entlang der *b*-Achse im Vergleich zum Ausgangsprodukt verdoppelt. Alle Siliziumatome im Hochdruckpolymorph sind von vier Sauerstoffatomen umgeben. Weitere Verkürzung der Si-O Bindung auf ~1.52 Å resultiert in Coesit-III mit triklinischer Einheitszelle. Dieser Übergang findet bei ca. 31 GPa statt. Die Umwandlung ist reversibel, zeigt jedoch eine starke Hysterese. Die abrupte Veränderung des Ramanspektrums deutet auf eine Umwandlung erster Ordnung hin, wobei sich ein Polymorph mit deutlich verschiedener Struktur niedriger Symmetrie (Coesit-III) bildet. Trotz mehrfachen Versuchungen, wurde die Struktur dieses Polymorphen in dieser Studie nicht bestimmt. Die Produkte, die nach den quasi-hydrostatischen Hochdruckexperimenten geborgen wurden, zeigen die gleiche Struktur wie die Edukte, Coesit-I. Im Kontrast hierzu zeigen Kristalle, die bei Hochdruck Experimenten, in denen der Druck direkt zwischen zwei Diamanten aufgebaut wurde (d.h. unter uniaxialem Stress standen) keine kristalline Struktur.

Die kürzeste und kompressibelste Si-O Bindung im Coesit-I ist ein sehr wichtiges Beispiel dafür, dass solche Bindungen nur auf (fast) lineare Si-O-Si Ausrichtungen beschränkt sind, und in anderen Si-O-Si Konfigurationen nicht günstig sind. Das Hochdruckverhalten von Coesit-I ist durch zwei Kompressionsmechanismen gekennzeichnet, einerseits durch das Kippen von SiO_4 Tetraedern, ein typisches Verhalten in vielen SiO_2 Modifikationen, anderseits werden auch Si-O Bindungen stark verkürzt, was zur Verzerrung der Tetraeder führt.

Das Hochdruckverhalten vom Cristobalit ist von dem Grad der Druck-Hydrostasie abhängig. Unter hochhydrostatischen Bedingungen bleibt die Struktur von Cristobalite bis mindestens 15 GPa erhalten. Wenn die Bedingungen quasi-hydrostatisch werden und der Kristall unter minimalen Spannungen steht wandelt sich der tetragonale α-Cristobalite über Cristobalite-II in Cristobalit X-I bei ca. 11 GPa um. Das letzte Hochdruckpolymorph ist monoklin ($P2_1/n$) und besitzt Siliziumatome in oktaedrischer Koordination – jedes Si ist von sechs Sauerstoffatomen umgeben. Die Bildung und Struktur dieses Polymorphen waren ein lang-ungeklärtes Rätsel der Hochdruckforschung. Um die Siliziumkoordination von vier auf sechs zu erhöhen, ist bei dieser vermutlich rekonstruktiven Umwandlung keine thermische Aktivierung erforderlich. Jedoch ist das Hochdruckpolymorph bei Raumdruck nicht stabil und wandelt sich umgehend in α-Cristobalit um. Die Koordinationserhöhung von 4 auf 6 bei so geringem Druck (ca. 11 GPa) ohne Zufuhr von thermischer Energie ist bei keinem anderem SiO_2-Polymorph beobachtet worden. Solche Umwandlung könnte in einer quasi-hydrostatischen Umgebung stattfinden wo die Temperatur nicht ausreichend ist um thermodynamisch stabilen Stishovit zu bliden. In einer nicht-hydrostatischen Umgebung, unter einachsig gerichtetem Druck, wandelt sich Cristobalit schließlich in Seifertit (post-Stishovit Polymorph) um. Seifertit ist bei

Raumbedingungen metastabil konservierbar. Dieses ist ein wichtiger Hinweis dafür, dass Seifertit in stark geschockten Meteoriten nicht immer unter Gleichgewichts Bedingungen (> 80 GPa) gebildet werden muss.

Bei geringerem Druck zeigen Coesit und Cristobalit ähnliche Verdichtungsmechanismen,, Beide Polymorphe werden durch einen displazieven Phasenübergang zu dem jeweiligen Hochdruckpolymorph mit etwas verzehrter Struktur unter Symmetrieverringerung (Coesit-I bzw. Cristobalit-II) umgewandelt. Bei höheren Drucken folgt die Verdichtung auf unterschiedlichen Wegen, wobei der deutlichster Unterschied bei unaxialen Kompression zu beobachten ist: Coesit wird amorph, während Cristobalit sich direkt in Seifertit umwandelt.

Nicht-hydrostatische Kompression, wie zum Beispiel bei einem Impaktereignis im Meteoritenkrater oder in geschockten Meteoriten kann einen wesentlichen Einfluss auf die Erhaltung von Coesit und Cristobalit in natürlichen Proben haben. Das Verhalten dieser kristallinen oder amorphen metastabilen Polymorphen ist von Bedeutung, weil sie oft als Hochdruckindikatoren des Maximaldrucks in geologischen Prozessen wie Impakten oder Störungen, verwendet werden. Die neu-entdeckten Hochdruck-polymorphe liefern wichtige Information über Verdichtungsmechanismen in SiO_2 und liefern neue Randbedingungen für das komplexe SiO_2 Phasendiagram.

TABLE OF CONTENTS

1. INTRODUCTION

1.1 Silica

Silica is a broad name for compounds containing oxygen and silicon with the general formula SiO_2. Oxygen and silicon are the two most common elements on Earth, comprising ~30 wt% and ~16 wt% of it, respectively. Given that the Si-O bond is significantly stronger (466 kJ/mol) than the bond of any other element with oxygen (e.g. Putnis, 1992), it is understandable why SiO_2 is the dominant oxide constituent of the earth's crust (~60 wt %) and of the *Silicate Earth* (~45 wt %), which is the model composition of the crust and the mantle joined together, excluding the metallic core (McDonough & Sun 1995; McDonough 2001 and references therein). The most common element of the mantle after oxygen is magnesium, therefore reducing its bulk SiO_2 content. The leading oxide contributes not only to the pure or the so called "free silica" minerals, but also to the composition of all the rock-forming *i.e.* silicate minerals, which basically contain silicon-oxoanions, illustrated in Figure 1.1, charge balanced by different cations. Silicate minerals, including pure SiO_2 minerals, comprise 95 % of the Earth's crust (e.g. Putnis, 1992). Quartz (pure SiO_2) is the second most abundant mineral of the crust, comprising about 12 % of its volume, preceded by the group of feldspar minerals ($KAlSi_3O_8$–$NaAlSi_3O_8$–$CaAl_2Si_2O_8$), which constitute 59.5 % of it (e.g. Heaney 1994, and references therein). However, due to its high hardness (7 on the Mohs scale of 10) and low solubility in water, quartz is mechanically and chemically far more resistant to weathering than feldspar that eventually degrades to clay minerals. Therefore, quartz is abundantly enriched in various sedimentary environments. When such quartz rich continental sediments are subducted into the deep earth's interior, pure SiO_2 phases can comprise up to 20 volume % of the bulk mineral composition of the slab (Irifune et al., 1994). Similar outcome is seen for the subducted oceanic crust, which contains far less silica than the continents (e.g. Ono et al. 2001; Perrillat et al. 2006). The mantle surrounding the plunged slabs, however, is almost free of silica minerals.

The transformation process of silica under high pressures and temperatures has been of long and continuing interest due to its wide-ranging implications for geology, material sciences, technology and industry. Understanding of how the densification mechanisms in SiO_2 occur is important for understanding problems ranging from the constitution of the mantle and its transition zone, or amorphization during an impact event, or developing high-toughness ceramics (Huang et al., 2006).

1.2 The Si-O bond

The type of the crystal structure in a compound is related to the character of chemical bonding. Crystals with purely ionic or purely covalent bonds are very rare and vast majority of silicate minerals have complex structures with bonding character transient between ionic and covalent. Ionic structures are held together by non-directional electrostatic forces, with the atoms packed as if they were hard spheres that obey radius ratio rules. Covalent bonds are directional with electron density increasing along direction that connects the two bonding atoms. Covalent bonds are formed from the atoms that have both *s* and *p* valence electrons, i.e. the elements of the III-V group of the periodic table, with relatively high electronegativities.

Silica does not produce any separate molecules (O=Si=O), because double bonds do not form (Fanderlik, 1991). The Si-O bond can be considered both ionic and covalent in character (e.g. (Pauling, 1960, 1980). If the character of the Si-O bond was purely ionic, the oxygen ions would tend to be close-packed around positively charged Si^{4+} or any other cation in the structure of silicates. According to Pauling (1960), the value of the ionic radii ratio Si^{4+}/O^{2-} (0.38 Å/1.29Å = 0.29) implies the coordination number of silicon to be 4. However, very few silicates have sufficient densities to account for close-packed oxygen arrays. Additionally, the observed coordinations in silicates are not always consistent with the cation/oxygen radius ratios. Moreover, ionic bonding implies regions of zero electron density that should be found between Si^{4+} and O^{2-}, yet this has not been supported experimentally. Based on various electronegativity calculations, iconicity degree of the Si—O bond can vary between 35 and 50 % (Pauling, 1960,1980; Lakatos et al. 1959; Jatkar and Jyengar, 1949). In a covalent model, the Si-O bond is formed between hybridized 3*s* and 3*p* orbitals of silicon and 2*p* orbitals of oxygen. The electron configuration of the silicon atom is $1s^2\ 2s^2\ 2p^6\ 3s^2\ 3p_x^1 p_y^1$ or, in an excited state, $1s^2\ 2s^2\ 2p^6\ 3s^1\ 3p_x^1 p_y^1 p_z^1$. The four valence orbitals hybridize to form energy-equivalent sp^3-hybrid orbitals, separated by an angle of 109° 28' and directed towards the vertices of a tetrahedron, as illustrated in Fig 1.1. The oxygen atom ($1s^2 2s^2 2p_x^2 2p_y^1 2p_z^1$) utilizes particularly the non-pair $2p_y$ and $2p_z$ electrons for its bond formation, always one for each sp^3 electron of silicon atom (Rohrer, 2001) to form the $[Si^{4+}O^{2-}{}_4]^{4-}$ tetrahedron. Whereas the measurements have shown that the angle between the Si-O bonds in the elementary tetrahedron is stable (109° 28'), the angle of the Si-O-Si bond between the connected tetrahedra was found to range between 120° and 180° in various forms of silica. A number of theoretical models have proposed that Si-O-Si bond is affected by complex hybridization (e.g. *sp* and sp^2), that involves low-lying *d*-type orbitals on silicon. The theoretical models accounting for the complex hybridization on Si-O bond are summarized in Fanderlik (1991) and Gibbs et al. (1994). In conclusion, the stable intratetrahedral angle between the

Si-O bonds is, therefore, determined by sp^3 hybridization of the 3*s* and 3*p* orbits of the silicon atom, whereas the various sizes of the Si-O-Si bond angles are influenced by a complex case of sp^n hybridization in which the hybrid orbits are not equivalent.

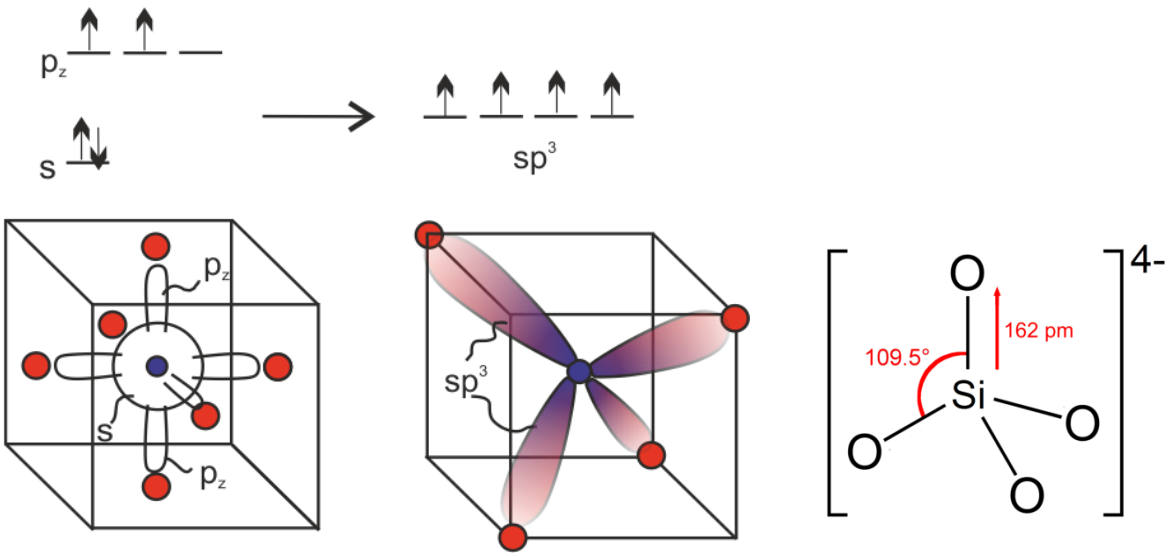

Figure 1.1. Illustration of silicon atom (blue sphere) and its orbitals energy levels before (left) and after (middle) sp^3 hybridization and the formation of chemical bond with oxygen (red spheres). The elementar tehtahedron, its formal charge and the bond length and angles are represented on the right.

1.2.1 The SiO_4 tetrahedron

SiO_4 tetrahedral units can join together by sharing oxygen atoms in a variety of ways to form chains, rings, sheets or three dimensional silicates. The basic classification of all rock-forming minerals is based on the arrangement of the SiO_4 tetrahedra – if they are isolated from other SiO_4 tetrahedra (and connected to polyhedra of different cations), or they are connected to each other by corner-sharing. No more than two tetrahedra can share a common corner i.e. bridging oxygen. The corner-sharing arrangement of the SiO_4 tetrahedra can be considered a skeleton of all rock-forming minerals, with other cations occupying suitable interstices.

The shape and size of the tetrahedron depend on the Si-O bond lengths and on the intratetrahedral O-Si-O bond angles. These have been determined for a large number of silicates by means of X-ray and neutron diffraction. The mean Si-O bond length is 1.62 ± 0.05 Å. Cations occupying interstices in the structures of silicates are likely to attract oxygen, thereby slightly increasing the length of the Si-O bond. The corner-linked tetrahedra share a Si-O-Si bond angle, which was experimentally determined and theoretically calculated to vary between 120° and 180°. Calculation of the potential energy

surface of an Si_2O_7 pair (two linked tetrahedra) as a function of the Si-O_{br} (bridging oxygen) bond length and the Si-O_{br}-Si angle (e.g. Gibbs et al. 1981, 1994, 2009) indicate that the angle is widening with decreasing Si-O_{br} bond length: the Si-O-Si bond angles close to 180° can be related to the bonds of less than 1.60 Å (see Chapter 5 on coesite). The Si-O bond length and the intratetrahedral O-Si-O angle appear very rigid, thus the expansion and contraction of the silicate structures are strongly dependent on the relatively adaptable intertetrahedral Si-O-Si bond angles.

In case tetrahedra are isolated from each other and do not share any oxygens, Si:O ratio is 1:4 (for example olivine Mg_2SiO_4). Silica phases are fully polymerized (so called tectosilicates): all tetrahedra share corners with other tetrahedra, a framework silicate is formed, with 4 bridging oxygens per tetrahedron and the Si:O ratio of 1:2, resulting in the stoichiometric formula SiO_2. Structures of coesite and cristobalite are illustrated in Figure 1.2. A general feature of framework structures is that they open and expand at high temperatures, giving rise to the maximal symmetry allowed by the tetrahedral linkages. At room temperature, these structures tend to collapse, thereby reducing the symmetry. This is largely accommodated by rotation of the tetrahedra and changes in the Si-O-Si bond angles.

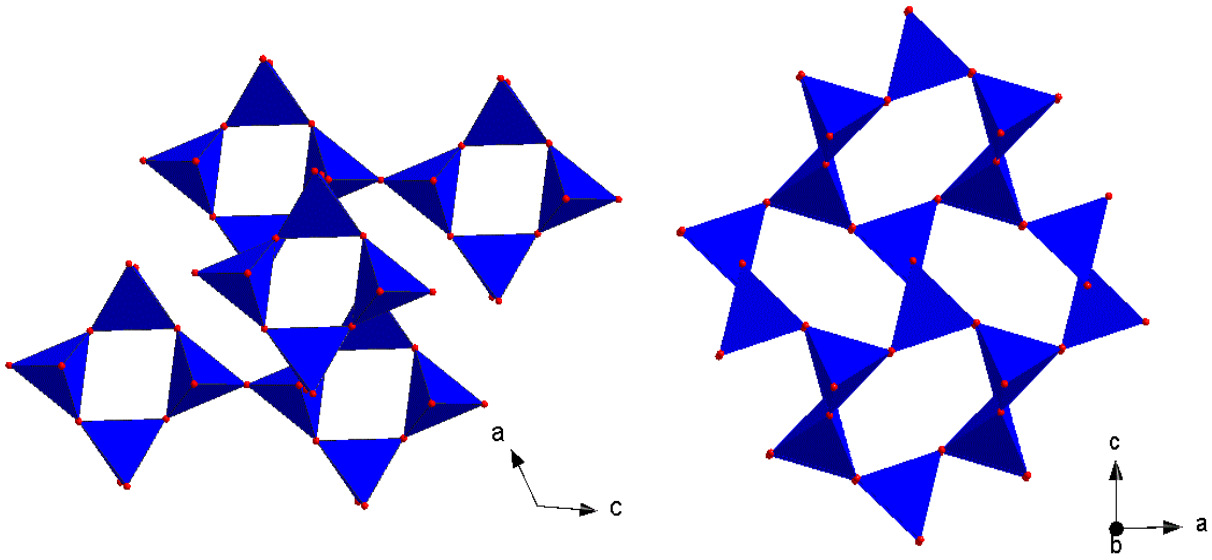

Figure 1.2. Polyhedral representation of coesite (left) and α-cristobalite structures at ambient conditions (red spheres are oxygen atoms). Coesite (space group *C*2/c) contains 4-membered rings of tetrahedra that are not interconnected within the same plane, but are connected to the plane above and below to form a crankshaft-like structure. Cristobalite (space group $P4_12_12$) contains 6-membered rings of tetrahedra. Coesite after (Angel et al., 2003) and cristobalite after Peacor, 1973.

1.2.2 The SiO_6 octahedron

The Si^{VI} configuration gives rise to a more ionic Si–O bond (Mitra, 2004). Although not commonly observed in the minerals that are found on the surface of the earth, Si^{VI} is common in organic compounds (Gibbs et al., 1994). Experimental data yield typical length of the Si-O bond in an octahedron in the range 1.70 – 1.84 Å. Numerous theoretical models suggested involvement of the *s*-, *p*- and *d*- orbitals in the complex hybridization in case of SiO_6 (Gibbs et al. 1994).

At the pressures and the temperatures typical of the crust and the upper mantle of the earth (< 200 km), silicate minerals contain SiO_4 polyhedron. Between 5-20 GPa (that corresponds to the depths which include the transition zone of the upper mantle at 440-670 km and the uppermost lower mantle) all common silicate minerals undergo phase transitions to structures that contain SiO_6. Some minerals in this region like majorite, pyroxene or wadeite etc., contain silicon in both four-fold and six-fold coordination (Finger and Hazen, 2000). At higher pressures and temperatures that are characteristic of the lower mantle lying deeper than 670 km, silicon increases its coordination number from four to six, and above 25 GPa, only Si^{VI} can be found. Changes of the structures with the *P*-*T* conditions of the earth's interior are illustrated in Fig. 1.3. Structures containing six-fold Si are also frameworks, in which the octahedra can be either corner or edge-linked. In spite of the variety of the octahedral linkages, the size and the shape of SiO_6 are very similar within all the compounds: mean Si-O bond distances vary within 2 %; polyhedral volumes within 4 % (Finger and Hazen, 1991, 2000).

Some theoretical calculations predict pentacoordinated silicon (e.g. Badro et al. 1997). The Si^{V} was confirmed in case of other common silicates (Angel et al., 1996). However, the experimental determination of Si^{V} in pure silica (Luo et al. 2004) have not been unambiguous.

1.3 Equilibrium phase relations in SiO_2

The discovery of crystal X-ray diffraction by Max von Laue in 1912 led to the first attempts in studying the structure of rock-forming minerals. Within only few years these pioneering attempts determined structures of the best known minerals, such as diamond, calcite, pyrite, halite, etc. and in the decades to follow immense progress was made in characterizing dozens of other minerals (Bragg, 1937). Notably, already the earliest crystallographic efforts indicated that the silica system, albeit having a very simple chemical composition, shows high structural complexity manifested by prolific polymorphism. It was the observation that the most common silica minerals – quartz, cristobalite and

trydimite – undergo modifications at high temperatures which increase their symmetry, thereby reducing the number of structural parameters to be determined, that allowed scientists to reveal the structure of these minerals: first of the high-temperature, the so-called *β*-polymorphs and then later of their low-T, i.e. *α*- counterparts. (e.g. Bragg and Gibbs, 1925, summerized in (Heaney, 1994).

Today, more than 30 stable or metastable silica phases are known to occur at ambient to moderate pressures up to ~9 GPa (Heaney, 1994; Hemley et al., 1994; Haines et al., 2001). Their structures can be described as open frameworks comprised of fully polymerized corner-sharing SiO_4 tetrahedra. Among them, only α-quartz is thermodynamically stable at the surface of the Earth (Fig. 1.3), however many others can be metastably preserved at ambient conditions – e.g. trydimite, cristobalite, coesite, etc.

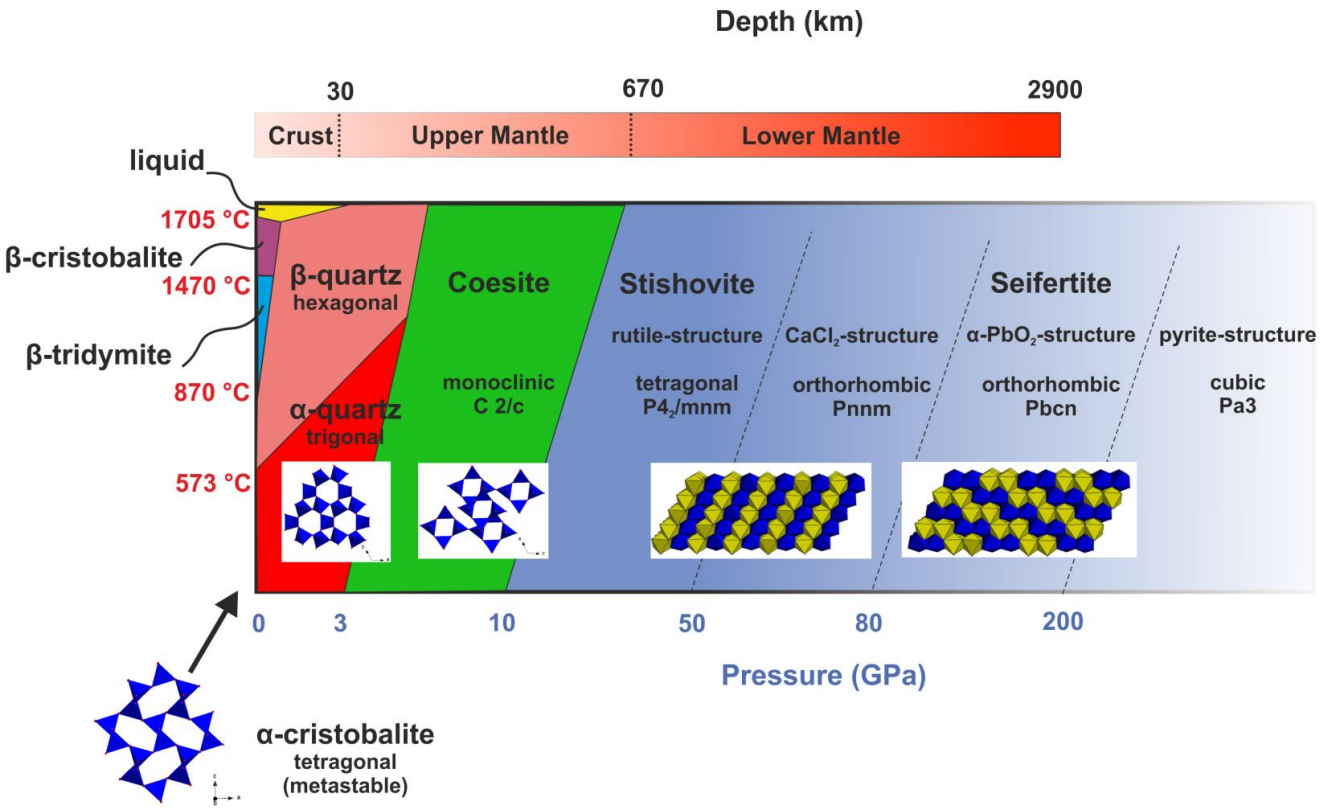

Figure 1.3. A schematic phase diagram of silica. Thermodynamical stability fields in the lower pressure segment, up to the rutile-$CaCl_2$ phase boundary are realistic (e.g. Heany, 1994). Phase boundaries at higher pressures $CaCl_2$-α-PbO_2-Pa3 are schematic according to the experimental data (summarized in Driver et al. 2010). Structures according to: quartz (Glinnemann et al., 1992); cristobalite (Peacor, 1973); coesite (Angel et al., 2003); stishovite and seifertite (Dubrovinsky et al., 2004).

Low– or α-quartz (trigonal) transforms to the hexagonal high- or β-quartz at 573 °C (at room pressure), then further to β-trydimite (hexagonal) at 870 °C, and finally to β-cristobalite (cubic) at 1470 °C. Melting of β-cristobalite takes place near 1700 °C at room pressure. The transformations between the α-β forms are displacive and do not require any Si-O bond breaking, only the rotation of the tetrahedra and changes in the Si-O-Si bond angles. However, the structures of quartz, trydimite and cristobalite are quite distinct and each of them represents a different arrangement of the linked tetrahedra. Tre transformations between these three polymorphs are reconstructive and require a lot of energy in order to break and re-arrange strong Si-O bonds. Therefore, β forms of trydimite and cristobalite very often transform to their symmetry-reduced α-counterparts upon quick cooling, even though the α-forms are metastable. The transition to the stable α – quarz is hindered due to the high energetic barrier and can be overcome only by sufficiently slow cooling. This is the reason why we find α-trydimite (orthorhombic) and α-cristobalite (tetragonal) related to igneous or volcanic rocks. It is important to note, however, that at ambient conditions trydimite can exist in six different forms which have very distinct structures and are commonly intergrown in a complex manner (e.g. Pryde & Dove 1998). Densities of these minerals are: quartz 2.65 (2.53), trydimite 2.26 (2.22), cristobalite 2.32 (2.20) g/cm^3, with density of β-forms in parentheses. In addition to the earth's surface, α-quartz is the predominant silica polymorph throughout the crust and uppermost mantle. At higher pressures the structure of low-quartz is more stable relative to that of high-quartz and much more energy (temperature) is required for the transformation to the high-temperature phase (e.g. Heany 1994).

Naturally occurring high-pressure silica polymorphs are represented by coesite (monoclinic), stishovite (tetragonal) and recently described seifertite (orthorhombic). Above ~2 GPa silica takes the structure of coesite – the densest polymorph that contains silicon in tetrahedral site (2.98 g/cm^3). The phase transition quartz-coesite is also reconstructive (Akaogi et al., 1995; Dmitriev et al., 1998). Coesite is associated with rocks excavated from depths of 100-300 km (upper mantle), corresponding to the pressure range of 3-10 GPa. No silica polymorphs denser than coesite have ever been found in any exhumed rocks on Earth (Goresy et al., 2008). Coesite was also documented in rocks related to impact craters (e.g. Chao et al. 1960) or in heavily shocked meteorites of various kinds (e.g. Ohtani et al. 2011). Above ~ 10 GPa stishovite (tetragonal) is formed, with the density 46% higher than that of coesite. This transition is sometimes related to the seismic X-discontinuity at 250-350 km (e.g. Chen et al., 2015). Stishovite can be found in terrestrial impact-related rocks, as well as in shocked meteorites. At the earth's lower mantle (pressures exceeding 25 GPa), all silicates and not only pure silica minerals are observed to transform to dense structures in which all Si are six-coordinated (Mitra, 2004). At pressures above 45-55 GPa and ambient temperature tetragonal stishovite

undergoes orthorhombic distortion and displacively transforms to a $CaCl_2$-type structure. This phase boundary has been extensively studied by numerous experimental and theoretical groups (Andrault et al., 2003, 1998; Asahara et al., 2013; Driver et al., 2010; Dubrovinsky and Belonoshko, 1996; Shigeaki Ono, 2002; Tsuchida and Yagi, 1989; Tsuchiya et al., 2004; Yang and Wu, 2014). The interest arises from the fact that this transition was suggested as an explanation for several seismic discontinuities observed in the mid-lower mantle (1000-1600 km), however no real agreement was achieved. The $CaCl_2$-type structure is not quenchable and it was never observed in nature. The high-pressure transition from $CaCl_2$ to α-PbO_2 (seifertite) structure is predicted to occur above 80 GPa according to (Andrault et al. 1998; Teter et al. 1998) but it was experimentally evidenced that the $CaCl_2$ structure is stable to at least 120 GPa (Andrault et al., 1998; Dubrovinsky et al., 1997). The phase boundaries in the post-stishovite range are still very unclear, arising from contradictory experimental results. Seifertite is the densest form of silica occurring in nature. It was discovered in heavily shocked Martian meteorites (Goresy et al., 2008; Sharp et al., 1999), and only very recently also recognized in a lunar meteorite (Miyahara et al., 2013). The stability field of seifertite is expected in the lowermost portion of the mantle, above 120 GPa. At pressures exceeding those of the Earth's interior and corresponding to giant rocky or icy planets, for example Uranus or Neptune, silica phases can exist in structures with silicon having coordination higher than 6. The pyrite-type structure was experimentally obtained above 260 GPa (Kuwayama et al., 2005); in this structure silicon is surrounded by 6+2 oxygens. However all other structural types that exist at significantly higher pressures can only be addressed by means of theoretical calculations (e.g. Tsuchiya & Tsuchiya 2011).

1.3.1 Occurrences of cristobalite and coesite

Coesite was first observed experimentally by Coes in 1953 and later discovered in nature by Chao and coworkers, in impact breccia from Meteor Crater (Chao et al. 1960). Nowadays coesite is widely accepted as a high-pressure indicator in rocks related to meteorite impact sites, where quartz transforms to coesite due to the high-pressure and high-temperature regime of the impact and to the very rapid quenching conditions which prevent a reversion to quartz (e.g. Xiao et al., 2011). Shock-induced formation of coesite has been also observed in meteorites, where it can be found along with other shock minerals (e.g. Ohtani et al., 2011). Terrestrial occurrence of coesite was reported from deeply (>100 km) subducted crustal rocks (ultra-high pressure metamorphic rocks) or mantle derived rocks (kimberlites), which have been exhumed under conditions that prevent retrograde transition to quartz (e.g. Smyth and Hatton, 1977; Chopin, 1984; Smith, 1984; Korsakov et al., 2007; Mosenfelder and Bohlen, 1997; Ruiz-Cruz and Sanz de Galdeano, 2012; Sobolev et al., 2000). The metastable

persistence of coesite up to surface conditions is commonly the result of their inclusion in mechanically strong host minerals like garnet, zircon or diamond, which act as pressure vessels (e.g. Sobolev et al., 2000). In the UHP rocks, coesite is formed in static pressure environment and by a solid-state transformation. On the contrary, coesite found in impact related rocks crystallized from a melt at high *PT* conditions (e.g. Chen et al., 2010). More details on its structure are given in Chapters 4 and 5.

Cristobalite is a silica polymorph that forms at low-pressures and at variable temperatures: tetragonal α-cristobalite can be formed upon cooling of *β*-cristobalite at temperatures lower than ~250 °C. Low temperature phase is far more common and it is often reported in volcanic rocks and ashes of intermediate and acidic composition (e.g. Horwell et al., 2012), or sometimes in basaltic rocks (Van Valkenburg and Buie, 1945). Natural α-cristobalite can be found as constituent of opal-CT, which is an intermediate product in diagenesis of marine sediments (e.g. Gaillou, 2008). Rare appearance of α-cristobalite is related to ~5 terrestrial impact sites, where it was observed in the so called ballen – spheroidal forms comprised of crystallites of quartz and/or cristobalite (Ferriere et al., 2009). In contrast to its subordinate and rather exotic terrestrial occurrence among silica phases, cristobalite is the predominant SiO_2 polymorph in various planetary materials. IR spectra emitted from the protoplanetary disks surrounding young, "pre-hydrogen-burning" T Tauri stars, show prominent features of silica that are best fitted by cristobalite, possibly associated with trydimite (Koike et al., 2013; Sargent et al., 2009). As inferred by the meteoritic record, examples of cristobalite occurrences are numerous. Chondrules, the early solar condensates and constituents of the chondirtic meteorites, although not primarily comprised of silica, demonstrate a rare type (< 2%) named silica-bearing chondrules that are comprised of up to 40 wt % of SiO_2, in most cases identified as cristobalite (e.g. Brearley and Jones, 1998). Apart from chondrules, cristobalite is found as an accessory mineral in the matrix of various chondrites (summarized by Brearley and Jones, 1998). Lunar basalts contain silica as accessory (~1 % of volume) phase, with cristobalite and trydimite dominating better than 99 % of it (e.g. Rasmussen et al., 2008).

1.4 Metastability of silica polymorphs under high-pressures

Framework oxides with polyhedral building blocks often possess significant capacity for densification under pressure owing to their open structures (Huang et al., 2006). Despite its simple chemical composition, silica shows rich polymorphism at elevated pressures (e.g. Dubrovinsky et al., 2004; Martoňák et al., 2007; Teter et al., 1998). High-pressure behaviour of framework structures largely depends on the way in which the polyhedra are linked together, particularly in the corner-sharing tetrahedral structures. The volume decrease in silica framework structures is achieved by rotation rather than distortion of tetrahedra, because the forces within individual tetrahedra are much stronger than the forces between them (e.g. Ross, 2000). These mechanisms lead to volume reduction, crystalline-crystalline phase transitions, or to amorphization i.e. loss of the long-range crystalline order. The complexity of pressure-created polymorphs in silica is illustrated in Figure 1.4. Reconstructive transitions to stable high-pressure phases consisting of SiO_6 octahedra (e.g. stishovite, $CaCl_2$-structured silica, or seifertite) are often hindered due to high kinetic barriers associated with the relatively strong Si-O bonding within tetrahedra (Haines et al. 2001). As a consequence, compression of tetrahedral phases without sufficient temperature supply results in complicated metastable relations, such as the persistence of low-pressure tetrahedral phases far out of their stability fields.

1.4.1 Quartz & trydimite

Being the most common silica mineral, **quartz** has been a subject of numerous high-pressure studies by means of experimental and computational work. Compressional behaviour of α-quartz was established based on numerous single crystal XRD studies (Levien et al. 1980; Hazen et al. 1989; Glinnemann et al. 1992; Kim-Zajonz et al. 1999) up to maximal 19.3 GPa. At higher pressures various techniques were used to describe high-pressure behaviour in which pressure-induced phase transition to the monoclinic phase of $P2_1/c$ symmetry (Haines et al., 2001) and the onset of amorphization (Kingma et al., 1993) was observed. **Trydimite** high-pressure behaviour has not been investigated as much experimentally and the reason for this is its enhanced metastability (six polymorphs) at ambient conditions. Only few studies are available, in which it was reported that monoclinic trydimite undergoes phase transformation near 5 kbar (Nukui et al., 1980; Pryde and Dove, 1998).

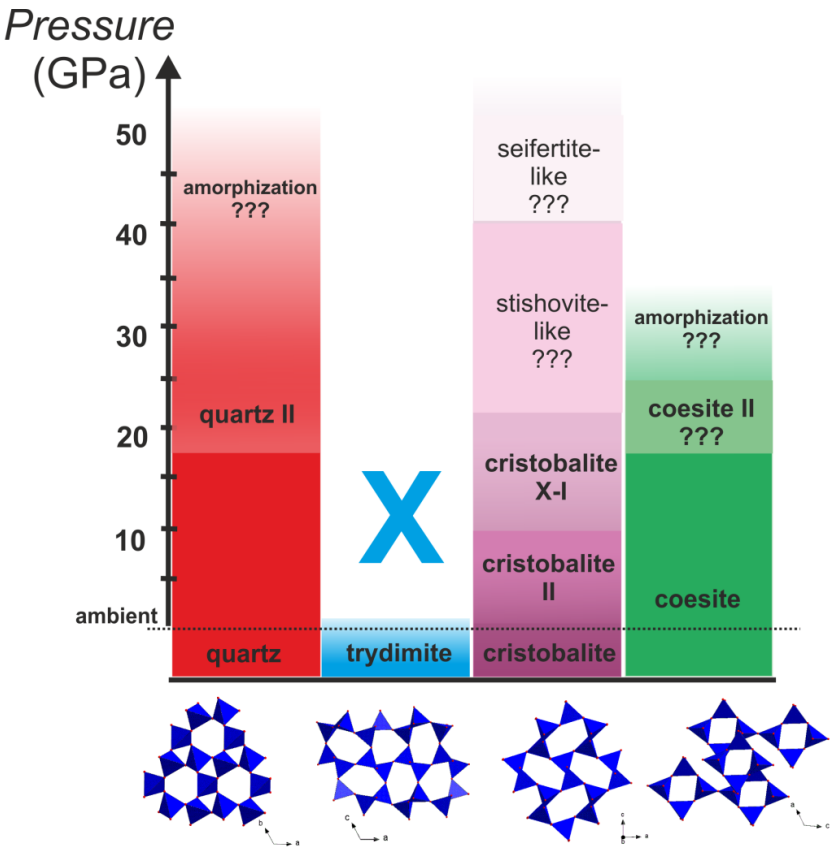

Figure 1.4. Schematic pathways of pressure-induced polymorphism starting from various tetrahedral SiO_2 phases. Structures are illustrated for comparison of their characteristic rings. Question marks present regions of uncertain behaviour or formation of a new polymorph with unknown structure. References are given in appropriate sections. Structures according to: quartz (Glinnemann et al., 1992); cristobalite (Peacor, 1973); coesite (Angel et al., 2003); monoclinic tridymite (Kihara et al., 2005).

1.4.2 Coesite

The high-pressure structural behaviour of coesite was previously studied using in-house based single crystal X-ray diffraction up to 5.2 GPa (Levien and Prewitt, 1981) and up to 8.7 GPa (Angel et al., 2003) in ethanol-methanol pressure medium, as well as by means of ab initio calculations up to 17 GPa (Gibbs et al., 2000) . These studies concluded that the symmetry of the unit cell appears less hexagonal with increasing pressure, undergoing compression in the *a* direction more than twice as much than in the *c* direction. Also, the most obvious structural change upon compression was found to be the reduction of four out of five different Si-O-Si angles, with smaller angles undergoing more compression than the larger ones. The Si1-O1-Si1 angle is constrained to 180 ° due to symmetry requirements. The O1 atom is placed on an inversion center and as long as the symmetry is maintained, the Si1-O1-Si1 linkage remains linear, giving rise to the high stiffness of the structure. Spectroscopic experimental studies on the high-pressure behaviour of coesite (Hemley, 1987; Williams et al. 1993) observed changes in the spectra of coesite collected at ambient temperature and

at the pressures of 22–25 GPa, and reported that coesite becomes amorphous above 30 GPa. The authors attributed such changes to a high-pressure phase transformation occurring in coesite; however, no further investigation has been reported to better describe such behaviour.

1.4.3 Cristobalite

High-pressure behaviour of α-cristobalite is of interest form the geological standpoint because it was experimentally observed that under elevated pressures and at ambient temperature this polymorph with 4-fold coordinated silicon can transform to seifertite – a lower mantle phase with octahedrally coordinated Si (e.g. Dubrovinskaia et al., 2001; Prokopenko et al., 2001; Yahagi et al., 1994). The transformational sequence is as follows. The tetragonal α-cristobalite transforms to a monoclinic cristobalite-II near ~1.5 GPa upon compression. The structure of this higher-pressure polymorph was recently solved by Dove et al. 2000 using neutron diffraction and by Dera et al. (2011) using *in situ* single crystal x-ray diffraction. Above ~10 GPa cristobalite-II is found to transforms to cristobalite X-I. Apart from the recent assumption of the unit cell parameters (Dera et al. 2011), the structure of the cristobalite X-I still remains unknown. Further compression of cristobalite X-I above pressures exceeding ~35 GPa leads to formation of cristobalite X-II, which is the polymorph reported to have the structure of seifertite. However, there is a large discrepancy among various experimental observations regarding the pressure at which this transition takes place and the structure of the HP polymorphs has not been yet determined.

1.5 Motivation & challenges of this study

Pressure-induced metastable polymorphs can hardly be preserved at ambient conditions and thus are rarely ever observed in natural materials. However, they play an important role in transformation mechanisms between the thermodynamically stable polymorphs. At sufficiently low temperatures in static and shock-wave high pressure studies the transformation from lower-pressure silica phases to the thermodynamically stable high-pressure phases are not direct (Hemley et al., 1994) and strongly depend on the formation of intermediate phases. This is the reason why understanding the structures of metastable polymorphs is of great interest in studying transformation pathways experimentally, as well as in numerical modellings that predict behaviour of silica at extreme conditions (e.g. Donadio et al., 2008; Huang et al., 2006; Martoňák et al., 2007).

Although one of the most studied systems over the past decades, structures of many SiO_2 phases at higher pressures have not yet been depicted. The phase diagram of silica is strongly simplified; it often omits large hysteresis in temperature and pressure. A major complexity in studying the behaviour of silica arises from the fact that the transition mechanisms, the pathways through intermediate crystalline phases and the onset of pressure-induced amorphization strongly depend on the starting polymorph, as well as on the hydrostaticity and stress anisotropy present in the sample during experiments. Differential stress largely influences the sequence of transitions, so it is of outermost importance to study the structures based on single-crystal X-ray analyses.

Presence of numerous metastable polymorphs of silica has been observed so far by spectroscopic or powder diffraction tenchiques (Fig. 1.4) but only few of the structures have been determined, often addressed with great uncertainties. This is considered a great challenge in high-pressure crystallography for the following reasons: 1) very low scattering factor of silicon and oxygen lead to poor quality of data for structural determination; 2) metastable phases show poor crystallinity with enhanced structural disorder and are almost impossible to recover; 3) the limiting sample size (<30 μm) used in studying these materials at elevated pressures, combined with poor crystallographic constraints, restricts the investigation techniques solely to the most intense radiation sources –i.e. synchrotrons.

In this study the aim was to systematically understand the compressional behaviour of the two polymorphs, coesite and cristobalite, regarding the phase transitions that they undergo at higher pressures. These polymorphs represent two extreme structural arrangements of tetrahedral silica forms by means of density and "openness" of the structures, resulting in very different densification mechanisms and response to pressure.

2. METHODS

This chapter gives an outline and a brief background of the experimental and analytical techniques applied in the study. Exact experimental procedure and analytical conditions are given later, in the corresponding manuscripts.

2.1 Synthesis and characterization of the starting material

Starting material used for synthesis of crystalline SiO_2 polymorphs needed for *in situ* high-pressure diamond-anvil cell experiments (HP-DAC) was commercial silica glass (Merck 1.08044.0100). The glass in form of 1-2.5 mm sized irregular granules has very low impurities content, as was determined by LA-ICP-MS (see further). Starting from this glass we synthesized SiO_2 polymorphs using high-pressure and/or high-temperature apparatus available at BGI: coesite was synthesized using piston-cylinder apparatus; α-cristobalite was synthesized using high-temperature furnace. In addition to synthetic α-cristobalite, we also used a natural sample from Ellora Caves in India, provided by Harvard Museum of Natural History.

2.1.1 LA-ICP-MS

Prior synthesizing crystalline silica polymorphs, we analyzed trace element composition of the starting silica glass, and of the natural samples of cristobalite by Laser Ablation (LA) – Inductively Coupled Plasma (ICP) – Mass Spectrometry (MS). Measurements were performed using a 193 nm ArF Excimer laser (Geolas M system; Coherent) connected to a quadrupole mass spectrometer (Elan DRC-e; Perkin Elmer). In this instrument, the sample is stored in an air-tight chamber where the 193 nm wavelength laser beam hits the sample and ablates it to form aerosols. The sample aerosols are carried away to the ICP segment with a gas flow of helium mixed with a small amount of hydrogen. Here argon is electrically heated by an inductive coil to very high temperatures to form plasma by which the sample aerosol is ionized. The ion beam leaves the ICP and, being focused by a set of lenses, it enters the mass spectrometer. In the quadrupole mass spectrometer, which operates in high vacuum, ions are separated according to their mass to charge ratio, allowing quasi-simultaneous measurement of many elements. In order to integrate collected data, we compared our measurements with a NIST 610-glass as external standard. Additionally, we used a quartz crystal of well-determined

composition as an internal standard, as reported in Audétat et al. (2014). The analyzed elements and their concentrations are reported in the corresponding manuscripts.

2.1.2 Coesite and cristobalite synthesis

Coesite crystals of a suitable size and quality for HP-DAC experiments were synthesized in the *Voggenreiter* piston-cylinder (PC) apparatus. Starting silica glass granules were ground under ethanol using agate mill to produce fine-grained powder, which was then loaded with approximately 5 wt % distilled water into 10 mm long, 5 mm outer-diameter and 4.6 mm inner-diameter Pt capsule (Fig 2.1). The water was added to enhance growth of larger crystals. The Pt capsule was welded shut on both sides while being cooled in liquid nitrogen, in order to prevent loss of water due to the heating. The capsule was then placed into a standard ½ inch pyrex-talc PC assembly also shown in Figure 2.1. The assembly consists of several layers: a pyrophyllite sleeve surrounding the capsule that prevents the contact of the metal with the graphite heater and absorbs water in the case of escape from the capsule; ceramics of a common name "crushable" alumina in form of a cone and a disk placed at the bottom and the top of the capsule act as spacers and pressure medium within the heated area; a tapered graphite resistance heater that allows minimal temperature gradient alongside the capsule (Bromiley and Keppler, 2004); a pyrex sleeve that acts as a thermal insulator to shield the outside of the assembly and a talc sleeve that is an outside pressure medium. The upper alumina spacer has a hole in the center to provide space for a thermocouple employed to monitor temperature.

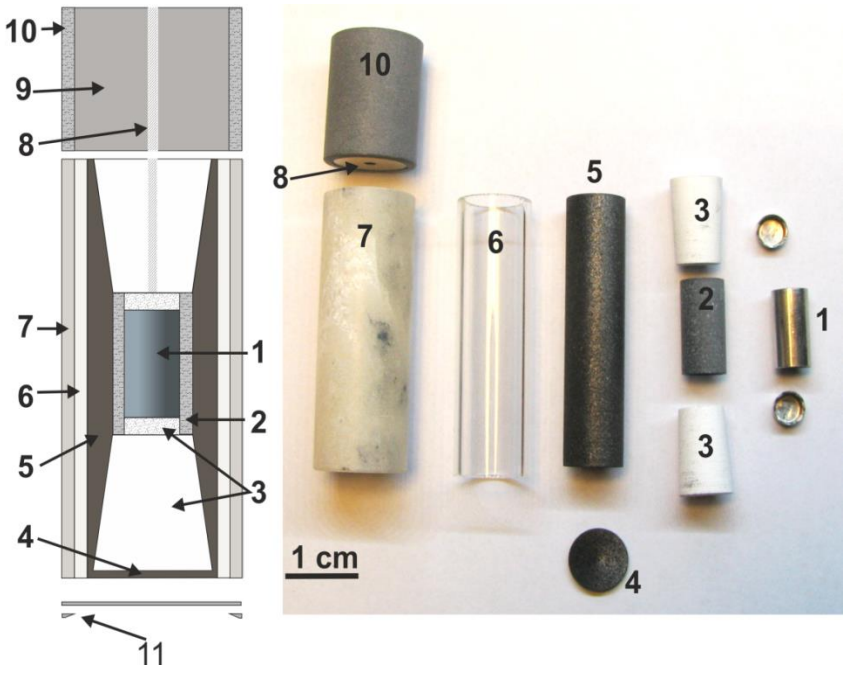

FIGURE 2.1. Piston cylinder ½ inch pyrex-talc assembly. 1) platinum capsule; 2) pyrophyllite sleeve; 3) "crushable" alumina spacers; 4) graphite disc at the bottom of the graphite heater to provide the electrical circuit; 5) tapered graphite heater; 6) pyrex sleeve; 7) a talc sleeve; 8) central hole for the thermocouple passing through the alumina and 9) steel cylinder conducting the electricity to the heater with 10) pyrex sleeve that prevents contact of the steel and the surrounding metal of the press; 11) steel disc and ring that ensure the electrical contact of the graphite and provide the flattened contact of the assembly and the piston. Modified after Bromiley & Keppler 2004.

The piston-cylinder press used in this study consists of two hydraulic rams: the lower, master ram creates pressure directly onto the sample while the top ram provides a confining end load. The master ram creates pressure by pushing a 0.5 inch tungsten carbide piston into a bomb, where the sample is stored within a 0.5"-diameter chamber. The inner part of the bomb consists of tungsten carbide whereas the outside is made of hardened steel. The compression of the bomb against the top ram allows for creating pressures up to 40 kbar. If lower pressures are needed (up to 20 kbar) one can either use a larger piston (¾ inch) in this type of press or a press without end load ram. During the experiment, while the furnace is heated by passing an electrical current through it, the bomb is being cooled by water, so that most of the PC metal remains close to the room temperature. A detailed description of PC apparatus is given, for example, by Johannes (1973) and by Keppler and Frost (2005).

The sample was pressurized up to ~90% of the desired pressure and then heated at 100 °C/min up to 1250 °C. After stabilization of the temperature, the sample was fully compressed to 35 kbar and then held at these conditions for ~15 hours. In the end, the sample was slowly cooled (ramped) down to 1100 °C over 5 hours and finally quenched. The temperature was monitored throughout the experiment using a type S (Pt - $Pt_{10\%}Rh$) thermocouple. In the successful experiment run A14 slow cooling procedure and water-saturated conditions resulted in growth of relatively large (above 100 μm in linear dimensions) crystals, which were then used for the HP experiments.

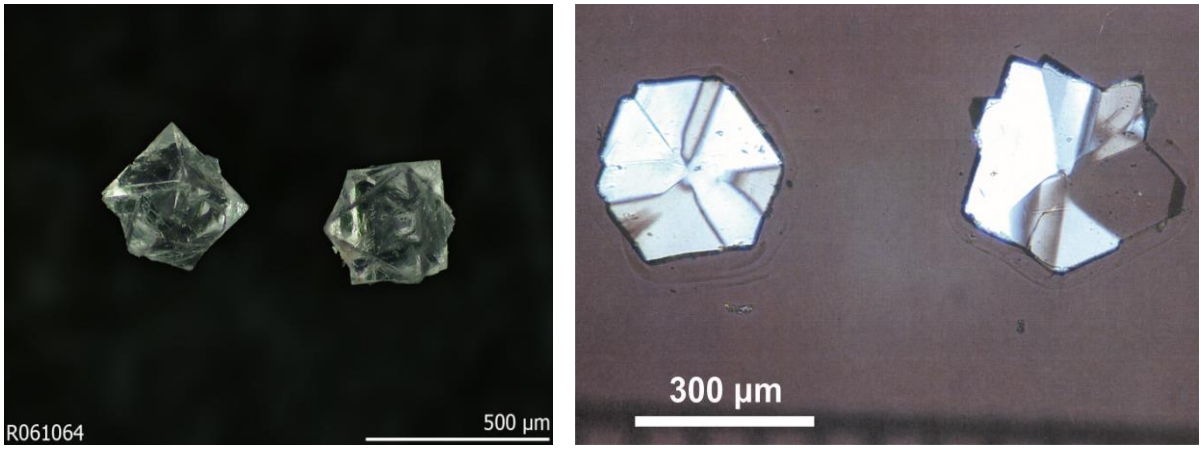

FIGURE 2.2. Natural crystals of cristobalite from Ellora Cave, India. The sample was obtained from Harvard Museum of Natural History. The figure on the left is taken from the database of Raman spectra, X-ray diffraction and chemistry data for minerals (www.rruff.info). On the right, an optical microphotgraph of ~20 μm thinsection of the crystals obtained under cross-polarized light, indicating single-crystal domains up to ~100 μm in linear dimension.

Cristobalite was synthesized by heating the glass granules at temperatures of ~1650 °C for 3 hours and then cooling down slowly over 15 hours to ~1500 °C (a temperature slightly higher than that of

cristobalite-trydimite transition), and then rapidly quenched. This procedure allowed the growth of cristobalite crystals up to ~100 μm in linear dimension; however it was not possible to avoid twinning which occurs on cooling due to the transition from the cubic *β*-cristobalite to the tetragonal *α*-cristobalite. These crystals were of sufficient quality for Raman spectroscopy but not for single crystal X-ray diffraction for which we had to use the natural cristobalite (Figure 2.2).

2.1.3 Powder and single-crystal X-ray diffraction

The in-house X-ray diffraction instruments available at BGI were used to characterize the synthesized materials and to select good quality single crystals for HP-DAC experiments. X-ray diffraction is widely used a non-destructive technique for obtaining structural information of crystalline materials. When X-rays interact with matter, they are elastically scattered by electrons and if the target atoms are arranged in such a way that they show long-range periodicity, diffraction pattern can be created. Diffraction is effective only at certain incidence angles with respect to the reflecting planes, determined by Bragg's law (Bragg and Bragg, 1913):

$$2d\ sin(\theta) = n\lambda \quad (1)$$

where d is the interplanar distance, λ is the X-ray wavelength and θ is the half angle between the incident and diffracted beams (Fig. 2.3). When the diffraction condition is satisfied, the reflection angle equals to the incident angle, and the two angles are bisected with the reciprocal vector, which points to the *hkl* reflection (Fig. 2.3). Intensity of the reflected radiation is not equal to the incident intensity but it is related to the mean electron density within the direct lattice plane.

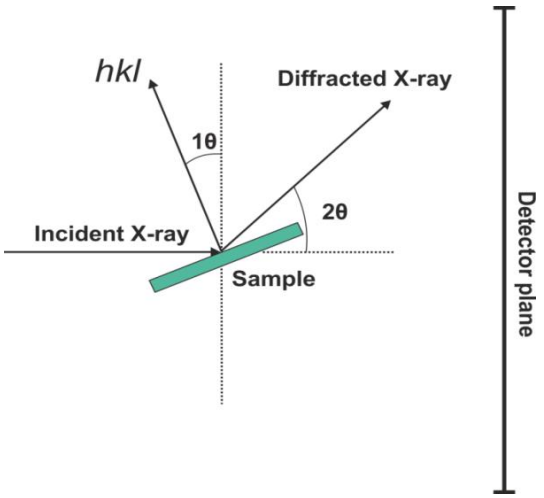

FIGURE 2.3. Basic principles of the Bargg diffraction condition (Modified after Dera, 2010). Incident beam of the wavelength λ is diffracted from a set of *hkl* planes with the interplanar *d*-spacing. Diffracted beam is collected on a detector plane perpendicular to the incident beam.

In the case of monochromatic X-ray source, diffraction pattern creates co-axial cones with apexes located where the incident beam interferers with crystalline planes. In a powder sample, numerous crystallites are randomly oriented and there are always crystalline planes properly orientated to fulfill the Bragg's equation, thereby contributing to a diffraction pattern in a form of (almost) complete cone. Therefore in a powder X-ray experiment (PXRD) we often see (partially) closed circles (Debye-Scherrer rings) collected on a detector plane. However, in the case of single-crystal diffraction (SC-XRD) the crystal has to be rotated in order to bring as many planes as possible into diffraction condition. PXRD experiments are usually carried out to obtain *d*-spacings of lattice planes (*hkl*) in order to calculate unit cell parameters of a known structure. In contrast to PXRD where the information is gathered in a 2-D image, SC-XRD dataset consists of 3-D diffraction intensities from the whole reciprocal space. With the completeness and the redundancy of such datasets it is possible to fully refine atomic coordinates of a known structure or to determine even very complicated new structures.

For the different research projects described in the following chapters, crystals were selected based on their optical quality – size, transparency, crystal shape, surface appearance, etc. Very small crystals (up to ~20 μm in linear dimension) were tested using a rotating anode high-brilliance Rigaku diffractometer equipped with MoKα radiation (λ=0.7080 Å) operated at 60 kV and 50 mA, and with an Osmic focusing X-ray optics and a Bruker Apex CCD detector. Intensity data of crystals larger than 20-30 μm in diameter were collected using a 4-circle κ-geometry Xcalibur diffractometer equipped with MoKα radiation operated at 50 kV and 40 mA, a CCD detector, a graphite monochromator and a 0.5 mm collimator. For unit cell parameter determination and crystal quality test, short pre-experiments were run using omega scans 20-40°, step size 1° and 10 s/frame exposure time. Full data collection procedures were then optimized based on the pre-experiment and the chosen parameters varied depending on the crystal symmetry and collected intensities. Most commonly, omega scans were chosen to collect the full reciprocal sphere up to 2θ max = 70°, with step size 0.5 – 1.0° and exposure time 10-30 s/frame, choosing high redundancy to improve statistics. After the collection, a *jpeg* movie was recorded every 2° during phi-rotation to confirm good centering of the crystal. Data reduction and integration were performed using the CrysAlisPro package (Oxford Diffraction 2006). No absorption corrections were necessary due to the very small absorption of SiO_2 and very small crystals sizes. Structure refinements were performed based on F^2 using the SHELX97 program package (Sheldrick, 2008) in the WingX System (Farrugia, 1999) starting from appropriate atomic coordinates, as described in the following manuscripts.

2.2 High-pressure experiments

2.2.1 Diamond anvil cell

2.2.1.1 The set-up

Diamond anvil cell (DAC) is one of the main devices utilized in static high-pressure studies in geosciences, physics, material sciences and related fields and it has been in use for over 50 years (Bassett, 2009). Two main characteristics of DAC technique are crucial: 1) pressures up to several megabars can be reached and 2) diamonds are essentially transparent to electromagnetic radiation in a wide range of photon energies, including optical, near-infrared region and X-rays, allowing various phenomena – diffraction, scattering, absorption, emission etc. – to be observed *in situ*. The biggest disadvantage of this technique is a very small sample size (tens to hundreds of μm). The only other feasible technique that can generate such high pressures, albeit based on a dynamically driven compression, employs shock-produced pressures generated by explosions, gas-guns or by lasers.

Many different designs and adaptations of DACs are available around the world, but the basic principle and the main components remain similar. A typical DAC consists of two diamonds mounted on two opposite metal holders. The pressure is created by compressing these holders against each other while mechanically tightening the screws. The pressure is defined as a ratio of a force over the area over which it is applied. Therefore with a small diamond anvil surfaces a moderate force can generate very high pressures. In general, diamond anvil cells can be divided into two groups based on the metal holder design: plate-opposing and piston-cylinder DACs. A nice overview of DACs development and designs is given by Mao & Hemley (1998) or in Bassett (2009). Very detailed instructions on DAC preparation and theoretical backgrounds are given in Miletich et al. (2000).

Not only is diamond one of the hardest materials known, with a very high bulk modulus (~440 GPa; Dewaele et al., 2004), but it is also transparent to various kind of radiation and chemically mostly inactive up to moderate temperatures. Therefore it is still the best candidate for the purpose of *in situ* studies at extreme pressures. A new type of high-pressure cells using moissanite (SiC compound) has been developed recently to substitute for diamonds instability above 700 °C (Keppler & Frost, 2005 and references therein). Nonetheless, this new method has shown several disadvantages and it is still not in routine use. Diamonds are used in form of single crystals, usually cut perpendicular to a crystallographic axis. The size of the flat cut (culet) determines the maximum pressure that can be reached in the experiment. Common culet sizes range from 60 μm to 1 mm, attaining pressures of ~300 to ~10 GPa, respectively. The opposite side of the diamond, table, fixed to the holder, is usually

3 to 6 mm wide. With increasing table/culet ratio the maximal achievable pressure increases. The critical point of experimental set-up is to position the culets perfectly parallel to each other and to align them precisely. If the culets are slightly misaligned (precision needed is ca. 1μm), diamonds will crack under pressure. Diamonds in use are mostly natural. Depending on their nitrogen content, they are divided into types I and II. Type I is much more common and therefore cheaper, but due to the higher nitrogen content which contributes to high fluorescence, diamonds of this kind might not be always suitable for spectroscopic studies, whereas for X-ray studies the nitrogen impurity has no major effect. However, the geometry of the diamond is essential for the single crystal X-ray measurements. In order to allow for large coverage of the reciprocal space, a special design of the diamond shape has been developed (Boehler and De Hantsetters, 2004). The conical side of the so-called Böhler-Almax diamonds has the optical aperture of 90°. In Figure 2.4 (insets 5 and 6) difference between the standard and the Böhler-Almax diamonds is demonstrated. The diamond anvils are fixed to a metal "seat", usually made of tungsten carbide. A gasket made of hard metal is placed between the anvils, usually hard steel or rhenium, the latter one allowing pressures exceeding 30 GPa and remaining stable up to ca. 600 °C (my own unpublished experiments). Gasket is pre-indented before use by compression between the anvils which leave a deep imprint in the metal. Such procedure allows to 1) re-check the alignment of the anvils after reaching moderate pressure; 2) to strain-harden the gasket and 3) to create a hump of the metal on the outside which supports the anvils during compression. A sample chamber is then drilled within the indentation. A common way to do this is to use a spark-eroder, but several labs have recently substituted this time-consuming method by faster and more precise laser-drilling. Diameter of the chamber should be 1/3 up to 1/2 of the culet size.

In this study a piston-cylinder DAC type BX90 designed at BGI (Kantor et al., 2012) was used. It basically consists of a top part, the piston, which fits exactly into the bottom part, the cylinder, providing high mechanical stability and a precise alignment of the diamonds. Circular 12-mm side openings in the piston and in the cylinder allow easy access and adjustment of the seats, which is crucial for precise alignment of the diamonds. Wide (90°) symmetrical axial opening of the DAC combined with the Böhler-Almax diamonds allow for successful single crystal X-ray diffraction experiment. In this study type-I diamonds were used. For the spectroscopic experiments, however, we selected only diamonds with very low background. Two sizes of BX90 cells were used– a larger one for the room temperature experiments and the smaller for heating experiments (Fig. 2.4).

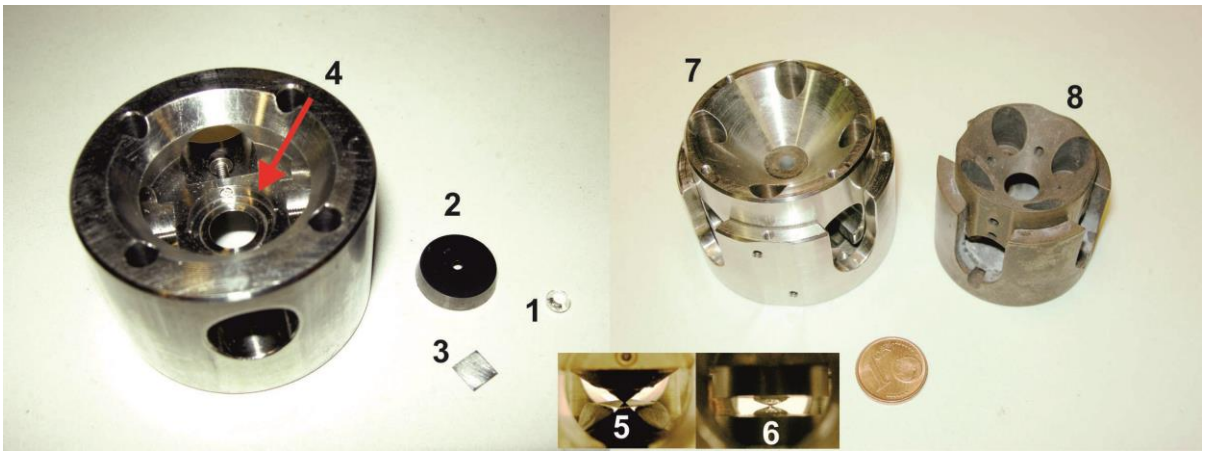

FIGURE 2.4. Components of a diamond-anvil cell (DAC): 1) diamond; 2) tungsten-carbide seat; 3) rhenium gasket; 4) piston (top) part of the DAC, red arrow indicated circular cavity where the seat is fixed; 5) standard diamonds; 6) Böhler-Almax diamond design; 7) closed BX90 DAC; 8) small design of BX90 used for heating experiments; rust on the surface comes from the oxidation during high-temperature treatment.

2.2.1.2 Pressure-transmitting medium

The DAC consists of two opposite anvils, resulting in stress along the loading direction to be greater than the stresses in the gasket plane. In most of the HP experiments it is essential to maintain (quasi)hydrostatic conditions within the sample chamber. In order to do so, pressure-transmitting medium is normally inserted into the pressure chamber. The best pressure-transmitting media are light noble gases, such as He and Ne, due to their chemical inertness and relatively high solidification pressures. Even after solidification, these gases behave quite soft and hydrostatically. Light rare gases have low X-ray absorption and give low background, and are therefore particularly suitable for X-ray diffraction measurements in DACs (Kurnosov et al., 2008).

We used neon as the pressure-transmitting medium because it provides quasi-hydrostatic conditions up to the highest pressures attained in this study. Although helium is shown to provide better hydrostaticity (Klotz et al., 2009), it has a disadvantage of decreasing mechanical stability of diamonds by diffusing into them (Kurnosov et al. 2008 and references therein). Another significant disadvantage of using helium in this study is that it may occupy large voids in the loose structures of the investigated SiO_2 phases, thus contributing to an overall volume increase and influencing the structural behaviour (Sato et al., 2013).

Neon crystallizes at 300 K at 4.8 GPa. As studied by Klotz et al. (2009), who employed several rubies placed around the chamber, the first signs of non-hydrostaticity appear at 15 GPa. Beyond such pressure, however, the values of pressure gradients remain very small: at maximal pressures they

achieved - 50 GPa - the standard deviation of pressure detected by the different ruby spheres is less than 0.5 GPa, i.e. less than 1% and hence very similar to the case of helium. According to the X-ray diffraction analyses by Dewaele et al. (2008), neon provides quasi-hydrostatic conditions at least up to ~100 GPa, based on observation that all the X-ray diffraction peaks, except for the (111) reflection, broadened considerably only above this pressure.

2.2.1.3 Pressure determination

Two general methods are commonly used in order to determine pressure within a DAC. One possibility is to monitor pressure using a pressure marker loaded along with the sample, such as ruby sphere or powder of a metal with well-defined equations of state (e.g. W, Ag, Cu, Pt…). Another possibility is to determine pressure using the surrounding pressure medium. Ruby pressure relies on the fluorescence method and it requires an incident laser source and a spectrometer. In the case of the metal pressure markers or the pressure medium, one needs to know their EOS and to determine unit-cell using X-ray diffraction. In this study pressure was determined using ruby fluorescence method and/or neon EOS.

Ruby is a red gemstone-quality variety of corundum (α-Al_2O_3) in which Cr^{3+} atoms substitute Al^{3+} at the octahedral site. As a transition metal ion, Cr^{3+} is a strong adsorption and fluorescence center. Upon absorption of light, d-electrons of chromium are transferred from the ground $^4A_2$ state to the excited $^4T_1$ state, corresponding to a spin-allowed transition. This excited state then decays into an excited ^2E state, which has a spin multiplicity different from that of the $^4T_1$. This transition does not involve energy emission because the energy is used for the lattice vibration. From the ^2E state the system returns to the ground $^4A_2$ state, involving light emission due to a sharp spin-forbidden transition. The emission spectrum of ruby related to the ^2E -> $^4A_2$ transition is dominated by two sharp bands, R_1 and R_2, located at about 692.8 nm and 694.2 nm at room pressure and temperature, respectively (Nasdala et al. 2004). The difference of ~ 1.4 nm between the two bands is caused by splitting of the ^2E excited state. The red fluorescence bands of ruby show significant pressure dependence and their frequency shift was calibrated to obtain a ruby pressure gauge in several studies (Dewaele et al., 2004; Mao et al., 1986; Xu et al., 1986; Zha et al., 2000). The most commonly used gauge is the one reported by Mao et al. (1986), calibrated up to ~80 GPa in argon pressure medium. The wavelength shift of the R_2 fluorescence line was in that study calibrated against the pressure derived from simultaneous X-ray diffraction measurements of the unit cell volume of copper, by referencing it to the Hugoniot equation of state obtained in an earlier shock wave experimental study (Mao et al. 1979). The pressure relation for the ruby line is given as:

$$P = {}^{A}/_{B}\{[1 + ({}^{\Delta\lambda}/_{\lambda_0})^{B}] - 1\} \quad (2)$$

Where P is the pressure in Mbar, λ_0 is the wavelength of the ruby line in nm at ambient conditions and whose position is dependent on the initial Cr content, $\Delta\lambda$ is the difference between λ at a measured pressure and the λ_0, and A and B are refined parameters of the function. In quasi-hydrostatic conditions A = 19.04 Mbar and B = 7.665, but in non-hydrostatic environment B = 5. The difference between the two scales is demonstrated in Figure 2.5.

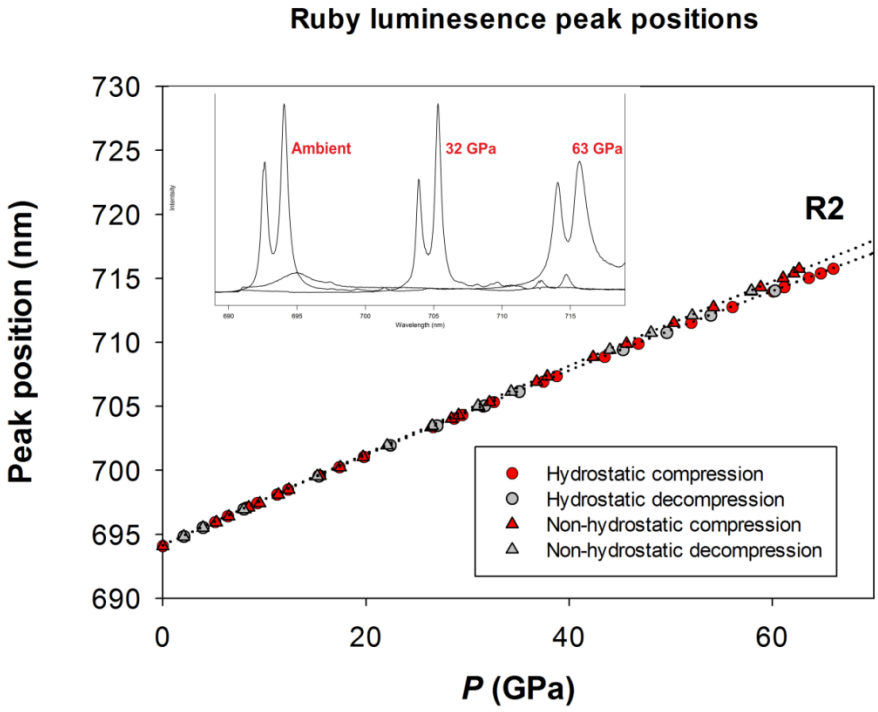

FIGURE 2.5. Ruby spectra recorded at different pressures and at room temperature during compression and decompression of cristobalite X-I (experiment Exp4, Chapter 6). Dotted lines are given equations (2) for the ruby line pressure dependence in hydrostatic (circles) and non-hydrostatic (triangles) environment. The differences between the two estimates are significant above 40 GPa. Inset of the ruby spectra shape demonstrates slightly asymmetric appearance at the highest pressure.

A more recent study by Zha et al. (2000) recalibrated the ruby pressure scale against a primary pressure scale of MgO, which is based on integrated pressure-density data obtained by Brillouin and X-ray diffraction measurements up to 55 GPa in helium pressure-transmitting medium. The accuracy of the ruby scale was reestablished within ±1 %, suggesting B = 7.715. At higher pressures, however, the upcoming studies provided increasing evidences that the Mao ruby scale underestimates pressures, particularly above 40 GPa (e.g. Chijioke et al., 2005; Dewaele et al., 2004; Fei et al., 2007). A quasi-hydrostatic compression in helium up to 120 GPa suggests significantly higher B values of

10.32(7), as established by studying MgO (Jacobsen et al., 2008). The effect of hydrostaticity was seen even earlier (Hemley, 1989), where ruby was calibrated against tungsten in neon pressure medium up to megabar pressures. Their data collected in neon suggest slightly higher *B* values than in Mao's scale (argon) for the pressures exceeding 80 GPa, but not as high as suggested for data collected more recently in helium (Zha et al. 2000; Jacobsen et al. 2008). It should be noted that argon pressure medium provides hydrostatic conditions only up to low pressures - first signs of non-hydrostaticity are seen ~2 GPa (Angel et al., 2007; Klotz et al., 2009). A recent overview on methodology of pressure determination using ruby luminescence is given by Syassen (2008).

The ruby spheres obtained commercially for the purposes of this study are 5-10μm in diameter and contain 3600 ppm Cr^{3+}. A description on synthesis is given by Chervin, Canny & Mancinelli (2001).

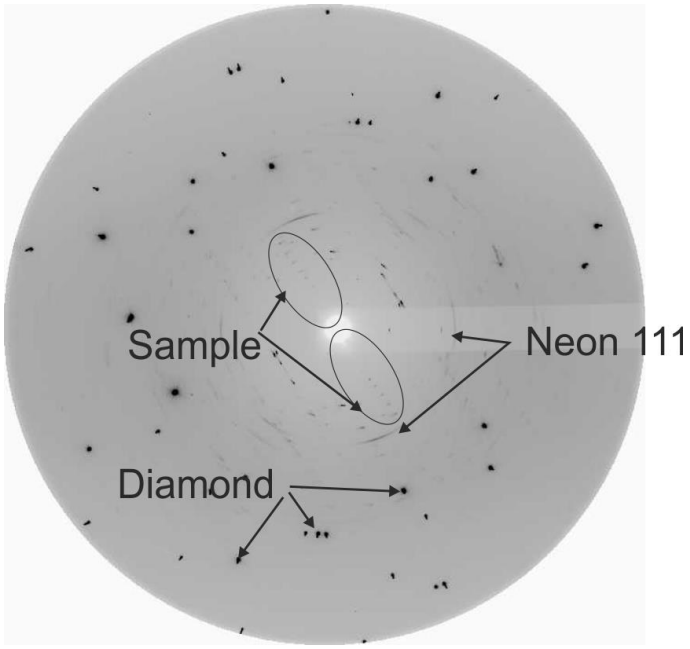

FIGURE 2.6. Full-rotation or a wide-scan image collected in DAC with coesite-II at 27.5 GPa. Strong diamond reflections, weak sample reflections and rings from the solidified neon are indicated. Pressure is determined based on *d*-spacings of neon (111) reflections (e.g. Fei et al. 2007). Further details of in situ X-ray diffraction are given in the section 2.2.3.

Neon. At pressures exceeding 50 GPa the ruby fluorescence signal becomes broad (inset in Fig. 2.5) and consequently the pressure determination becomes difficult. An alternative way to determine pressure is from the neon EOS. Based on X-ray diffraction analyses by Dewaele et al. (2008) up to 208 GPa, the crystal structure of neon remains face-centered cubic over the entire pressure domain, which covers the compression range up to $V/V_0 = 0.24$. Mie–Grüneisen–Debye formalism reproduces very well the present *P-V-T* data for neon as well as low pressure–low temperature data available in the literature. This makes neon a well calibrated X-ray pressure gauge, suitable for high-pressure, high-temperature studies. Compressional behaviour of neon is best described by least-squares fit of

the Vinet equation of state (K_0 = 1.16 (±0.14) GPa and K_0'=8.23 (±0.31), with an initial volume V_0 = 88.967 Å^3 (Dewaele et al., 2008; Fei et al., 2007). The pressure is determined based on the *d*-spacings of the (111) reflections (Fig. 2.6).

2.2.1.4 External electrical heating

Using external electrical heaters associated with diamond anvil cell (DAC) one can cover wide range of temperatures – from 300 to over 1000 K, holding to constant temperatures for many hours or even days at rather high pressures. Two kinds of external electrical heaters were applied separately and simultaneously for the purposes of heating– resistive Pt-wire heater placed in the cavity around diamond anvils and a whole-cell heater (Fig. 2.7a and b). The smaller heater placed around the anvils is made of Pt wire (Ø300 or 500 μm) folded around a 3 mm thick ring made of zirconia-based ceramics. The whole-cell heater has external diameter of 50 mm, it is made of fired pyrophyllite and contains Pt wire 500 μm in diameter folded over the inner surface. Temperature is measured with an external S type thermocouple, placed very close to the contact of the anvils and the Re gasket (Fig. 2.7a). As previously reported by Dubrovinskaia and Dubrovinsky (2003), on heating to 1000 °C the temperature gradient in the center of the high-pressure assemblage is practically absent. In the area of about 5 mm diameter around the diamonds, the temperature varies not more than 2–3 °C. A thermal insulator made of a square-shaped double-layered stainless steel box (Fig. 2.7b and c) was used in heating experiments. Stainless steel of type 1.4571 is temperature-resistant and shows no oxidation effect to at least 600 °C. The purpose of employing such an insulator is to protect the stage and objectives of a Raman-spectrometer used during the heating experiment, to provide homogenous temperature distribution around the DAC placed inside the box, and to maintain temperatures at a constant value for a longer period of time. Each layer of the steel is 1 mm thick and are spaced by 5-10 mm thick fiber-based insulation material used in high-temperature furnace. A 3 mm wide slit on the side allows thermocouple and heaters contacts to be outside of the box, and openings on the bottom and the top provide optical access to the cell. Opening on the top is 35 mm in diameter and it provides easy access to all four screws of the cell aiming at easy pressure adjustment during the heating experiment. The DAC and the whole-cell heater are fixed on a stainless steel holder (Fig. 2.7b). The outer heater was controlled by Laboratory Power Supply EA-PS 9065-20 and the inner by EA-PS 9028-100 (Fig. 2.7d). Maximal output power in the case where only outer heater was used to 600 °C was 270 W (output current 9 A). In the case where the heaters were used simultaneously, we heated with the inner heater to 300 °C (80 W, 10 A) and then joined the outer heater. At 600 °C maximal output power for the inner heater was 144 W (12 A) and for the outer 84 W (6 A). Our first

experiments showed that using an insulation box minimizes the power required to heat the cell and successfully protects stage of the Raman microscope from the heat.

The piston-cylinder type DACs used in heating experiments were developed at BGI and made of high-temperature resistant alloy. Loading screws as well as the contact surface between the two parts of the cell were covered by Molykote 1000 lubricant to avoid welding or locking of different parts. Diamonds and Re gasket were glued with high-temperature resistant graphite bond AREMCO Products Inc.

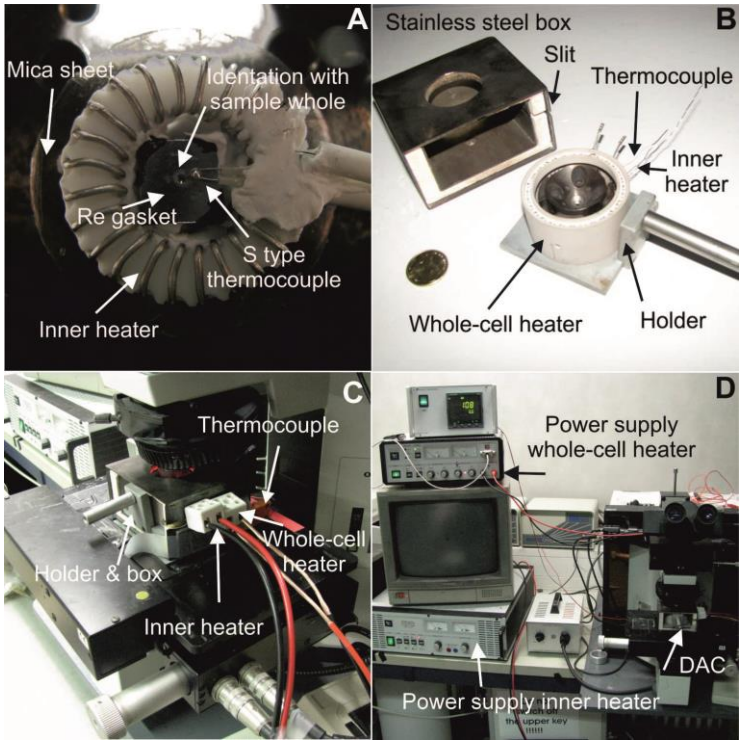

FIGURE 2.7. A) Bottom part of diamond anvil cell with indented Re gasket, a sample hole, S type thermocouple and surrounding inner heater. For scale, Pt wire is 0.5 mm thick, each gasket side is 5 mm, outer diameter of the heater is 15 mm. **B)**. DAC with an inner heater and whole cell heater placed on a holder and double-layered insulation box of stainless steel. **C).** Closed insulation box under the Raman microscope. **D).** Power suppliers for a DAC with two heaters.

2.2.2 *In situ* Raman spectroscopy

Spectroscopic techniques are independent on a long-range periodicity or crystallinity of material as they are probing local structure – e.g. site symmetry, coordination number, local crystallographic environment etc. As such, spectroscopic methods provide complementary information to that of a long-range, average picture obtained by the X-ray diffraction studies. Spectroscopy is also used in case of amorphous materials. Structural respond in minerals is related to changes in atomic bonds and is therefore best observed in the energy range of molecular vibrations, i.e. in infra-red range. One common way of studying the molecular vibrations is to induce the transition of the vibrational states by utilizing incident radiation of similar energies (i.e. in IR range), resulting in either absorption or

emission of radiation that directly corresponds to such transition. A different, complementary approach is to study scattering of the incident radiation – Raman scattering – caused by inelastic interaction with the vibrating molecule. Raman scattering is a weak effect (λ^{-4} dependency) that can be studied using intense monochromatic source, usually a laser in visible range. The photon energy of such radiation is much higher than the energy differences between vibrational states in molecules and crystals, hence no real absorption will occur. However, the incident light will excite the system, enabling existence of virtual, short lived, high-energy states, upon which termination most of the incident light will be elastically scattered without any change in initial energy – Rayleigh scattering. One of the low probable phenomena is that the ground state system gains energy while excited, by reducing the energy of the scattered photon $E=h(v_0-v_1)$. This type of scattering which experiences the red shift due to its partial energy loss is named Stokes Raman scattering. At temperatures higher than absolute zero, the system will contain a very small portion of already excited vibrational states, which may lose their energy due to the interaction with light by transferring it to the scattered photon. This so-called anti-Stoke Raman light is blue-shifted due to the gained energy $E=h(v_0+v_1)$. Figure 2.8 illustrates differences between IR and various Raman phenomena. The intensity ratio of Stoke and anti-Stoke light depends on the distribution of the ground versus excited states (Boltzmann distribution), hence it strongly depends on the temperature. Stoke and anti-Stoke bands appear at opposite sides of the zero-positioned Rayleigh line, nevertheless they are equal in energy. Unless it is of particular interest, anti-Stoke bands are not recorded because it is easier to collect and analyze the more intense Stoke scattering.

A typical Raman spectrum is a plot of light intensity (counts or arbitrary units) versus the shift Δw from the absolute wavenumber of the incident light ($w_0=1/\lambda_0$):

$$\Delta w[cm^{-1}] = \left({}^{1}/_{\lambda_0(nm)} - {}^{1}/_{\lambda(nm)}\right) * ({}^{10^7 nm}/_{cm}) \qquad (3)$$

Where λ_0 is the wavelength of the incident light, and λ is the Raman spectrum wavelength, expressed in nm. In Raman scattering the shift from the incident light is of analytical interest and in this way it can be compared with other Raman spectra, independently of the source wavelengths i.e. absolute wavenumbers used in spectrometer.

Raman spectroscopy is a non-destructive technique widely used for identification and structural characterization of materials. Coupled with diamond-anvil cell it enables in situ experimental investigation of minerals under extreme pressure and/or temperature conditions. An introduction to Raman spectroscopy with a focus on mineral sciences is given in Nasdala et al (2004). Details on technical set-up are given by Gillet (1996) and Goncharov (2012).

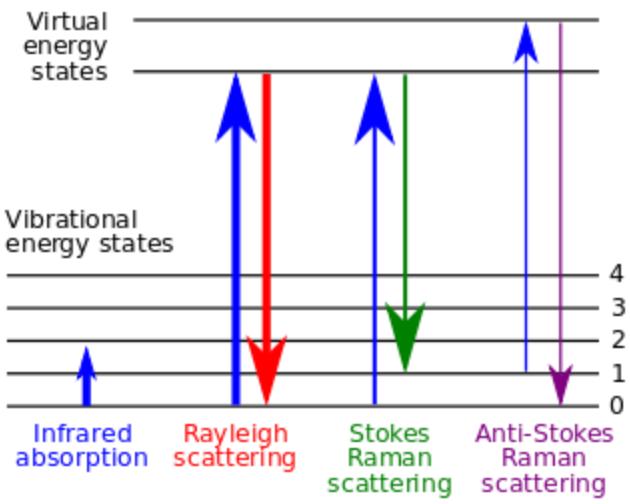

FIGURE 2.8. Vibrational states in a system excited by Infra-red or visible radiation.

In this study we used two different Raman spectrometers: a LabRam system (Horiba Scientific Inc.) with a He–Ne-laser (excitation wavelength 632.8 nm) as well as Dilor XY Raman spectrometer with Ar^+ ion laser (514.5 nm, Coherent Innova 300). The LabRam system is equipped with a notch filter placed at 150 cm^{-1} to cut off the Rayleigh signal. Confocal optics is used to focus the laser beam of 0.15 W on the surface of the sample, enabling the spatial resolution of ~2 μm. A 1200 g/mm grating and an air cooled CCD detector provide the spectral resolution better than 2 cm^{-1} in the investigated spectral range. The Dilor XY is also equipped with confocal optics, but it has a longer optical way, also allowing investigating the range as close to the laser beam as ~75 cm^{-1}. It contains a CCD detector cooled by liquid nitrogen, a double-stage spectrometer with a 1800 g/mm grating, resulting in spectral resolution of 1 cm^{-1}. The output power was varied according to the sample signal between 0.3 and 1.0 W. Data were collected using the Labspec software associated with both Raman spectrometers and fitted using Igor Pro.

2.2.3 *In situ* Synchrotron SC-XRD

Pressures exceeding 50 GPa are attainable in DACs with culet size of 250 μm or less, which means that the initial sample chamber size should be 100-125 μm before loading of the pressure-transmitting medium. After gas loading and upon compression, the chamber size will rapidly shrink until it stabilizes at the point where the pressure medium solidifies, which is at ~5 GPa in the case of neon. At this pressure the size of the sample chamber is around half of the initial size. Above this pressure, the chamber will not shrink drastically, instead of that, however, the gasket will become much thinner during compression. The ~50 μm in diameter chamber is limiting the linear size of the sample to a

maximum of ~30 μm (Fig. 2.9), in order to prevent the risk of touching the edge of the gasket, which could further cause damage or stress on the crystal. In order to rich high pressures (above approximately 30 GPa), the initial thickness of the gasket indentation should not exceed 30 μm, which limits the thickness of the sample to <15 μm. The size of the X-ray beam of a conventional in-house diffractometer is ~500 μm FWHM, therefore also the gasket is irradiated by the beam. A metal gasket is diffracting much more strongly than the sample. Although many experiments can be carried out in-house, the effect of the diffraction from the gasket is a particularly big drawback in case of the experiments with very weakly scattering materials, such as SiO_2. Even testing of coesite and cristobalite crystals of the required size in air prior putting them into a DAC was shown to be problematic in terms of very low diffracting intensities. Once put in the DAC, absorption of MoKα radiation by the DAC significantly reduces the beam intensity, resulting in low intensities from the sample, combined with strong diamond's and gasket's signals. Therefore the HP-DAC experiments could only be carried out at synchrotron radiation facilities.

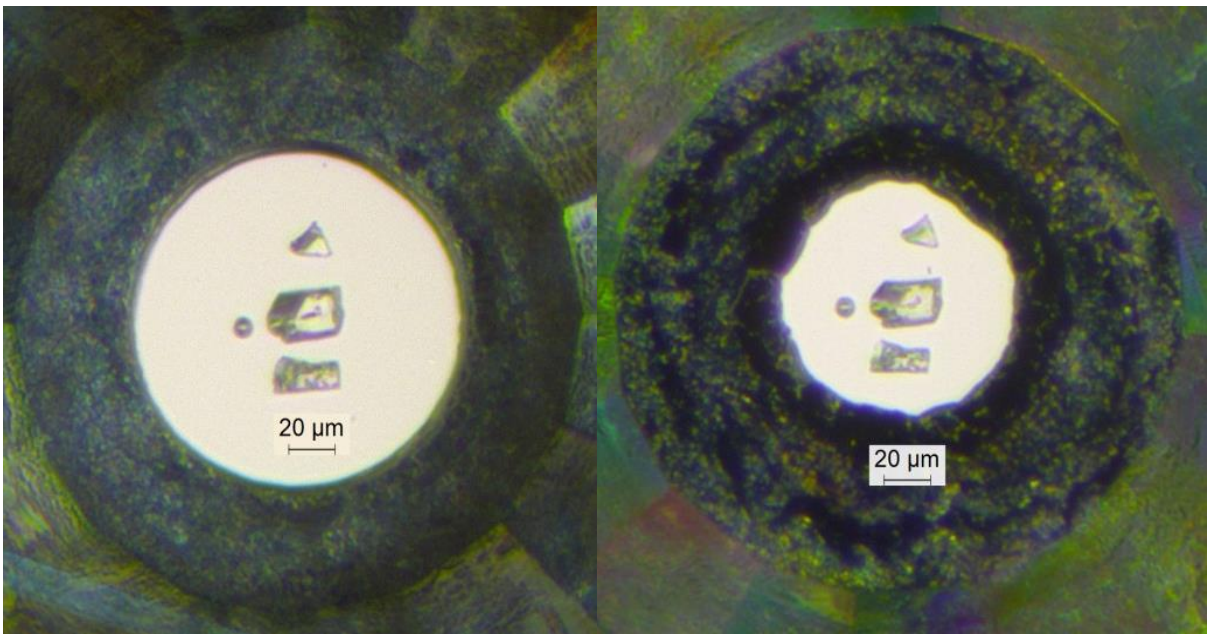

FIGURE 2.9. View on a sample chamber in a diamond-anvil cell loaded with three different cristobalite crystals at room pressure before (left) and after neon gas-loading at 9 GPa (right).

Diamonds are almost transparent to X-rays with energies above ~20 keV, even more so in the case of a short-wavelength synchrotron source (λ~0.3Å) so there is no need for absorption corrections when using the beam which is perfectly centered on the sample. However, the typical beam size of about 5-8 μm (FWHM) limits the single crystals size to be either significantly larger or smaller than the beam

itself. Another problem of *in situ* data collection is intense diamond diffraction which contributes to the very intense diffraction spots which need to be eliminated in order to find the sample (Fig. 2.10).

The major problem encountered for the in situ SC-XRD using diamond-anvil cells is the limited access to the reciprocal space. To assure the sufficient 2θ coverage and therefore the proper coverage of the reciprocal space one needs to choose the diamonds, the support seats and the DAC with high opening angles. The success of an experiment depends strongly on the choice of the DAC and diamond geometry, but also on the crystal quality. The total number of reflections collected in a DAC is far smaller than collected for the same crystal in the air due to the restricted coverage of the reciprocal space. This leads to greater uncertainties in the structural parameters (positional or displacement parameters, reliability values, etc…). Under compression, the unit cell volume will decrease in real space, causing the expansion of the reciprocal lattice and therefore the decrease in the total number of accessible reflections. All these hindrances are particularly limiting in the case of low-symmetry structures, such as monoclinic coesite, due to the requirement of accessing many more reflections of the reciprocal space in order to gain accurate structural information. Notably, pressure-induced phase transitions are often driven by symmetry-lowering mechanisms, so the increase in pressure commonly leads to a decrease in data quality.

Pressure regions of interest (e.g. where a structural change occurs) were first determined by much faster *in situ* Raman spectroscopy and then investigated by collecting SC-XRD data sets. The parameters for the XRD data collection were first determined based on a wide scan image taken of the crystal while the DAC is rotating at a constant speed from the zero position up to the angle of its maximal opening in both directions around the ω-axis of the goniometer. This image contains enough reflections of various intensities to allow a proper estimate of exposure time and step size for the full data collection performed as step scans of in 0.5° or 1.0° in ω for a determined amount of time until the entire accessible opening angle of ±40° is covered.

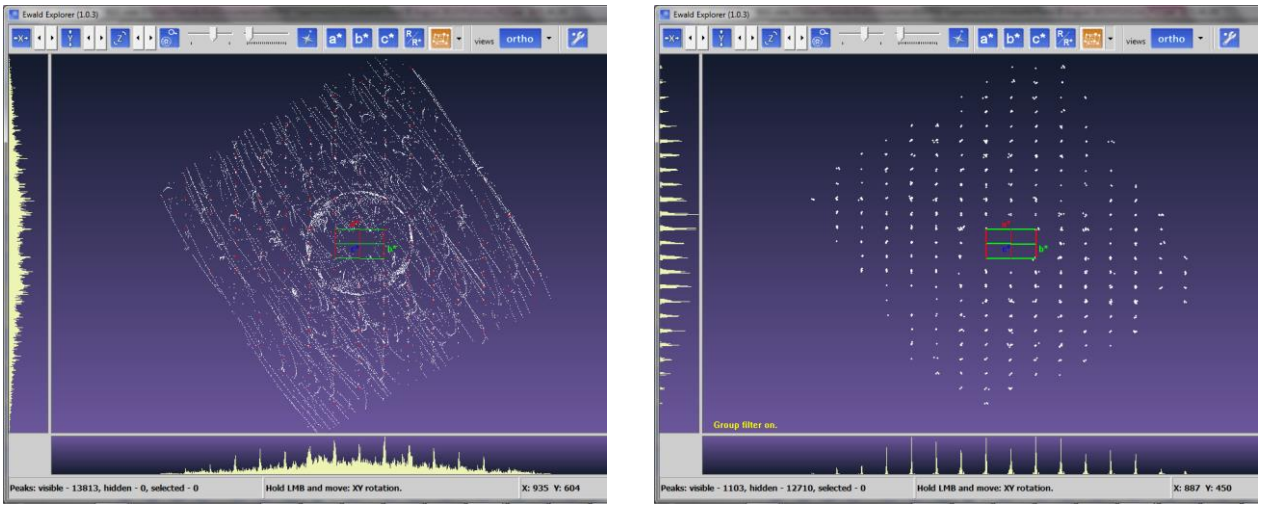

FIGURE 2.10. Representative step-scan data set of cristobalite X-I (Chapter 6) collected at high pressure (20 GPa) presented in the Ewald Explorer window of the *CrysAlis* software. On the left, all collected reflections contain low intensity sample reflections along with strong reflections of diamond, neon and rhenium. On the right, reciprocal lattice of the sample is extracted from the entire data set and the *hkl* reflections are indexed based on a unit cell choice. Intensities of the reflections can be readily reduced and integrated.

2.3 Characterization after high-pressure treatment

2.3.1 Scanning Electron microscopy and Focused Ion Beam Applications

Some of the samples recovered after the high-pressure experiments were characterized by Scanning Electron Microscopy (SEM) and prepared for TEM analyses by Focused Ion Beam (FIB) technique. The quenched crystals were fixed with superglue to a glass (Fig. 2.11a), so that only a very thin layer of the superglue was covering the surface (< 3 μm), and coated by a ~15 nm thin carbon layer. Two dual-beam instruments were used; one FEI QuantaTM 3D FEG located at the Faculty of Geosciences, Geography and Astronomy at the University of Vienna and one newly installed FEI Scios dual-beam instrument located at BGI, Bayreuth. Equipped with an electron column and an ion column, these instruments provide both high-resolution imaging and precise site-specific micromachining of the sample. Field Emission Gun Scanning Electron Microscope (FEG SEM) column in these instruments provides a much higher spatial resolution than a conventional SEM with a tungsten-wire thermal emitter. In the FEG gun instrument, electrons are emitted from a single crystal tungsten tip in an electromagnetic field applying an extractor voltage of 4 kV. Beam electrons are then accelerated by an electric field of 15 keV. The high-energy beam is demagnified by electrostatic and electromagnetic lenses and several apertures. Finally, the beam is focused to a specific focal length of the objective lens and deflected in the scan generator unit to scan over the defined sample surface area. The beam

electrons interact with the target atoms and different kinds of radiation are emitted. In order to make use of variable radiation, an SEM instrument is equipped with different detectors. The low-energy electrons ejected from the near surface of the sample are collected by an SE (Secondary Electron) detector, delivering morphological information. At the deeper levels and larger volumes of beam-sample interaction the so-called back-scattered electrons (BSE) are generated by interaction of beam electrons with the atomic cores of the sample atoms. A solid-state semi-conductor detector is used for BSE signal collection. BSEs have higher energies than the secondary electrons and the intensity of BSE signal is proportional to the atomic number (Z) of the target atoms, therefore allowing for Z-contrast imaging. The lighter elements create a lower intensity signal, appearing darker in a BSE image than the heavier ones. The instruments are also equipped with Energy Dispersive X-ray Detector (EDX) for a rapid, semi-quantitative site-specific micro-chemical analysis. This detector collects characteristic X-ray radiation emitted when outer shell electrons of target atoms fall back into inner electron shell positions after inner shell electrons had been knocked out by incident beam electrons.

In the FIB column of the microscope a beam of Ga^+ ions is produced (Volkert and Minor, 2007). In a field emission ion gun liquid Gallium is ionized by a strong electric field at an extractor voltage of 9 kV. Ga^+ ions are accelerated by applying an accelerating voltage of 30 kV. Beam formation and focusing is established by electrostatic lenses, and the ion beam current is controlled by apertures. Collision of the high-energy ions with the sample atoms at the sample surface causes sputtering of target atoms, accompanied by emission of low-energy (10 eV) secondary electrons (ISE) from the top few atomic layers. The ISE signal is used for SE imaging, but the spatial resolution is slightly lower than that of electron beam images. Sputtering of the surface atoms by Ga-ion penetration is used for controlled removal and machining of the sample at nanometer scale. We used FIB to prepare ~100 nm thin, electron-transparent foils of the quenched material for investigation with Transmission Electron Microscope (TEM). The FIB preparation procedure followed several steps.

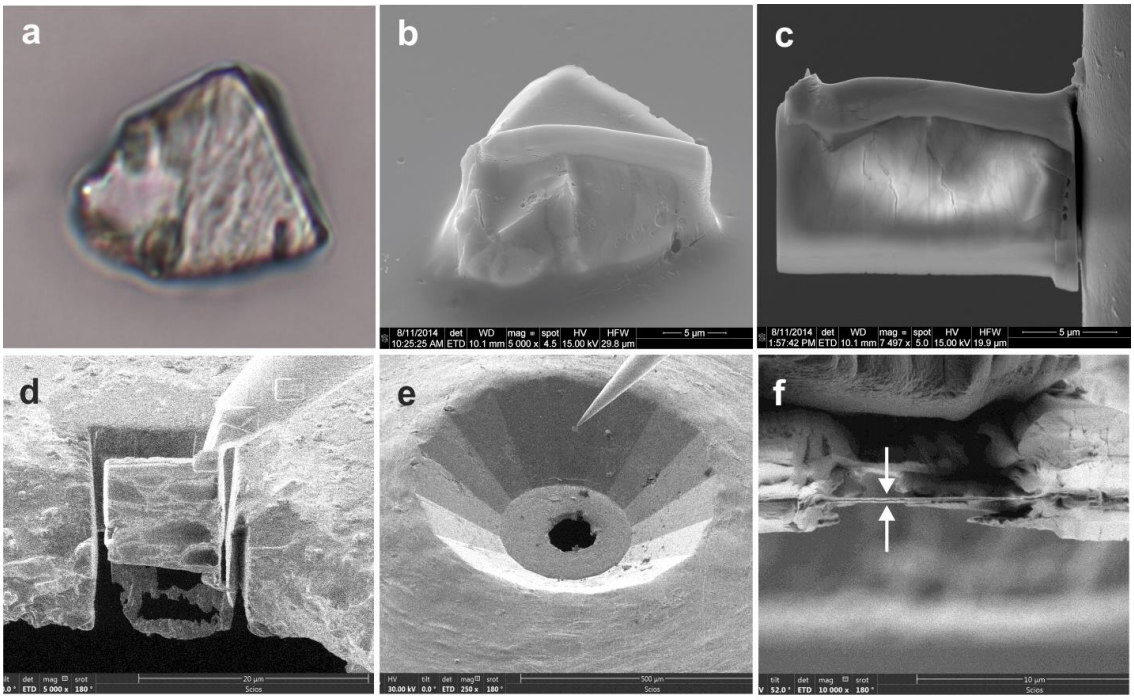

Figure 2.11. Stepwise procedure of the FIB sectioning. **A)** Quenched crystal of cristobalite (Chapter 6 EXP1) seen under optical microscope; **B)** The same crystal seen in FEG-SEM at a tilting angle of 52°; **C)** Thinned foil fixed to the Cu-grid, covered by Pt layer; **D)** Powder sample EXP6 (Chapter 6) extracted from the Re gasket; **E)** Lift-out of this sample using tungsten needle; **F)** Thinned to ~100 nm foil ready for TEM, fixed to the Cu-grid on both sides.

During foil extraction by FIB the sample surface is oriented perpendicular to the incident ion beam, established by sample tilt to 52° (Fig. 2.11b). The of the TEM foil is covered by a ca 2 μm wide and 2 μm thick platinum layer (Fig. 2.11b and c). The Pt layer is deposited using gaseous MeCpPtMe3 (methylcyclopentadienyl-trimethyl-platinum) streamed onto the surface by gas-injection system (GIS) while scanning with the ion beam, resulting in the volatilization of the organics and deposition of Pt. The section beneath the Pt stripe was exposed to the surface by drilling trenches on both sides of the Pt stripe. The first sputtering step was performed using an ion beam of 30 kV and 30 nA to produce a so called "regular cross section". During a second step the exposed foil surface was polished at both sides using beam settings of 30 kV and 15 nA, applying the so called "cleaning cross section" at 4° over- or under tilting of the sample. At a foil thickness of about 1 μm the foil was cut free on three sides ("U-cut") using a 1nA IB current. Subsequently an Omniprobe 100.3 (Vienna) or Easylift system (BGI) micromanipulators were used for in-situ lift-out of the pre-thinned foil and transfer of the foil to a Cu-grid. Then a tungsten needle was inserted into the chamber and fixed to the foil by Pt deposition, after which the foil was cut free from the sample (Fig. 2.11e). The foil was fixed to a Cu grid by Pt deposition (Fig. 2.11c and f), and the Pt contact between the tungsten needle and the

sample was removed by IB sputtering to release the foil from the micromanipulator needle using an ion beam of 0.5 nA. The foil was finally thinned at both sides using progressively lower ion beam currents from 1.0 nA to 30 pA in order to produce an electron transparent sample foil (Fig. 2.11f). The finally thinned TEM lamellae were about 10x15x0.1 μm in size.

2.3.2 Transmission electron microscopy

The transmission electron microscope (TEM) uses a beam of electrons to resolve structures and chemical composition at the micro- to nano-scale (e.g. Williams and Carter, 1996). Electrons are produced by heating a tungsten filament at voltages ranging from 80 to 300 kV, under which they have a wavelength of ~0.04 Å. The highly energetic electrons are fired towards the sample down a column held under vacuum where different electromagnetic –condenser – lenses are used to focus the beam and to transmit it through a very thin specimen (< 150 nm). The electron beam that passes through the sample is then collected and focused by a set of objective and projector lenses. By controlling the strength of these lenses and placing the appropriate aperture, either the diffraction pattern or the image can be modulated and projected on an imaging device, a fluorescent screen. Diffracted beam is used to generate the selected-area electron diffraction (SAED) patterns. Obtained on a very thin specimen, with the electron beam focused in a sub-ängstrom scale, this pattern represents an almost undisturbed 2-D slice of the reciprocal space. Apart for diffraction pattern, the passing electron beam is used to create diffraction contrast imaging. By choosing an aperture that allows only the direct beam to pass, bright field (BF) images are obtained. Also a selected diffracted beam can be used to create the image, in which case corresponding dark field (DF) image is obtained. These techniques are used to visualize microstructural nm-sized features.

In this study the samples were directly removed from the gasket and further prepared either by FIB-technique or by crushing the recovered grains between two glass slides. The obtained powder was dissolved with a drop of ethanol. A drop of ethanol dispersion was then placed on a lacey carbon film on Cu-grid (300 mesh). The chemistry of the grains was also cross-checked using an energy-dispersive X-ray (EDX) analyzer, operated at 200 kV.

3. SYNOPSIS

This cumulative thesis consists of Introduction (Chapter 1), Methods (Chapter 2), two published manuscripts (Chapter 4 and 5) and one ready for submission manuscript (Chapter 6). All manuscripts have been written by me as the first author. The main focus of this work is to understand compressional mechanisms of crystalline SiO_2, by studying two important minerals with very distinct structures, coesite and cristobalite. The most common silica mineral – quartz – has been more extensively studied over the past decades, and its pathways of compression are well constrained. On the other hand, high-pressure experiments on coesite and cristobalite lead to many contradictory results, so that no conclusive model on their compressional behaviour has been reached. This work significantly expands the understanding of how differently structured silica minerals react to hydrostatic and non-hydrostatic (uniaxial) compression, thereby explaining some of the long-standing questions. Chapters 3 and 4 represent an extensive study on high-pressure behaviour of coesite, the densest silica polymorph with four-fold coordinated silicon. The final manuscript included as chapter 5 deals with the compressional behaviour of cristobalite, which has a very loose structure. Here I summarize the most important results from each of the chapters and give a concluding remark.

3.1 Detailed summary of the manuscripts

Pressure-induced phase transitions in coesite (Chapter 4)

(Published in *American Mineralogist*)

This work is focused on understanding the pathways of phase transitions in coesite under high pressures by mainly using *in situ* Raman spectroscopy complemented by *ab initio* calculations of the Raman active phonons and supported by X-ray diffraction. The starting material in form of single crystals of coesite was compressed up to pressures of ~51 GPa using diamond-anvil cells with neon as the pressure transmitting medium. Mineral coesite is widely accepted as a high-pressure indicator found in rocks related to meteorite impact sites, in ultra-high pressure metamorphic rocks or in kimberlites (mantle derived rocks). Crystalline or amorphous metastable phases derived from coesite under high-pressure conditions can be of interest in geological application as potential tracers of peak transient pressure conditions reached in processes such as impacts or faulting.

This study reveals two high-pressure polymorphs of coesite, coesite-II and coesite-III (Fig. 3.1), that remain crystalline (Fig. 3.2) far above the previously reported amorphization pressure (30 GPa). This significant discrepancy between previous and our current results implies that the metastable phase diagram of silica phases requires a substantial revision, as none of the metastable high-pressure phases of coesite has been previously studied.

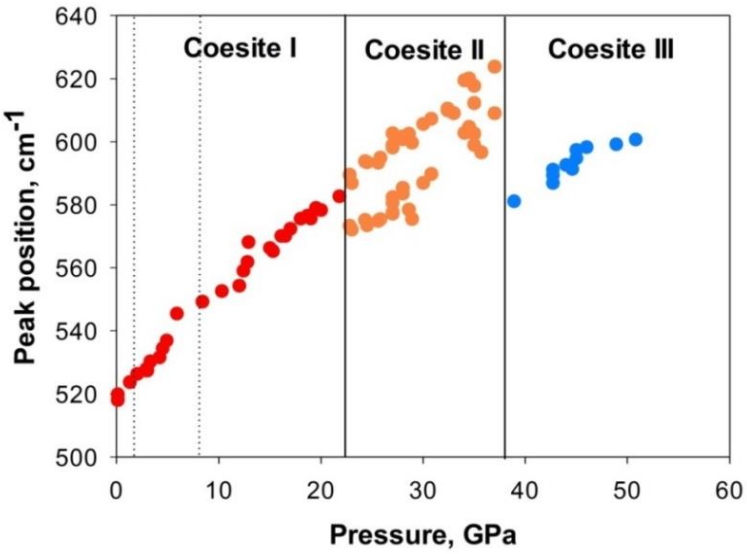

FIGURE 3.1. Pressure dependence of the main Raman active mode obtained from several different experiments at ambient temperature. Phase transitions at ~23 and ~35 GPa are indicated by solid lines, and the thermodynamic stability field of coesite is indicated by dotted lines.

The transition from coesite-I to coesite-II is marked by appearance of a doublet in the main Raman peak (Fig. 3.1). It is probably a displacive, second order in character phase transition arising from the shearing of the four-membered rings of SiO_4 tetrahedra upon compression, as revealed by the phonon softening, continuous behaviour of the main peak, as well as by the absence of hysteresis. Decrease in intensity and softening of the main peak doublet during heating up to ~400 ºC, support the observation that coesite-II is a metastable phase, which exists only at room temperatures far outside the pressure stability field of coesite-I. The heating which is insufficient to transform coesite to the thermodynamically stable phase – stishovite – enhances the thermal motion of the metastable structure and causes instability but, most probably, does not lead to amorphization. Hence, the pressure- and temperature-quenched sample retransforms to coesite.

The transition of coesite-II to coesite-III is possibly first order in character, as it appears from the abrupt change in Raman spectra above ~35 GPa (Fig. 3.1). As expected in a first order transition, the frequency of the main mode, situated at ~600 cm^{-1}, does not vary significantly with pressure and a hysteresis is probably hindering reversible transformation from coesite-III to coesite-II.

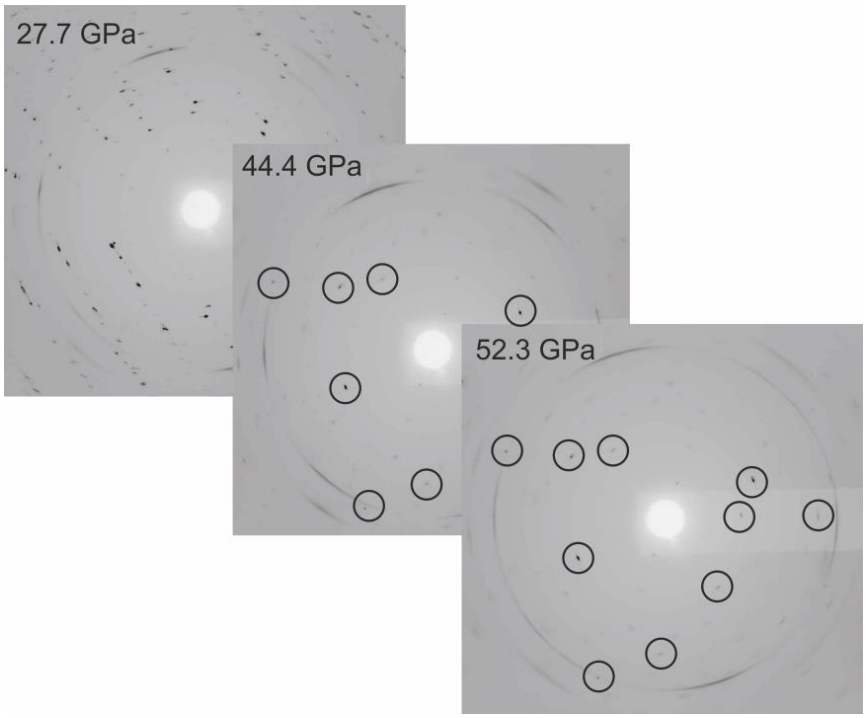

FIGURE 3.2. X-ray diffraction peaks of pressurized coesite single crystal at various pressures can be observed in wide-scan diffraction images at least up to 52.3(3) GPa, but they disappear at 54.8(3) GPa. At 27.7 GPa coesite-II phase shows prominent diffraction peaks. At higher pressures, a distinct change in diffraction pattern is observed. At 44.4 and 52.3 GPa few weak peaks of still crystalline phase coesite-III are marked by circles. Broad diffraction rings belong to neon; the figures represent diffraction region up to ~1.5 Å. Upon decompression down to ambient pressure, the material did not recover the crystallinity and no diffraction peaks were observed.

High-pressure crystal chemistry of coesite-I and its transition to coesite-II (Chapter 5)

(Published in *Zeitschrift für Kristallographie*)

This work builds upon the previous chapter by studying in detail the structure of coesite-I under pressure and it lays out the principal mechanism that leads to its transition to coesite-II. The high-pressure crystal chemistry was studied by means of single crystal X-ray diffraction (SCXRD) using synchrotron radiation. The samples were pressurized using diamond-anvil cells loaded with neon as pressure-transmitting medium.

Uncommon for other silica polymorphs, high-pressure behaviour of coesite-I is governed by two simultaneous compressional mechanisms: 1) polyhedral tilting along with Si-O-Si bond-angle reduction and 2) Si-O bond-length compression with polyhedral distortion. The two symmetrically distinct SiO_4 tetrahedra of the coesite-I structure respond differently to compression. The Si1 tetrahedral site undergoes much more distortion than the Si2 site and it is anomalously compressible relative to SiO_4 tetrahedra in other silicates. The shortest Si-O bond (related to the stiff 180º Si-O-Si angle in Si1 tetrahedron) is also the most compressible bond, in contrast to the expected behaviour under increasing pressure. The displacive phase transition from coesite-I to coesite-II above ~20 GPa is likely driven by this extreme shortening of the Si1-O1 bond (0.05 Å or 3.2%). The structure of the novel *high-P* polymorph coesite-II has reduced symmetry ($P2_1/n$) and a unit cell that is doubled (Z=32) along the *b*-axis with respect to that of the initial coesite-I ($C2/c$, Z=16). All silicon atoms in coesite-II are in tetrahedral coordination. Upon transition, the linear Si-O-Si angle bends, resulting in two independent angles, one of which, however, retains almost linear geometry (~178º). Figure 3.3 illustrates how the characteristic features in the structure of coesite-I change upon the transition to coesite-II.

The requirement of this angle to be close to linear likely causes further Si-O compression down to an extremely short distance of ~1.52 Å, which prompts subsequent structural changes, with the formation of a triclinic phase at ~31 GPa, coesite-III. This is a good example of how very short and compressible bonds are restricted to the (almost) linear Si-O-Si geometry, and appear highly unfavorable in other Si-O-Si arrangements. Building blocks of the coesite-I structure are four-membered rings (4-rings) of tetrahedra. The tetrahedra in coesite-II are rearranged in such a way that two slightly different 4-membered rings are created. Our previous Raman spectroscopy study on the pressure-induced phase transition in coesite reveals that the main A_g vibration mode of coesite at ~521cm^{-1} is a breathing mode of the 4-membered rings. The two rings in coesite-II with two slightly different sizes are expected to have breathing modes at slightly different frequencies, contributing to the appearance of a doublet in the experimental Raman spectra upon the coesite-I to coesite-II transition.

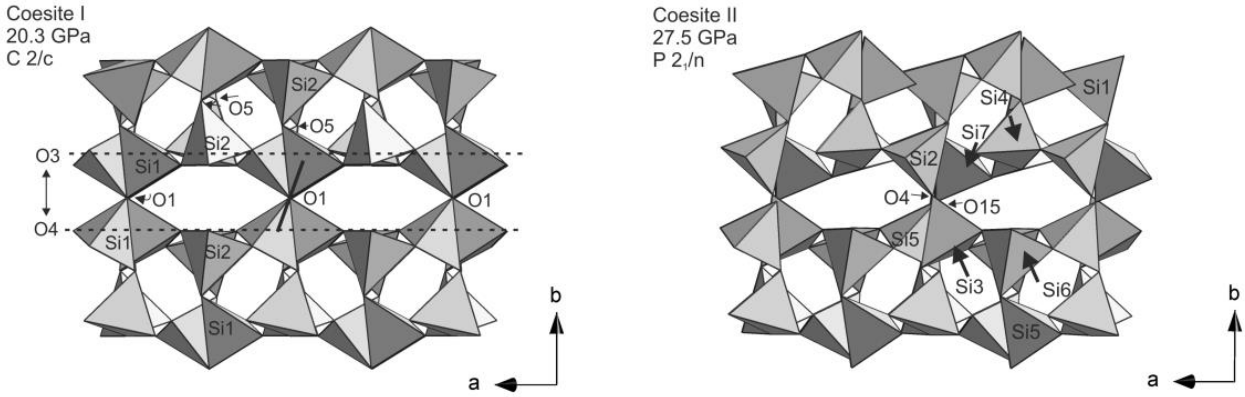

FIGURE 3.3. Structure of coesite-I at 20.3 GPa and its distortion up to transition to coesite-II (27.5 GPa) viewed down the *c*-axis. On the left, dominant features in coesite-I – symmetric hollow channels that run parallel to [001], placed between the linear Si1-O1-Si1 angles, are presented. Dashed lines indicate semi-close-packed O3 and O4 planes of oxygens in (010). On the right, in the structure of coesite-II the hollow channels parallel to the *c*-axis are asymmetric and are places between Si7-O4-Si5 (~178º) and Si2-O15-Si3 (~153º) angels. Few distinct Si tetrahedra are labeled.

High-pressure behaviour of cristobalite: bridging the gap towards the "seifertite enigma" (Chapter 6, to be submitted)

The focus of the study was to understand the formation and stability of a high-pressure polymorph cristobalite X-I, the structure of which was unknown until know. In addition, we investigated weather seifertite, the post-stishovite polymorph of silica, can form at pressures much lower than its thermodynamic equilibrium. The response of α-cristobalite to high pressures has been a subject of numerous experimental and theoretical studies for more than two decades, indicating abundant polymorphism at elevated pressures. In order to reconcile contradictory results available so far on high-pressure behaviour of α-cristobalite regarding different outcomes when the same starting material is compressed at different levels of hydrostaticity, we conducted series of experiments at high-pressures and at room temperature at variable stress conditions, using starting material in form of single crystals and powders. Understanding high-pressure behaviour of this mineral has important geological implications. In contrast to its subordinate and rather exotic terrestrial occurrence among silica phases, α-cristobalite is observed as the predominant SiO_2 polymorph in various planetary materials. It was documented alongside all the natural occurrences of the high-pressure, post-stishovite silica polymorph seifertite, related to the heavily shocked meteorites. Notably, cristobalite has also been documented in the meteorites that lack any high-pressure silica polymorphs, albeit the rest of the mineral record indicated peak shock pressures exceeding 10 GPa, at which at least coesite or stishovite should form.

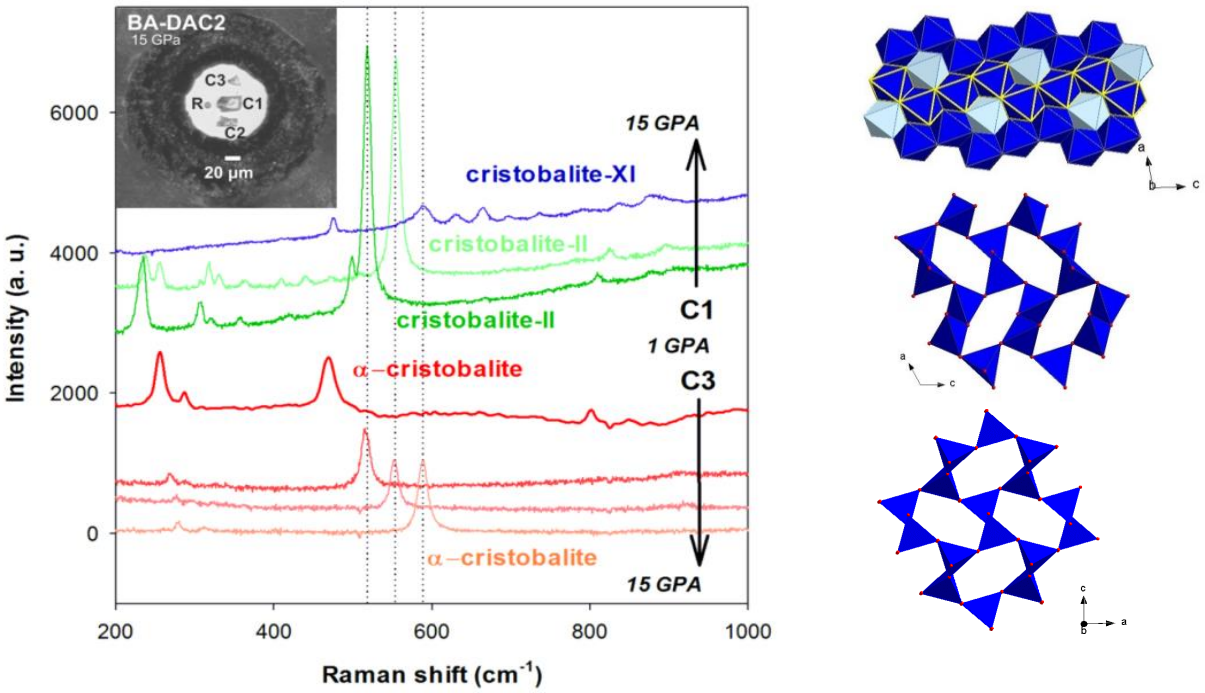

FIGURE 3.4. *In situ* Raman spectra collected on three different single crystals of α-cristobalite at 1.1, 4.6, 8.6 and 15.0 GPa and at room temperature. Inset shows the DAC pressure chamber seen at 14.1 GPa. In quasi-hydrostatic conditions the starting cristobalite (red) transforms via intermediate cristobalite-II (green) to cristobalite X-I (blue), but it retains its initial structure (orange) in the case of high hydrostaticity (smallest crystal size). The structures on the right representing the three polymorphs: α-cristobalite (bottom), cristobalite-II (middle) and cristobalite X-I (top).

Starting material in form of α-cristobalite was compressed using diamond-anvil cells. We conducted *in situ* high-pressure Raman spectroscopy and synchrotron based single-crystal X-ray diffraction (SCXRD). The experimentally determined structure was then applied in *ab initio* calculations to obtain the Raman active modes. After high-pressure treatment, recovered samples were additionally investigated by powder X-ray diffraction (PXRD) and transmission electron microscopy (TEM). We find that in highly hydrostatic environment α-cristobalite remains untransformed to at least ~15 GPa (Fig. 3.4 red spectra). Under quasi-hydrostatic conditions, intermediated by cristobalite-II (Fig. 3.4 green spectra), α-phase undergoes a first-order reconstructive phase transition to cristobalite X-I above ~10 GPa at ambient temperature (Fig. 3.4 blue spectrum). The phase X-I is found to exist at least up to ~80 GPa and to convert back to the starting cristobalite upon pressure release. We solve the structure of cristobalite X-I - a polymorph, showing that it contains kinked chains of octahedra (Fig. 3.4) similar to those in seifertite - by means of single-crystal X-ray diffraction. This polymorph shows a distorted *hcp* close-packing of oxygen atoms with randomly distributed cations. The increase in coordination number of silicon from 4 to 6 on cold compression has not been observed to occur at such low pressures (~10 GPa) in any other silica polymorph. In non-hydrostatic environment cristobalite eventually transforms to seifertite, the high-pressure silica polymorph (α-PbO_2 type) at

maximum of ~50 GPa. Seifertite formed far below its *P-T* thermodynamic stability field following the sequence of transitions α -> II -> X-I -> α-PbO_2 bypasses the equilibrium formation of stishovite and $CaCl_2$ structured polymorph, and, as reported earlier, it can be recovered to ambient conditions. Based on our observation, we conclude that particularly in quasi-hydrostatic or non-hydrostatic conditions cristobalite may occur on decompression after and could not, therefore, be used as a proof of the absence of high-pressures. Neither cristobalite nor seifertite should be considered reliable tracers of the peak shock conditions.

3.2 Conclusion

In conclusion, the compressional behaviour of the two minerals can be compared. Both coesite and cristobalite follow the same densification path initially by undergoing a displacive phase transition to a slightly distorted structure of reduced symmetry (I->II transitions). The most striking difference in response to compression of coesite and cristobalite is their reaction to (uniaxial) stress: coesite becomes amorphous when compressed in non-hydrostatic conditions; cristobalite, on the other hand, transforms directly to quenchable seifertite, a post-stishovite polymorph of silica. This difference can be explained by the fact that the collapse of the loose α-cristobalite structure leads to the formation of cristobalite X-I, which contains all Si atoms in octahedral sites at pressures as low as ~11 GPa. Under further compression only a slight rearrangement of the octahedra is required in order to form the next stable phase.

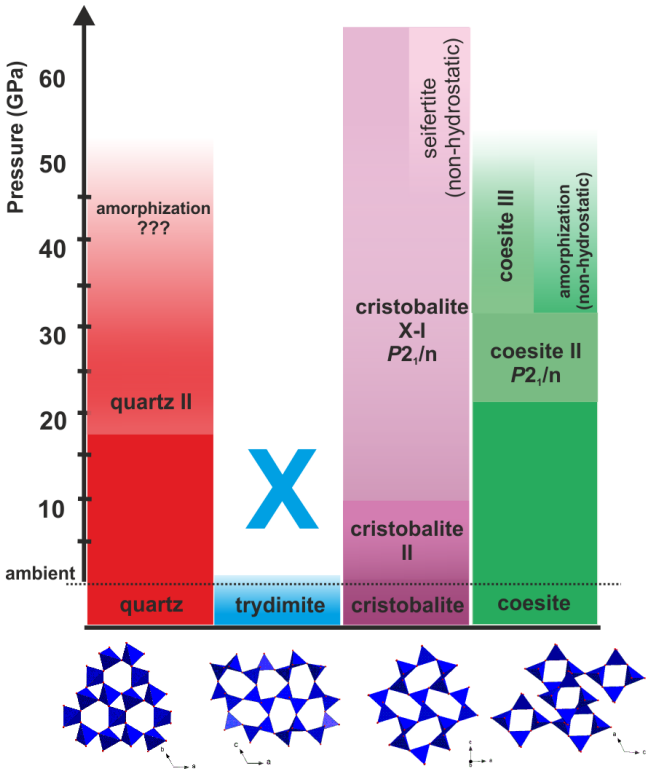

FIGURE 3.5. Schematic presentation of the pressure-induced pathways starting from various tetrahedral SiO_2 polymorphs highlighting the main contribution of this work: HP polymorphs of coesite and cristobalite. Initial polymorphs are illustrated for comparison of their characteristic ring structures. Structures according to: quartz (Glinnemann et al., 1992); cristobalite (Peacor, 1973); coesite (Angel et al., 2003); monoclinic tridymite (Kihara et al., 2005)

Coesite, on the other hand, has a very stiff structure accommodating its volume decrease almost entirely via the compressible but rigid Si1-O1-Si1 linkage, whereas the other sites in the structure are far less affected. This mechanism allows the structure to become only slightly distorted up to much higher pressures (35 GPa), hindering the structural rearrangements that would bring silicon atoms into 6-fold coordination, which is much more stable at such pressures.

In the end we briefly comment on the compressional mechanisms of all low-pressure silica polymorphs, α-quartz, α-cristobalite and coesite-I complementing our data with that available in the literature. This segment is not included in any of the manuscripts.

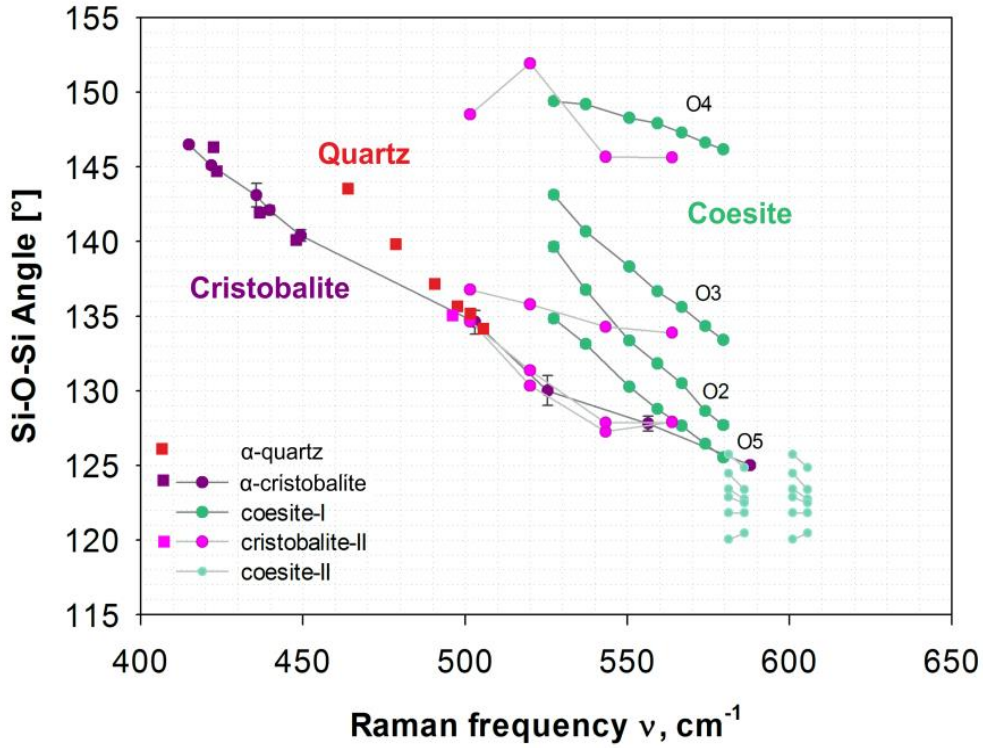

FIGURE 3.6. Correlation between the main Si-O-Si bond angle frequencies for α-quartz, α-cristobalite, cristobalite-II, coesite-I and coesite-II, after Palmer et al. (1994). The α-cristobalite and cristobalite-II Raman frequencies are from this work. Structural parameters for α-cristobalite are from this study and complemented by data from Dera et al. (2011) and references therein; they cover the pressure range from 0-14.1 GPa. Bond angles for cristobalite-II are taken from Dera et al. (2011) and references therein, covering pressures starting from 3.5 up to 10.1 GPa. Raman frequencies and bond angles for quartz are taken from Palmer et al. (1994) and references therein; they cover the pressures from ambient to 5.9 GPa. Raman frequencies and bond angles for coesite-I (2.4-20.3 GPa) and coesite-II (27.8 and 30.3 GPa) are from this work. Note that for coesite-II only the bond angles formed by breaking of the two most compressible (Si1-O2-Si2 and Si1-O5-Si2) bond angles of the coesite-I structure are shown, the rest is omitted for clarity (coesite-II has 16 bond angles). Error bars are given for α-cristobalite and coesite-I, but are mostly smaller than the symbol; error bars for coesite-II are omtitted for clarity and are not reported for quartz or cristobalite-II.

According to the available literature data, three mechanisms described as dominant in compression of silica phases: 1) Si-O-Si bond angle reduction, allowing tilting of tetrahedra, 2) Si-O bond length reduction causing tetrahedra volume decrease, and 3) tetrahedral distortion. α-quartz and α-cristobalite contain only one Si and one O in the asymmetric unit, therefore only one Si-O-Si angle. Coesite-I has Si1 and Si2 sites and five characteristic Si-O-Si angles. Complementing an earlier plot of the Raman frequency of the main stretching mode *v* against Si-O-Si angle (Fig. 3.6) with spectroscopic and structural data from this study, we can conclude that a structure of a mineral is likely to become unstable when this angle approaches ~125°, regardless the pressure. Data for α-quartz are unfortunately incomplete.

Regarding decrease of the tetrahedra volume with pressure (Fig. 3.7), this mechanism contributes more to the compression of the stiff coesite-I structure (K_0=96(4) GPa) than to compression of loose α-cristobalite (K_0=11.0(4) GPa) and α-quartz (K_0=38.7(3) GPa). To our knowledge, the remarkable compressibility of the Si1 tetrahedral site in coesite-I can only be compared to that zircon and forsterite (summarized in Smyth et al. 2000). Note, however, that in such structures the tetrahedra do not form three-dimensional framework as in the case of coesite-I.

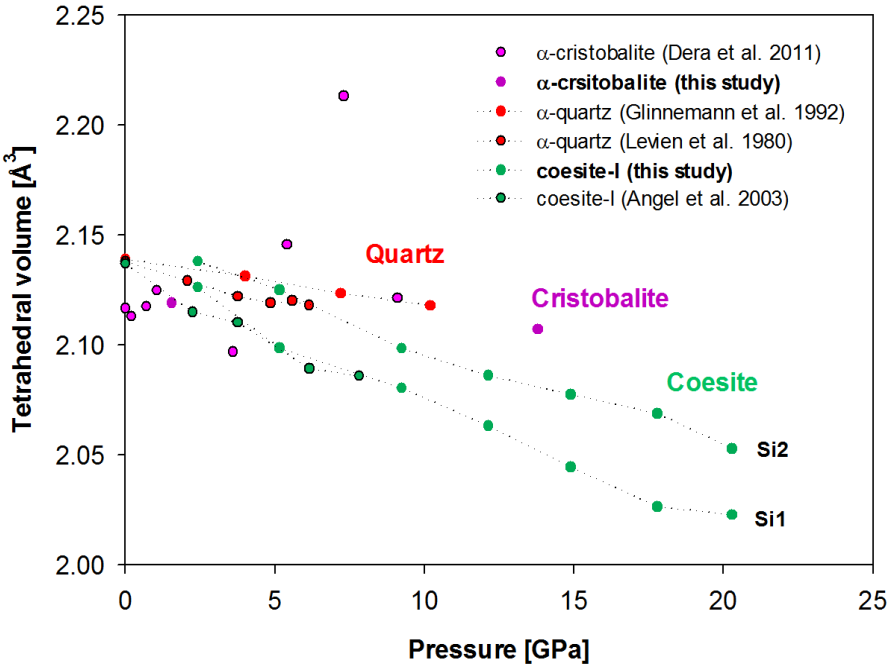

FIGURE 3.7. Tetrahedral volume decrease of selected silica polymorphs with increasing pressure.

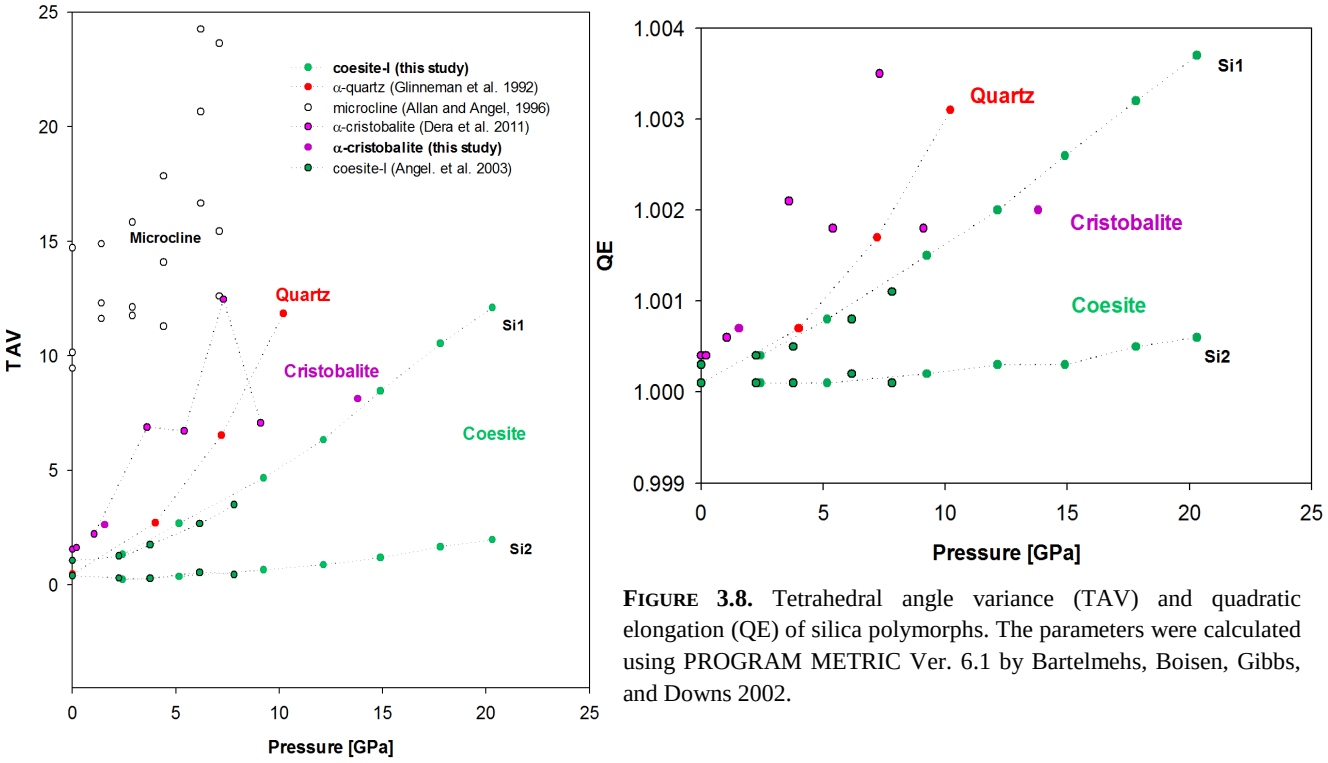

FIGURE 3.8. Tetrahedral angle variance (TAV) and quadratic elongation (QE) of silica polymorphs. The parameters were calculated using PROGRAM METRIC Ver. 6.1 by Bartelmehs, Boisen, Gibbs, and Downs 2002.

On the other hand, tetrahedral distortion seems to be the prevalent mechanism of compression in α-quartz (Fig. 3.8). α-cristobalite and the Si1 site of coesite are distorted to similar extent, but the Si2 site in coesite-I seems to remain almost undistorted under compression. Available data on α-cristobalite are scattered but the last pressure point we obtain at 14.1 GPa shows significantly better crystal quality and refinement statistics (R_{int}= 2.1 %; R_1= 6.7%) than those reported by Dera et al. (2011), therefore we consider our data more reliable. Tetrahedral distortion can be quantified by two parameters, tetrahedral angle variance (TAV) and quadratic elongation (QE). Angle variance is a measure of the distortion of the intra-polyhedral bond angles from the ideal polyhedron and Quadratic elongation is a measure of the distortion of bond lengths from the ideal polyhedron as defined by Robinson et al. (1971). Represented in Figure 3.8, both TAV and QE show similar pattern for the three minerals. For comparison we also plot common feldspar, which in addition to the Si-tetrahedra, also contains Al-tetrahedra and cations in the structural cavities and is therefore much more distorted.

3.3 List of authors contributions

Černok, A., Ballaran, T., Caracas, R., Miyajima, N., Bykova, E., Prakapenka, V., Liermann, H., Dubrovinsky, L. "**Pressure-induced phase transitions in coesite**". *American Mineralogist* 99, 755-763 (2014). DOI:10.2138/am.2014.4585

Č.A. designed and performed all DAC experiments at BGI; Č.A., B.E. and L.D. collected data at synchrotrons; C.R. performed theoretical computation; M.N. analyzed recovered sample with TEM; Č.A., and B.T. analyzed all data, Č.A., BT and L.D. discussed all data; Č.A. wrote the manuscript; all coauthors read the manuscript.

A. Černok, E. Bykova , T.B. Ballaran , H.P. Liermann , M. Hanfland and L. Dubrovinsky. **''High-pressure crystal chemistry of coesite-I and its transition to coesite-II''**. *Zeitschrift für Kristallographie - Crystalline Materials* 229, 761-773 (2014). DOI:10.1515/zkri-2014-1763

A. Č. designed and prepared DAC samples; A. Č., E.B. and L.D. collected data at synchrotrons; A. Č. and T.B.B. analyzed all data; E.B. solved the structure of coesite-II. A. Č., T.B.B. and L.D. discussed all data; A. Č. wrote the manuscript; all coauthors read the manuscript.

A. Černok, K. Marquardt, R. Caracas, E. Bykova, G., H. P. Liermann, M. Hanfland, M. Mezouar, and L. Dubrovinsky. **High-pressure behaviour of cristobalite: bridging the gap towards the "seifertite enigma".** To be submitted

A. Č. designed and performed all DAC experiments; K.M. and A. Č. collected TEM data; R.C. performed theoretical calculations; A. Č, E.B and L.D. collected synchrotron data; E.B. and L.D. solved the structure of cristobalite X-I; A. Č. analyzed all data; A. Č and L.D. discussed all data with K.M. and R.C; A. Č. wrote the manuscript; all coauthors read the manuscript.

4. PRESSURE-INDUCED PHASE TRANSITIONS IN COESITE

Ana Černok,[1] Tiziana Boffa Ballaran,[1] Razvan Caracas,[2] Nobuyoshi Miyajima,[1] Elena Bykova,[1] Vitali Prakapenka,[3]Hanns-Peter Liermann,[4] and Leonid Dubrovinsky[1]

[1]Bayerisches Geoinstitut, Universität Bayreuth, Universitätsstrasse 30, D-95440 Bayreuth, Germany

[2]Centre National de la Recherche Scientifique Laboratoire de Geologie de Lyon (LGLTPE) UMR 5276 Ecole Normale Supérieure de Lyon 46, allée d'Italie, 69364 Lyon, France

[3]Center for Advanced Radiation Sources, The University of Chicago, Argonne National Laboratory, Building 434A, 9700 South Cass Ave, Argonne, IL 60439, USA

[4]Photon Sciences, Deutsches Elektronen-Synchrotron (DESY), Notkestraße 85, 22607 Hamburg, Germany

American Mineralogist **99**, 755-763 (2014), DOI:10.2138/am.2014.4585

4.1 Abstract

High-pressure behaviour of coesite was studied on single crystals using diamond-anvil cells with neon as the pressure transmitting medium by means of in situ Raman spectroscopy up to pressures of ~51 GPa. The experimental observations were complemented with theoretical computations of the Raman spectra under similar pressure conditions. We find that coesite undergoes two phase transitions and does not become amorphous at least up to ~51 GPa. The first phase transition (coesite I to coesite-II) is reversible and occurs around 23 GPa. The second transition (coesite-II to coesite-III) at about 35 GPa is also reversible but involves a large hysteresis. Samples recovered from the highest pressure achieved, ~51 GPa, show Raman spectra of the initial coesite. The ab initio calculations gave insight into the initiation mechanism of the first phase transition, implying, from the analysis of unstable phonon modes, that it is probably a displacive phase transition due to shearing of the four-membered rings of SiO_4 tetrahedra upon compression. The transition to the lowest-symmetry phase, coesite-III, is possibly a first order phase transition which leads to a very distinct structure. None of the metastable high-pressure phases of coesite has been previously studied and it was widely accepted that coesite undergoes pressure-induced amorphization at significantly lower pressures (30 GPa). The study of the high-pressure behaviour of coesite is important to better constrain the metastable phase

diagram of silica. Further crystallographic investigations are necessary for characterizing the structures of these metastable coesite forms. Crystalline or amorphous metastable phases derived from coesite under high-pressure conditions are of particular interest because they can be used as potential tracers of peak transient pressures (stress) reached in processes such as impacts or faulting.

4.2 Introduction

Silica, SiO_2, exhibits a very rich polymorphism with more than 30 stable or metastable phases, most of which occur at ambient to moderate pressures (< 9 GPa). Some of these phases, such as quartz, trydimite and cristobalite consist of frameworks of SiO_4 tetrahedra and are abundant in nature. Phases of silica stable at higher pressures and temperatures are mostly composed of octahedrally coordinated silicon atoms. Coesite, thermodynamically stable above ca. 2.5 GPa and at temperatures in excess of 500 °C, is the densest known polymorph with silicon atom tetrahedrally coordinated to oxygen. This polymorph was first observed experimentally by Coes (1953) and later discovered in nature by Chao and coworkers, in impact breccia from Meteor Crater (Chao et al., 1960). Nowadays coesite is widely accepted as a high-pressure indicator in rocks related to meteorite impact sites, where it forms due to the high-pressure and high-temperature regime of the impact and to the very rapid quenching conditions which prevent a reversion from coesite to quartz (e.g., Xiao et al., 2011). Shock-induced formation of coesite has been also observed in meteorites, where it can be found along with other shock minerals (e.g., Ohtani et al., 2011). Terrestrial occurrence of coesite was reported from deeply (>100 km) subducted crustal rocks (ultra-high pressure metamorphic rocks) or mantle derived rocks (kimberlites), which have been exhumed under conditions that prevent retrograde transition to quartz (e.g., Chopin, 1984; Korsakov et al., 2007; Mosenfelder and Bohlen, 1997; Parkinson, 2000; Ruiz-Cruz and Sanz de Galdeano, 2012; Smyth and Hatton, 1977). In these rocks coesite commonly occurs as an inclusion within clinopyroxene, olivine, garnet or diamond. Coesite-in-diamond assemblage was recently introduced as an important high-pressure barometer (Sobolev et al., 2000).

Because of the relatively strong Si-O bonding in silica, there are high kinetic barriers associated with the transitions to stable high-pressure phases consisting of SiO_6 octahedra (Haines et al., 2001). This results in complicated metastable phenomena at high pressures and ambient temperature such as the persistence of low-pressure phases far out of their stability fields and transitions to metastable crystalline and amorphous phases. Slow kinetics, enhanced metastability, formation of poorly crystallized or structurally disordered materials usually give rise to weak X-ray diffraction patterns which are difficult to interpret, resulting in contradictory interpretations. Another major complexity in

studying the behaviour of silica also arises from the fact that the transition mechanisms, the pathways through intermediate metastable phases and the onset of pressure-induced amorphization strongly depend on the starting polymorph, as well as on the hydrostaticity and stress anisotropy present in the sample during experiments. For example, experimental studies on polycrystalline α-quartz in neon pressure medium (Kingma et al., 1993) evidenced pressure-induced phase transitions above 21 GPa to a crystalline metastable phase of reduced symmetry, followed by pressure-induced amorphization above 30 GPa. In helium pressure medium, which provides higher hydrostaticity, polycrystalline quartz is found to remain crystalline up to 45 GPa and to transform to a monoclinic phase at such pressure (Haines et al. 2001). A transformation path through several metastable phases has been reported in cristobalite, as well (e.g., Dera et al., 2011; Prokopenko et al., 2001; Yagi and Yamakata, 2000). Numerical calculations also stressed the fact that stable polymorphs of SiO_2 may undergo a number of phase transitions to metastable phases with increasing pressure before reaching amorphization (Teter and Hemley 1998; Wentzcovitch et al. 1998).

In an experimental study on the high-pressure behaviour of coesite, Hemley (1987) observed changes in the Raman spectra of coesite collected at ambient temperature and at the pressures of 22-25 GPa in argon pressure medium, and reported that coesite becomes amorphous above 30 GPa. The authors attributed such changes to a high-pressure phase transformation occurring in coesite; however, no further investigation has been reported to better describe such behaviour.

In this study we aim at giving insight into the high-pressure behaviour of coesite. We measure in situ Raman spectra at pressures up to 51 GPa and complement them with theoretical computations of Raman spectra under similar pressure conditions. We find two phase transitions clearly distinguishable by Raman spectroscopy and explain the mechanism of the first transition based on the theoretical calculations.

4.3 Experimental methods

4.3.1 Synthesis

The starting material for the coesite synthesis was SiO_2 glass powder with very low trace elements content, as analyzed at the BGI using LA-ICP-MS: Al 20 ppm, Ge 1.3 ppm, Na 1.0 ppm, Li 0.8 ppm, and B, Ti, Fe, Ga, Rb and Sn below the detection limits. Coesite single crystals were synthesized by mixing the starting powder with ~5 wt% distilled water inside a platinum capsule, which was then welded shut. The capsule was first placed into pyrophyllite sleeves and then in a 0.5" talc-pyrex

piston-cylinder assembly containing internal, tapered graphite resistance furnaces (Bromiley and Keppler, 2004). The mixture was pressurized to 3.5 GPa and slowly heated up to 1250 °C, kept at this temperature for ~15 hours, then cooled down to 1100 °C in 5 hours, and finally quenched. Slow cooling procedure and water-saturated conditions resulted in growth of relatively large (above 100 µm in linear dimensions) crystals. No Raman peaks were observed in the spectra of synthesized coesite in the O-H vibration region (2800-3400 cm^{-1}). This is in agreement with the study on pressure dependence of hydrogen solubility in coesite (Koch-Muller et al., 2001; Mosenfelder, 2000), according to which no water should be present in coesite synthesized at 3.5 GPa and 1250 °C.

4.3.2 High-pressure Raman spectroscopy

Piston-cylinder type diamond anvil cells (DAC) developed at BGI (Kantor et al. 2012) made of high-temperature resistant alloy were used for the high-pressure experiments. Experiments in quasi-hydrostatic conditions were carried out using 250 µm culet size diamonds, a cylindrical pressure chamber of 30-40 µm height and ~125 µm diameter drilled in a pre-indented rhenium gasket. We used neon as pressure transmitting medium, loaded using the BGI gas loading system (Kurnosov et al. 2008). Selected crystals were in the form of plates of typical size 15 x 30 x 50 $µm^3$ and they were loaded together with a ~5 µm in diameter ruby sphere for pressure determination. The pressure was determined using the ruby luminescence line (Mao et al. 1986).

Raman spectroscopy measurements were performed using a LabRam system (Horiba Scientific Inc.) with a He–Ne-laser (excitation wavelength 632.8 nm, output power 0.15 W, spectral resolution 2 cm^{-1}) as well as Dilor XY Raman spectrometer with Ar+ ion laser (514.5 nm, Coherent Innova 300, spectral resolution 1 cm^{-1}). The output power was varied according to the sample signal between 0.3 and 1.0 W when using the Dilor instrument. The spectrometers were calibrated using either the silicon peak at 520 cm^{-1} or referencing the value of the absolute wavelength of the ruby R_1 fluorescence line. Raman spectra were collected between 200 and 1200 cm^{-1}. This region is optimal because the LabRam spectrometer used in our experiments is equipped with a notch filter which prevents collection of the frequencies lower than 150 cm^{-1}, whereas above 1200 cm^{-1} low intensity peaks of coesite are suppressed by strong diamond peak at centered near 1300 cm^{-1}. We performed five different DAC experiments at room temperature by pressurizing the coesite crystals in steps of several GPa up to a maximum of ~51 GPa. In two of these experiments, Raman spectra were also collected during decompression. Peak positions in the Raman spectra were determined by fitting to Lorentzian peak shape using Igor Pro v. 6.22 software.

4.3.3 External electrical heating in DAC

Heating experiments up to ~400 ºC were performed using platinum-wire resistive whole-cell heater. The heater has an external diameter of 50 mm, it is made of fired pyrophyllite and 0.5 mm in diameter platinum wire is folded over the inner surface of the heater. For the purpose of protecting the Raman spectrometer from heating over several hours, we used a thermal insulator that is made of a square-shaped double-layered stainless steel box. Stainless steel of "type 1.4571" is oxidation-resistant at elevated temperatures and shows no oxidation effect to at least 600 °C (Fig. 4.1). The DAC and the whole-cell heater were fixed on a stainless steel holder, which was then placed inside the steel box with openings at the bottom and the top, to allow optical access. Temperature was measured using a Pt Pt/Rh S-type thermocouple placed in the vicinity of the gasket.

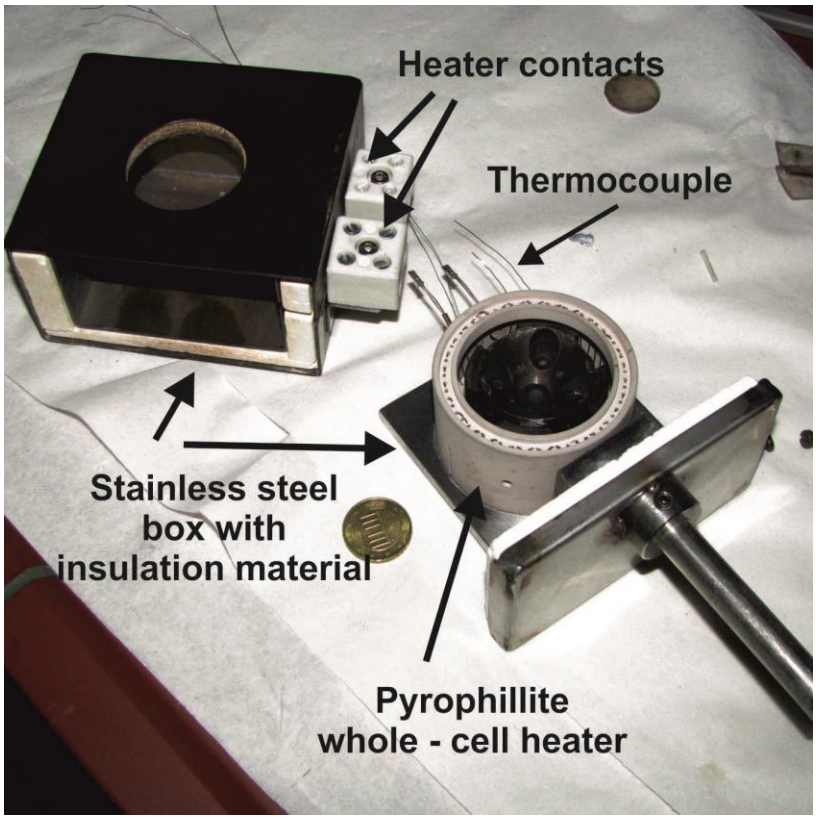

FIGURE 4.1. External heating assembly, consisting of a pyrophillite whole cell heater surrounding DAC placed on a stainless steel holder and double-layered stainless-steel insulation box. The coin is used as a scale marker.

In the first experiment, the coesite sample was pressurized at room temperature up to 29 GPa and then slowly heated up to 400 ºC. During heating up to 200 °C the pressure dropped down to 27 GPa and was readjusted before further heating. In a second experiment, the coesite sample was pressurized from room pressure up to 34 GPa and then slowly heated up to 200 °C. At this temperature, however,

the Raman spectrum was very poor and therefore the experiment was interrupted. Pressure was monitored from a position of the ruby fluorescence peaks corrected for temperature after (Rekhi et al., 1999).

4.3.4 Transmission Electron Microscopy

Conventional TEM characterizations in bright-field and dark-field imaging and selected electron diffraction techniques were carried out with a Philips CM20FEG equipped with an energy dispersive X-ray (EDX) analyzer, operated at 200 kV. Analyses were performed on several chips of a crystal which was subjected to a maximum pressure of 35 GPa. The recovered material was first characterized by Raman spectroscopy and then further crushed between two tungsten carbide plates. The ethanol dispersion was placed on a lacey carbon film on Cu-grid (300 mesh). Selected area electron diffraction (SAED) patterns from different chips were obtained to distinguish between crystalline and amorphous domains or particles. The chemistry of the grains was also cross-checked using EDX spectroscopy.

4.3.5 X-ray diffraction

We selected coesite single crystals at BGI using a rotating anode high-brilliance Rigaku diffractometer with Mo Kα radiation, equipped with Osmic focusing X-ray optics and Bruker Apex CCD detector.

The crystal recovered after a repeated experiment at 34 GPa and ~300 ºC was analyzed by means of single-crystal X-ray diffraction at the beamline 13IDD of the GSECARS at the Advanced Photon Source, Argonne National Laboratory, USA. An incident monochromatic beam with wavelength of 0.3344 Å was focused to a spot of 4x8 μm^2. Diffraction images were collected using a MAR165 CCD detector with sample-to-detector distance of approximately 250 mm. The sample was also analyzed by X-ray diffraction mapping along a 5 x 5 points, covering an area of 12 x 12 μm^2 (step size 3 µm), with exposure time of 10 s at each point. Diffraction images were integrated using the Fit2d software (Hammersley 1996).

4.3.6 *Ab initio* calculations

We analyze the pressure dependence of the phonon spectra also from the first-principles calculations. We determine the ground-state properties using standard density-functional theory (Kohn and Sham, 1965; Martin, 2004; Payne et al., 1992) in the ABINIT implementation, based on planewaves and pseudopotentials (Gonze et al., 2009, 2002). Starting from the crystal structure refined by Angel et al. (2003) we determine the theoretical structure of coesite up to 40 GPa in 10 GPa steps. Then we

compute the energy derivatives to build the dynamical matrices and the Raman tensors in the framework of the density-functional perturbation theory (Baroni et al., 2001; M. Veithen, 2005; Gonze et al, 2005). We employ a 4x4x4 grid of special k points (Monkhorst and Pack, 1976) to sample the electron density in the reciprocal space and a kinetic energy cutoff of 38 Hartrees (1 Hartree = 27.2116 eV). With these parameters the precision of the calculation is typical on the order of 0.001 Hartree in energy and better than 1 GPa in pressure. We store all the Raman spectra computed under pressure on the WURM website (http://www.wurm.info). More details of the Raman calculations can be found in the original WURM paper (Caracas and Bobocioiu, 2011).

4.4 Results

4.4.1 High-pressure, room temperature Raman spectroscopy

Selected Raman spectra collected during compression are shown in Figure 4.2. At ambient pressure coesite shows prominent peaks at 202, 261, 322, 352, 371, 425, 469 and 519 cm^{-1}, with the last peak being the most intense. The intensities and positions of these peaks are in good agreement with previous studies (Sharma et al. 1981; Boyer et al. 1985; Hemley 1987). The peaks that are expected to be centered around 665 cm^{-1} and 785 cm^{-1} at ambient pressure have only been observed at elevated pressures and not in all experiments. A peak located at 815 cm^{-1} was observed starting from ambient conditions, but was not detected in all experiments. Another peak, not previously reported in high-pressure Raman spectroscopy studies of coesite, was observed in two experiments. It appeared at and above 4.5 GPa, and, according to its pressure shift, it can be expected to occur around 860 cm^{-1} at ambient conditions. Raman bands at 1036 and 1164 cm^{-1} were observed at ambient conditions outside the DACs, but not under compression due to their very low intensities. All the vibration bands are significantly weaker than the main 519 cm^{-1} band, they all show continuous positive pressure shift during compression and can be followed up to ~28 GPa (Fig. 4. 2a). The bands located at 519, 665, 785 and 815 cm^{-1} have the largest pressure shifts, in good agreement with the previous study by Hemley (1987).

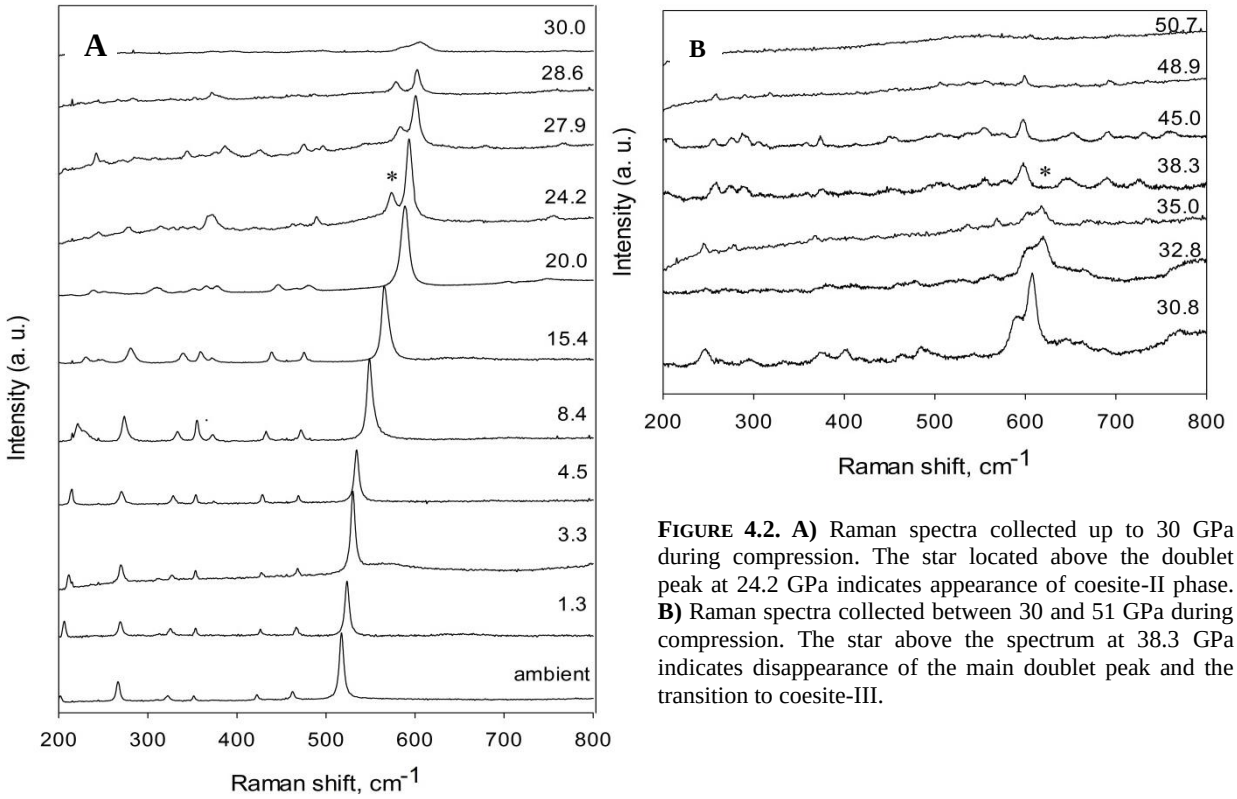

FIGURE 4.2. A) Raman spectra collected up to 30 GPa during compression. The star located above the doublet peak at 24.2 GPa indicates appearance of coesite-II phase. **B)** Raman spectra collected between 30 and 51 GPa during compression. The star above the spectrum at 38.3 GPa indicates disappearance of the main doublet peak and the transition to coesite-III.

The most intense 519 cm^{-1} band was described as v_s(Si-O-Si) symmetric stretching mode with A_g symmetry (Sharma et al. 1981, and references therein). It shows continuous positive pressure increase up to 23 GPa. Above 23 GPa a new strong vibrational band appears at a frequency of about 20 cm^{-1} lower than the main Raman peak, which at this pressure has a frequency of 593 cm^{-1}, as was also observed by Hemley (1987). Several other new modes become visible at lower frequencies, confirming the results reported by Hemley (1987) and their interpretation of a possible phase transition to a phase with reduced symmetry or enlarged unit cell. This post-coesite phase, hereafter referred as coesite-II, can be followed upon compression up to ~35 GPa (Fig. 4.2b). The A_g mode persists up to ~35 GPa, although its intensity decreases significantly. Above ~35 GPa, the two high-frequency peaks disappear; only one new peak centered around ~600 cm^{-1} can be observed (Fig. 4.2b). This sudden change in the Raman spectrum indicates a possible discontinuous transition to a new phase, hereinafter referred as to coesite-III. On further compression up to ~51 GPa, the peak centered around ~600 cm^{-1} decreases in intensity and exhibits a very small pressure increase (Fig. 4.2b). Above ~35 GPa, in addition to the peak centered around ~600 cm^{-1}, new bands appear as two triplets of equally spaced peaks between ~250-300 cm^{-1} and between ~620-720 cm^{-1}. Appearance of a large number of new vibrational modes may indicate that coesite-III has either an enlarged unit cell or

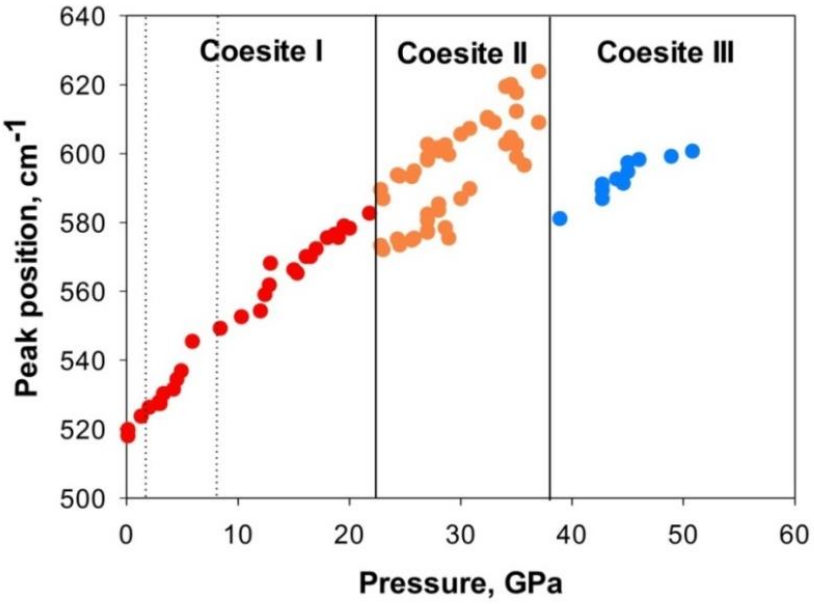

FIGURE 4.3. Pressure dependence of the main Raman active mode obtained from several different experiments at ambient temperature. Phase transitions at ~23 and ~35 GPa are indicated by solid lines, and the thermodynamic stability field of coesite is indicated by dotted lines.

lower symmetry with respect to coesite-I and II structures. At ~51 GPa no vibrational modes can be observed. The pressure dependence of the main 519 cm^{-1} Raman mode ($d\nu/dP$), where ν is the ambient-pressure phonon frequency and P is the pressure) was derived from a series of experiments and it is, on average, 3.0 ± 0.4 cm^{-1}/GPa (Fig. 4.3). Based on the zero-pressure bulk modulus K_{T0}= 100.8 ± 0.5 GPa reported by Angel et al. (2001) and using the formulation of the mode-Grüneisen parameter as $\gamma_\nu = (K_{T0}/\nu)(d\nu/dP)$, we obtain a value of 0.58 ± 0.08 for the A_g mode, only slightly higher than the values reported in Hemley (1987).

At the highest pressure reached in these experiments, about 51 GPa, the Raman spectrum of coesite almost vanishes. Under decompression the vibrational modes of coesite-III regain intensity, with the most prominent peaks visible at ~250, ~540 and ~580 cm^{-1}. Their frequencies decrease continuously down to ~24 GPa without any abrupt change, suggesting that the structure of coesite-III is preserved down to 24 GPa and that the transition to the coesite-II phase is not reversible or has a very large hysteresis. A strong single band centered around 600 cm^{-1} appears at ~24 GPa and its intensity increases with further decompression, until it dominates the Raman spectra below ~20 GPa, suggesting that the structure of coesite has been retrieved. Indeed, the Raman spectrum of the recovered crystal at room pressure is identical to that of the starting material (Fig. 4.4). The fact that

the pressure-quenched material is crystalline coesite strongly suggests that the high-pressure phase coesite-III was also crystalline at 51 GPa even if the Raman vibrations could not be observed.

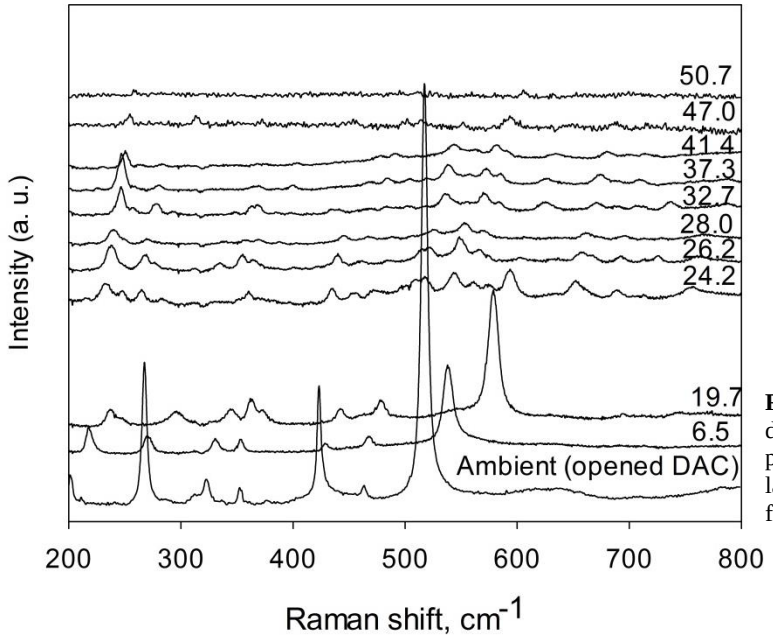

FIGURE 4.4. Raman spectra collected during decompression from ~51 GPa to ambient pressure. Note that the power of the incident laser beam was decreased below 20 GPa from 1.0 to 0.3 W.

4.4.2 Raman active modes from ab initio calculations

We compute the phonons in the Brillouin zone-center, with both frequencies and atomic displacement patterns, for coesite I up to 40 GPa. We equally determine the Raman tensors and compute the Raman intensities for the Raman-active modes. All the spectra are reported on the WURM website (http://www.wurm.info), but for sake of clarity only the spectrum at ambient pressure is represented here, in Figure 4.5a. Figure 4.5b shows pressure dependence of selected most dominant modes. The Raman spectra are dominated by the A_g mode situated at ~510 cm^{-1} at ambient pressure. A series of low intensity peaks are observed at frequencies higher than 600 cm^{-1}, in excellent agreement with the experimental data.

The strongest A_g mode, located at ~510 cm^{-1} at ambient pressure (at 541 cm^{-1} at 10 GPa) is a breathing mode of the four-membered rings comprised of SiO_4 tetrahedra (Fig. 4.6a) and it arises from bending of four different Si-O-Si bonds that vibrate in phase, namely Si-O2-Si, Si-O3-Si, Si-O4-Si and Si-O5-Si (nomenclature after Angel et al. 2003, see Figures 2 and 4 in the cited reference). Except for the Si-O4-Si bond angle, which changes by only a few degrees throughout the pressure range examined by Angel et al. (2003), other three bond angles show strong pressure dependence. In contrast to these four angles, Si-O1-Si is rigid due to symmetry constrains and remains 180º throughout the

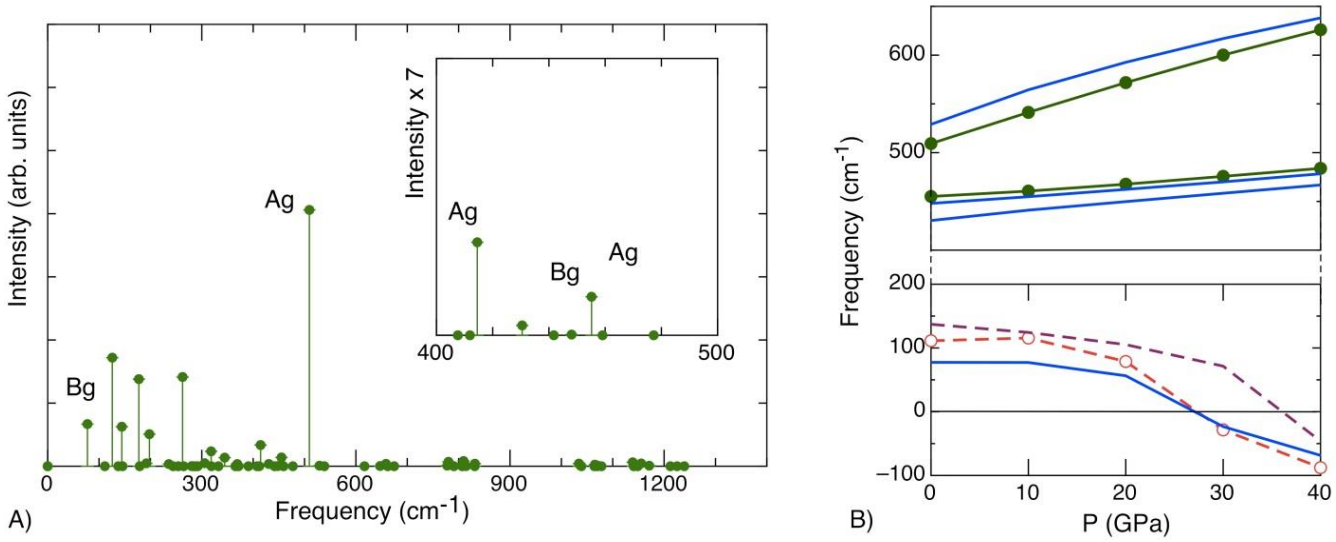

FIGURE 4.5. (A) Theoretical Raman spectrum at ambient conditions. The spectrum is dominated by the strong A_g mode at 510 cm^{-1}. Several peaks are visible at low frequencies and the most intense is the Bg mode at 77 cm^{-1}, while all peaks above 600 cm^{-1} are very weak. A few peaks are symmetry-labeled. The inset shows the peaks occurring in the 400-500 cm^{-1} range, with intensity magnified, with the B_g mode at 430 and the A_g mode at 455 cm^{-1}. (B) Pressure variation of selected modes in coesite-I. Note that the lowest frequency modes become unstable with increasing pressure. The A modes bear symbols; the g modes are represented with solid line; the dashed line represent modes that are only infrared active. Three modes become unstable between 20 and 30 GPa, including a B_g Raman active mode at 77cm^{-1} and an A_u infrared active at 111 cm^{-1} (ambient conditions). These two modes are displayed in Figure 4.6c and d at elevated pressure.

investigated range. Atomic movements of this breathing A_g mode are illustrated in a representative four-membered ring in Figure 6a seen during contraction. The largest displacement is seen in O3 and O4 atoms, which are moving symmetrically inward, and in O5 atoms that are moving parallel to each other along a-axes, but in the opposite direction.

A B_g mode that appears at 77 cm^{-1} at ambient conditions (also 77 cm^{-1} at 10 GPa and 56 cm^{-1} at 20GPa) is dominant in the lower frequency region and shows softening with increasing pressure (Fig. 4.5b), similar to previous experimental studies (Hemley 1987). This mode corresponds to shearing of the tetrahedra rings (Fig. 4.6b and c) and may have a significant influence on the structural distortion at elevated pressures. Shearing of the four-membered rings is illustrated by the two adjacent four-membered rings shown in Figure 4.6b. Within the same ring O3 atoms are displaced in the same direction, but this displacement direction is opposite between the two adjacent rings. O2 atoms vibrate opposite to the O3 displacement direction. Within the ring, one of the O4 atoms moves downwards and the other upwards from the plane of the ring. All O5 atoms of the structure move in the same direction, in the plane of the SiO_4 rings. Similar intensity variation is observed in an A_u mode that appears at 115 cm^{-1} at ambient pressure (Fig. 4.5b). Above 20 GPa this infrared active mode becomes even more unstable than the Raman active 77 cm^{-1} mode; this enhances the

displacement of the O1 atom from the rigid 180º Si-O1-Si bond (Fig. 4.6d). Then this displacement could initiate the structural changes that we observe above 24 GPa. However, an IR study is required in order to confirm this prediction. For a better visualization of the atomic motions, please visit the WURM website.

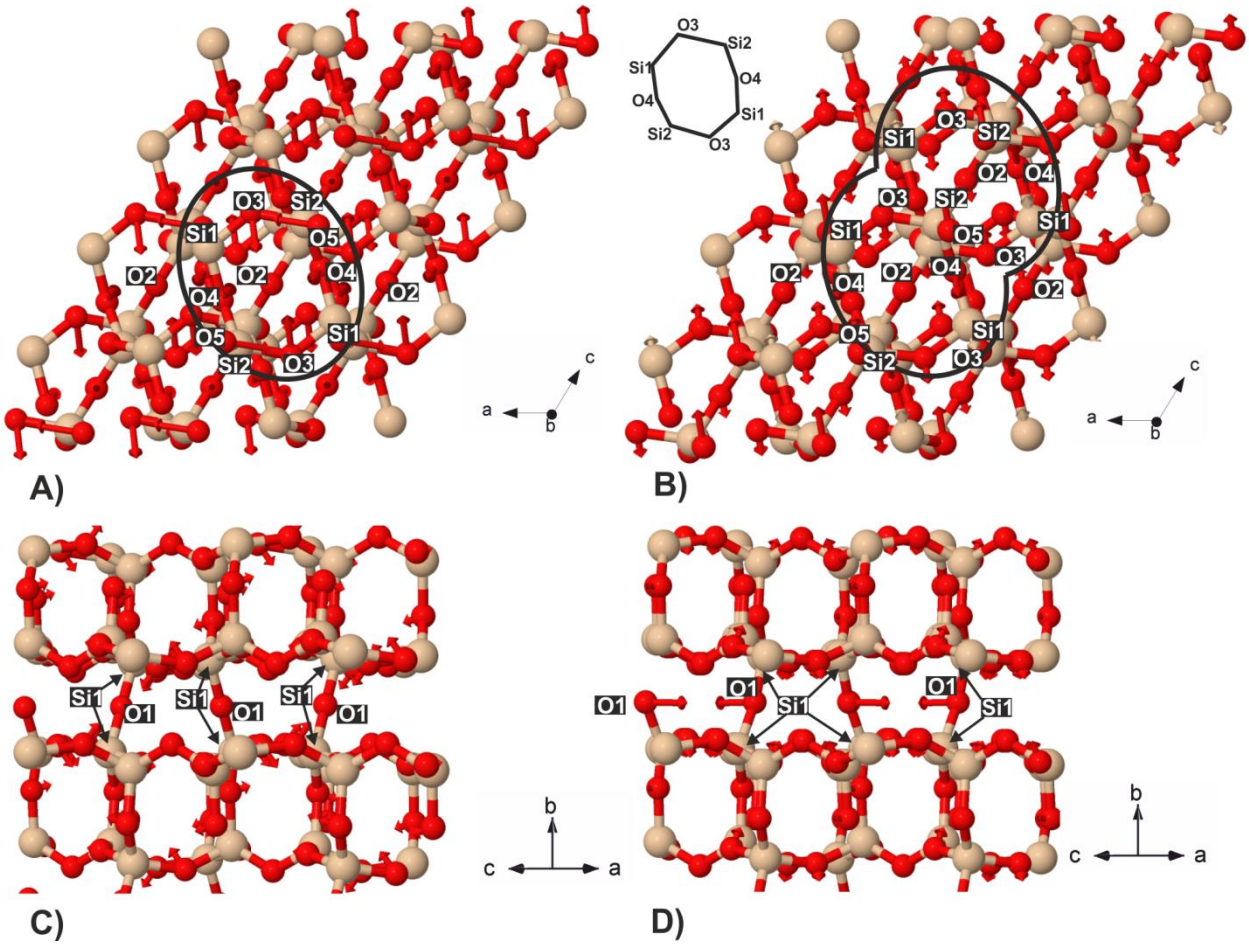

FIGURE 4.6. Atomic displacement pattern of some of the most representative Raman modes of coesite at 10 GPa. They dominate the Raman spectra and their behavior is likely responsible for the structural changes exhibited under pressures. White corresponds to silicon atom, grey is oxygen; atomic nomenclature is after Angel et al. (2003). Ellipses are surrounding representative SiO_4 rings and grey arrows placed on oxygen atoms are indicating displacement directions. **A)** The strongest A_g mode at 541 cm^{-1} (located at 510 cm^{-1} at ambient pressure) is a breathing mode of the four-membered tetrahedral rings. **B)** The B_g mode at 77 cm^{-1} (also 77 cm^{-1} at 10 GPa) dominates the spectra at low frequencies and it corresponds to shearing of the four-membered silica rings. The sketch in the upper left corner on the figure is for simplifying the structure of one ring. **C)** The same B_g mode at 20 GPa (56 cm^{-1}) in different crystallographic orientation. **D)** Infrared active Au mode at 20 GPa (78 cm^{-1}) showing significant displacement of the O1 atom from the rigid 180 ºSi-O1-Si bond.

Other two modes in the 400-500 cm^{-1} region (Fig. 4.5a) are correlated with the motion of the SiO_4 tetrahedra rings, although they have low intensity. One is a complex B_g mode at 430 cm^{-1},

corresponding to both breathing and shearing of the SiO_4 tetrahedra rings, and the other one is an A_g mode at 455 cm^{-1}, which arises from stretching of the rings. The 430 cm^{-1} mode has not been observed experimentally, but the 455 cm^{-1} mode, albeit very weak, was present in some of our spectra.

4.4.3 High-temperature, high-pressure Raman spectra

The Raman spectra collected at 27-29 GPa up to 400 °C and at 34 GPa up to 200 °C are shown in Figure 4.7a and b, respectively. The first heating experiment was carried out in the pressure range where coesite-II phase (Figs. 4.2a and b) was observed, and, as expected, the main feature in the Raman spectra is the peak doublet located ~600 cm^{-1} (Fig. 4.7a). The intensity of the vibrational

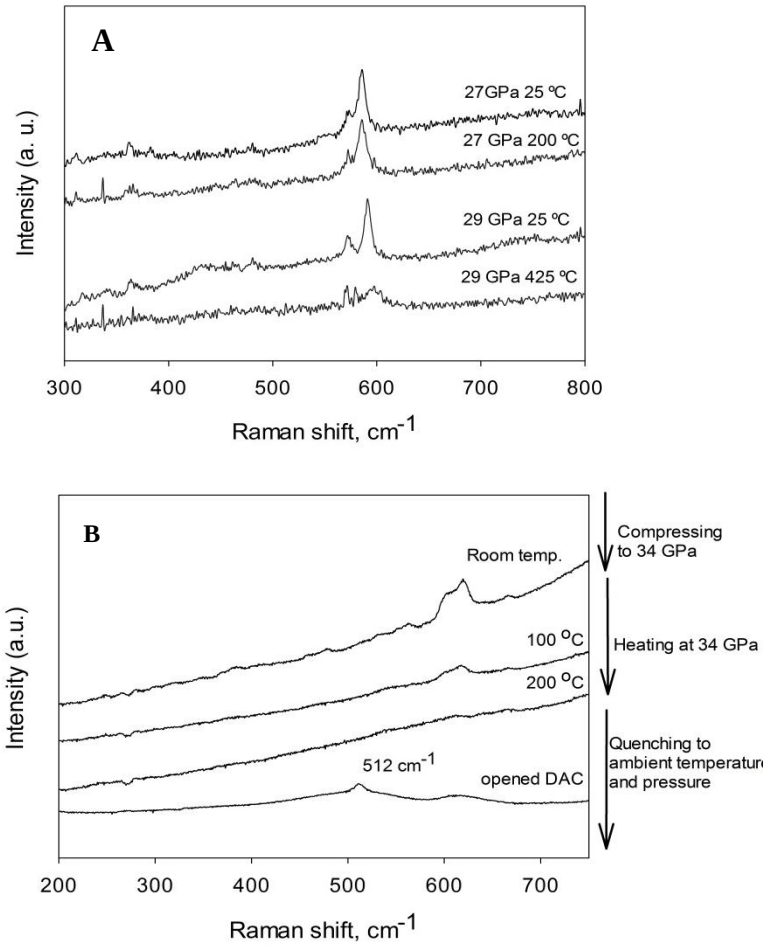

FIGURE 4.7. A) Raman spectra collected at 27-29 GPa during heating up to 400 °C. At both pressures one can notice decrease in intensity and an increase in the splitting of the doublet. **B)** Raman spectra collected at 34 GPa during heating u to 200 ºC and after quenching to ambient conditions. Only a decrease in intensity can be observed at this pressure, witho an increase in the splitting of the doublet.

modes decreases with increasing temperature, and at 27 GPa, as expected, they shift to lower frequency. However, at 29 GPa the higher frequency peak shifted 4 cm^{-1} towards higher frequency between room temperature and 425 °C, whereas the lower frequency band softened of ~1 cm^{-1}, increasing in this way the total spread of the doublet. At this temperature an intermediate peak appears in the spectra but due to the very poor quality of the spectra it is hard to tell if it is a signal from the sample or a spike. At higher temperatures the intensity of the doublet decreased significantly and the doublet peak was not observable.

At 34 GPa and 100 ºC, the peak doublet of coesite-II is still present and decreases both in intensity and in frequency with increasing temperature. No signal was observed at 200 °C (Fig. 4.7b). Raman spectra were collected during decompression at elevated temperature, but no Raman spectra of coesite were observed. At room pressure and after cooling down to room temperature, a broad peak close in position to the main vibration mode of coesite was observed (Fig. 4.7b). The recovered crystal was also analyzed by single-crystal X-ray diffraction (see further).

4.4.4 TEM observations

One of the recovered samples was investigated by transmission electron microscopy. This sample was selected for the TEM analysis because the central, thickest part of the crystal was bridged between diamond anvils at ~35 GPa during compression, whereas the thinner edges of the crystal remained largely undisturbed by the diamond culets. Raman spectra collected on the material recovered from the thin edge of the sample show a weak peak around 425 and 514 cm^{-1}, and the TEM analysis of the same material revealed that very thin grain domains are indexed with coesite in the SAED pattern (Fig. 4.8). On the other hand, the material recovered from the bridged part of the crystal does not show any Raman active modes and appears entirely amorphous at the TEM. Our observations agree

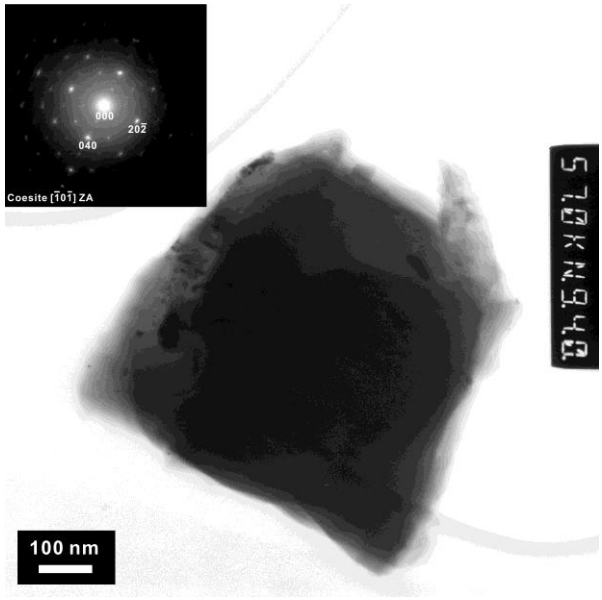

FIGURE 4.8. TEM analysis of one of the grains recovered from the thin edge of the crystal bridged at 35 GPa, showing diffraction profiles that can be attributed to coesite. The material from which this grain was selected shows a weak Raman peak around 520 cm^{-1}.

qualitatively with the previous studies on high-pressure silica behaviour: in experiments with stiff pressure media where amorphization is initiated at lower pressures with respect to experiments in quasi-hydrostatic conditions (e.g., Hemley 1987; Haines et al. 2001).

4.4.5 X-ray diffraction

X-ray mapping along 25 spots of the sample quenched from ~300 ºC and 34 GPa indicates that the material is well-crystallized. All observed diffraction peaks belong to coesite (Fig. 4.9). Phase identification was carried out using the Match! Software v 1.11 (with Crystallography Open Database), considering only the region of *d*-spacing between 4.5 and 1.0 Å (2theta 5 – 19º). The suggested possible phases by the program are coesite, diamond and quartz, however all of the peaks assigned to quartz have d-spacing which can also be assigned to coesite, and no peak belonging solely to quartz has been observed (Fig. 4.9).

4.5 Discussion

Coesite appears to undergo at least two distinct transitions to metastable phases upon compression, as shown in DAC experiments with quasi-hydrostatic medium (Ne) up to ~51 GPa. A similar high-pressure behaviour, i.e., complex path of transformations to metastable phases before amorphization, have been reported for quartz (Haines et al., 2001; Kingma et al., 1993) and it is in agreement with predictions from numerical models, which suggest that a number of metastable phases can appear on compression of SiO_2 materials before amorphization (Dubrovinsky et al., 2004; Wentzcovitch et al., 1998). Most certainly these phases appear as a consequence of the lack of energy at room temperature

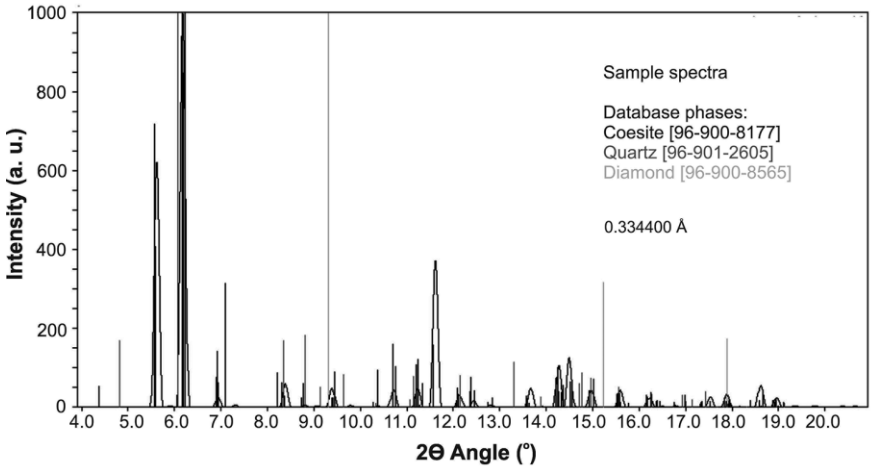

FIGURE 4.9. Representative X-ray diffraction data showing that the crystalline phase quenched from ~34 GPa and ~300 ºC is coesite. Reference phases are taken from Crystallography Open Database: coesite - Araki and Zoltai (1969), synthehic sample at ambient conditions; quartz - Hazen et al. (1989), synthetic sample at pressure of 1bar; and diamond – Wyckoff (1963).

to overcome the considerable potential barrier needed to increase the silicon coordination by oxygen from 4 to 6.

The transition from coesite-I to coesite-II at around 23 GPa was initially reported by Hemley (1987). The study focused on the phase transition, showing its relation to phonon softening, but did not go further into clarifying the eventual splitting of the most intense Raman doublet above ~23 GPa. The author also reports one single broad peak above 30 GPa centered around 600 cm^{-1}, interpreted as a feature similar to that reported for silica glass, and therefore concludes that above such pressure coesite becomes amorphous. Hemley (1987) also reported that the splitting at 23 GPa was obscured in all experiments except in those with argon, which was providing the best quasi-hydrostatic conditions in their experiments at higher pressures. Neon is shown to be a softer pressure-transmitting medium and to give quasi-hydrostatic conditions at higher pressures than argon (Klotz et al. 2009). In our experiments, therefore, we are able not only to clearly follow the evolution of the splitting of the main Raman mode above 23 GPa, but also to observe another phase transition at ~35 GPa. Non-hydrostatic compression, as we observed on the example of partially bridged coesite crystal as well as reported in the experiments with Ar or stiffer pressure media (Hemley 1987), leads to amorphization of coesite at lower pressures at room temperature.

Our experimental and theoretical results are in very good agreement, with a discrepancy in frequencies of about 10 cm^{-1} between the calculated and the measured spectra. The main Raman mode is at 519 cm^{-1} in the experimental spectra and at 510 cm^{-1} in the calculated; another intense A_g mode which is observed at 426 cm^{-1} is calculated at 415 cm^{-1}. Moreover, the calculated frequency shifts with pressure are very similar to those observed experimentally, at least for the strongest Raman modes.

At 8 GPa, a small shoulder at 228 cm^{-1} (Fig. 4.2a) can be observed overlying the 220 cm^{-1} peak (202 cm^{-1} at ambient pressure). From a previous study (Hemley 1987) it appears that the mode at 176 cm^{-1} intersects the 202 cm^{-1} mode at ~8 GPa, and therefore it could be the cause of the shoulder in the spectra we recorded at this pressure. However, it should be noted that the results of our ab initio calculations are in contrast with such an interpretation since these two calculated modes do not cross at any pressure (calculated up to 40 GPa), although their separation decreases with increasing pressure.

In light of our experiments and *ab initio* calculation we can give an insight on the mechanism of transformation from the coesite-I to coesite-II phase in terms of a complex phonon softening. The crystal structure of coesite-II has a lower symmetry than coesite-I, as it appears from the increasing

number of the vibrational modes observed in this study. The calculations show that three phonon modes, one B_g, one A_u and one B_u soften under compression (Fig. 4.4b), the former two becoming imaginary around 27 GPa. They all correspond to some form of shear of the SiO_4 tertrahedra rings, but the A_u and B_u modes are only infrared active. Freezing of any or all of these modes could enhance a displacive transition and may be associated with a breaking of the symmetry of the four-membered rings. This can also give rise to two slightly different breathing modes for two differently sheared rings, a consequence of which is the splitting of the main A_g mode (at 510 cm^{-1} at room pressure) associated with the breathing of the four-membered rings.

An alternative explanation is that the second Raman peak at 560 cm^{-1} in the coesite-II structure arises from the coupling between the soft B_g mode, situated at 77 cm^{-1} at ambient conditions and imaginary at the transition, with either the B_g mode at 430 cm^{-1} (at ambient conditions, 450 cm^{-1} at 20 GPa) or the A_g mode at 455 cm^{-1} (at ambient conditions, 468 cm^{-1} at 20 GPa). In particular the coupling and further energy transfer between the two B_g modes is very likely due to their identical symmetry. This transfer can also enhance the Raman intensity of the higher-energy mode. Coupling of the unstable B_g and the stable A_g modes is possible because of similarities between their eigendisplacements. The coupling could also enhance the polarizability of the higher-energy mode and hence its Raman signature.

The transition from coesite-I to coesite-II is likely to be second order in character because of the phonon softening, continuous behaviour of the main Raman peak, and because of the absence of hysteresis. Decrease in intensity and softening of the main peak doublet during heating, support the observation that coesite-II is a metastable phase, which exists only at room temperatures far outside the pressure stability field of coesite. The heating which is insufficient to transform coesite to the thermodynamically stable phase – stishovite – enhances the thermal motion of the metastable structure and causes instability but, most probably, does not lead to amorphization. Hence, the pressure- and temperature-quenched sample retransforms to coesite. The anomalous spreading of the doublet and shifting to the higher frequency at 29 GPa and 400 ºC requires further understanding and structural analysis of coesite-II.

The transition of coesite-II to coesite-III is possibly first order in character, as it appears from the abrupt change in Raman spectra above ~35 GPa (Fig. 4.2b). As expected in a first order transition, the frequency of the main mode, situated at ~600 cm^{-1}, does not vary significantly with pressure (Fig. 4.4) and a hysteresis is probably hindering reversible transformation from coesite-III to coesite-II.

The mechanisms of this transition cannot be revealed from *ab initio* calculation, since the structure of the two polymorphs is still unknown. If we assume that the major peak observed in the Raman spectra is still correlated to the O-Si-O motions as the A_g mode, the major decrease in frequency may suggest a softer Si-O bond and, hence an increase in coordination number of the Si. Coesite-III would therefore have at least some of Si in octahedral coordination. However, to confirm such hypothesis, a structural study is required.

4.6 Implications

The study of the high-pressure behaviour of coesite reveals two high-pressure polymorphs that remain crystalline far above the previously reported amorphization pressure. This significant discrepancy between previous and our current results implies that the metastable phase diagram of silica phases requires a substantial revision. Crystalline or amorphous metastable phases derived from coesite under high-pressure conditions can be of interest in geological application as potential tracers of peak transient pressure conditions reached in processes such as impacts or faulting.

4.7 Acknowledgements

We very much appreciate the assistance of Stefan Übelhack, who manufactured the insulation box for our experiments. Hubert Schulze is gratefully acknowledged for the sample preparation and Sven Linhardt for his help in experiments with electrical heating. We are grateful to Andreas Audétat for providing the starting glass material and helping us analyze it using LA-ICP-MS. This work was funded as a part of Bavarian Elite Network (ENB) Graduate Program "Oxides". The first-princiepls calcualtions were done on the jade machine of CINES, under DARI grant x2013106368. Portions of this research were carried out at the light source PETRA III at DESY, a member of the Helmholtz Association (HGF). We acknowledge the support of GeoSoilEnviroCARS (Sector 13), which is supported by the National Science Foundation - Earth Sciences (EAR-1128799), and the Department of Energy, Geosciences (DE-FG02-94ER14466).

5. HIGH-PRESSURE CRYSTAL CHEMISTRY OF COESITE-I AND ITS TRANSITION TO COESITE-II

Ana Černok[1], Elena Bykova[1], Tiziana Boffa Ballaran[1], Hanns-Peter Liermann[2], Michael Hanfland[3], and Leonid Dubrovinsky[1]

[1]Bayerisches Geoinstitut, Universität Bayreuth, Universitätsstrasse 30, D-95440 Bayreuth, Germany
[2]Photon Sciences, Deutsches Elektronen-Synchrotron (DESY), Notkestraße 85, 22607 Hamburg, Germany
[3]European Synchrotron Radiation Facility (ESRF), 6 Rue Jules Horowitz, 38000 Grenoble, France

Zeitschrift für Kristallographie - Crystalline Materials 229, 761-773 (2014).

DOI:10.1515/zkri-2014-1763

5.1 Abstract

The high-pressure crystal chemistry of coesite was studied by means of single crystal X-ray diffraction in the pressure interval ~2-34 GPa and at ambient temperature. We compressed the samples using diamond-anvil cells loaded with neon as pressure-transmitting medium and collected X-ray diffraction data using synchrotron radiation. The thermodynamically stable coesite – coesite-I – was observed up to ~20 GPa, with the following unit-cell parameters: a=6.6533(12) Å, b=11.9018(10) Å, c=6.9336(10) Å, β=121.250(20)º and V=469.38(15) Å^3. The volume-pressure data of coesite-I are described by means of a third-order Birch-Murnhagan EoS with parameters V_0 = 547.26(66) Å^3, K_{T0}= 96(4) GPa, K'_{T0} = 4.1(4). Above such pressure we witness the formation of a well crystallized coesite-II, previously observed only by spectroscopic studies. The structure of the novel *high-P* polymorph was determined and refined at ~28 and ~31 GPa with final R indices of 8% and 12 %, respectively. Coesite-II has $P\,2_1/n$ symmetry and a unit cell that is "doubled" along the b-axis with respect to that of the initial coesite-I: a=6.5591(10) Å, b=23.2276(14) Å, c=6.7953(9) Å, β=121.062(19)º and V=886.84(19) Å^3 at ~28 GPa. All Si atoms are in tetrahedral coordination. The displacive phase transition I->II is likely driven by the extreme shortening (0.05 Å or 3.2%) of the

shortest and the most compressible Si1-O1 bond, related to the stiff 180º Si1-O1-Si1 angle. Under compression the linear angle bends, resulting in two independent angles, one of which, however, retains almost linear geometry (~178º). The requirement of this angle to be close to linear likely causes further Si-O compression down to an extremely short distance of ~1.52 Å which prompts subsequent structural changes, with the formation of a triclinic phase at ~31 GPa, coesite-III.

5.2 Introduction

Coesite is the densest polymorph of silica, SiO_2, that contains silicon atom tetrahedrally coordinated to oxygen. It is thermodynamically stable above ~ 2.5 GPa and at temperatures in excess of 500 °C. The polymorph was first synthesized by Coes in 1953 and the structure was determined by Buerger and Zoltai in 1959. Coesite was discovered in nature by Chao and coworkers in impact breccia from Meteor Crater (Chao et al. 1960). Since then, natural occurrences of coesite were documented in kimberlites (Smyth and Hutton 1977), high-pressure metamorphic rocks (Chopin, 1984), and various materials, including meteorites, that have been subjected to shock-metamorphism.

Coesite (*C 2/c*, Z=16) shows nearly hexagonal symmetry at room pressure, with almost equal *a* and *c* axes, and a β angle close to 120º. The asymmetric unit contains two distinct silicon and five distinct oxygen atoms. It is a framework silicate comprised of fully polymerized corner-sharing SiO_4 tetrahedra. Building blocks of the framework are four-membered rings (4-rings) of tetrahedra that form chains that run parallel to the *c*-axis. These chains of 4-rings are linked in such manner that crankshaft-like chains are formed. Due to this arrangement there are five distinct Si-O-Si angles in the structure. The high-pressure structural behaviour of coesite was previously studied using in-house based single crystal X-ray diffraction up to 5.2 GPa (Levien and Prewitt, 1981) and up to 8.7 GPa (Angel et al. 2003) in ethanol-methanol pressure medium, as well as by means of *ab initio* calculations up to 17 GPa (Gibbs et al., 2000). These studies concluded that the symmetry of the unit cell appears less hexagonal with increasing pressure, compressing in the *a* direction more than twice as much than in the *c* direction. Also, the most obvious structural change upon compression was found to be the reduction of four out of five different Si-O-Si angles, with smaller angles undergoing more compression than the larger ones. The Si1-O1-Si1 angle is constrained to 180º due to symmetry requirements. The O1 atom is placed on an inversion center and as long as the symmetry is maintained, the Si1-O1-Si1 linkage remains linear, giving rise to the high stiffness of the structure (e.g. Thompson and Downs, 2010).

Our recent study (Černok et al., 2014) has shown that coesite, similarly to quartz and cristobalite, can be compressed under (quasi)-hydrostatic conditions to very high pressures and at ambient temperatures without undergoing amorphization. Earlier spectroscopic studies observed structural changes in coesite near ~23 GPa (Hemley,1987), and one more near ~34 GPa, with the latter polymorph remaining crystalline at least up to ~51 GPa (Černok et al. 2014). Reconstructive transitions to the stable high-pressure polymorphs consisting of SiO_6 octahedra (e.g. stishovite, $CaCl_2$-structured silica, or seifertite) are often hindered due to high kinetic barriers associated with the relatively strong Si-O bonding within the tetrahedra (e.g. Haines et al. 2001). As a consequence, compression of phases with tetrahedrally coordinated silicon without sufficient heating results in formation of complex metastable phases, leading in particular to persistence of SiO_4–based phases far out of their stability fields. Experimental challenge in studying the structure and the formation of these phases arises from the sluggish transitions, enhanced metastability regions, and formation of poorly crystallized materials. Such conditions usually give rise to weak X-ray diffraction patterns that are difficult to interpret, often resulting in contradictory interpretations. Although spectroscopic studies have indicated phase transitions to coesite-II and III, crystallographic analyses of these phases have not yet been reported.

In this work we were motivated to understand in detail the high-pressure crystal chemistry of thermodynamically stable coesite (hereafter coesite-I) and the mechanisms that lead to its structural transformation induced by pressures exceeding 20 GPa. We report single-crystal X-ray diffraction data collected with diamond-anvil cells (DACs) at ten different pressures up to ~34 GPa using synchrotron radiation. Our data confirm the phase transition above ~20 GPa and give insight into the structure of the novel high-pressure polymorph coesite-II. Appearance of extra reflections above ~30 GPa suggests a subsequent transition to a phase with lower, possibly triclinic, symmetry - coesite-III - in agreement with our previous Raman spectroscopy data.

5.3 Experimental

Synthesis conditions and the starting material used to synthesize the coesite crystals for this study have been described in a previous study (Černok et al. 2014). We selected coesite single crystals of typical size 10 x 20 x 30 μm^3 at the Bayerisches Geoinstitut (BGI), using a rotating anode high-brilliance Rigaku diffractometer with Mo Kα radiation, equipped with an Osmic focusing X-ray optics and a Bruker Apex CCD detector.

The structural behaviour of coesite-I was investigated in the pressure region between 2.4 and ~34 GPa at ambient temperature using piston-cylinder BX90 type diamond anvil cells (DAC) produced at BGI (Kantor et al. 2012). We used Boehler-Almax diamond anvils with 250 μm culet size and apertures of 80° (Boehler and De Hantsetters, 2004), to allow for large reciprocal space coverage in the single crystal X-ray diffraction experiments. Crystals of coesite were loaded together with a ~5 μm in diameter ruby sphere into a cylindrical pressure chamber of 30-40 μm height and ~125 μm diameter drilled in a pre-indented rhenium gasket. Neon, used as pressure transmitting medium, was loaded into the DAC using the BGI gas loading system (Kurnosov et al. 2008).

High-pressure single crystal X-ray diffraction experiments were performed at the beamline ID09A, at ESRF (Grenoble, France) and at the Extreme Conditions Beamline (ECB, P02.2) at PETRA III in Hamburg. At each pressure point, wide-scan diffraction images were collected in the ω range of ± 40 º for 3 seconds. In addition, 80 independent step-scan diffraction frames were collected with time exposure of 1 sec/step in the same ω range. At ESRF, data were collected at seven different pressure points from 2.42(5) up to 20.30(15) GPa, using 30 μm X-ray beam with a wavelength of 0.4144 Å and a Mar555 flat panel detector, located at the distance of 309.5 mm from the sample. At PETRA III we performed an experiment on another crystal, obtaining single crystal data at 27.52(13), 30.94(41) and 34.20(28) GPa, using 2 x 4 μm^2 (FWHM) X-ray beam with a wavelength of 0.29004 Å. The detector used was a MAR345 online Image Plate (IP), located at the distance of 400.8 mm. Pressure was determined using the ruby pressure gauge (Mao et al. 1986) both before and after collection of X-ray data. At ECB at PETRA III, in addition to the ruby pressure scale, we determine pressure also by using neon EOS reported by Fei et al. (2007). Single-crystal data have been reduced with the CrysAlis software package (Oxford diffraction 2006) and analyzed with the SHELX97 program package (Sheldrick 2008) as implemented in the WingX software (Farrugia 1999). Isotropic structure refinements of coesite-I were performed based on F^2 starting from the atomic coordinates for coesite at ambient conditions, reported by Angel et al. (2003). The structure of coesite-II was solved by direct method using SHELXS and refined by full matrix least-squares in the isotropic approximation using SHELXL, both programs being implemented in SHELX97 software.

5.4 Results

Wide-scan exposure images indicate that the single crystal of coesite remain well-crystallized up to the maximal pressures attained in this study (~34 GPa) with an abrupt change in the diffraction

pattern between ~20 and ~28 GPa (Fig. 5.1). The change is characterized by an increase in the number of reflections and an overall decrease in their intensities. This is in agreement with the Raman spectroscopy observations of a pressure-induced structural transformation from coesite-I to a lower-symmetry phase coesite-II (Hemeley 1987; Černok et al. 2014). We investigated the compressibility and the structural evolution of coesite-I from 2.42(5) GPa up to 20.30(15) GPa. The structure of the novel polymorph coesite-II was solved using the dataset collected at 27.52(13) GPa and also refined at 30.94(41) GPa. The unit cell parameters of the polymorphs at various pressures are reported in Table 5.1 and the compressibility data of coesite-I are summarized in Table 5.2. Details of the refinement procedure are given in Table 5.3. Refined positional parameters of coesite-I and coesite-II are reported in Tables 5.4a and b, respectively. Selected bond lengths and angles are given in Tables 5.5 and 5.6.

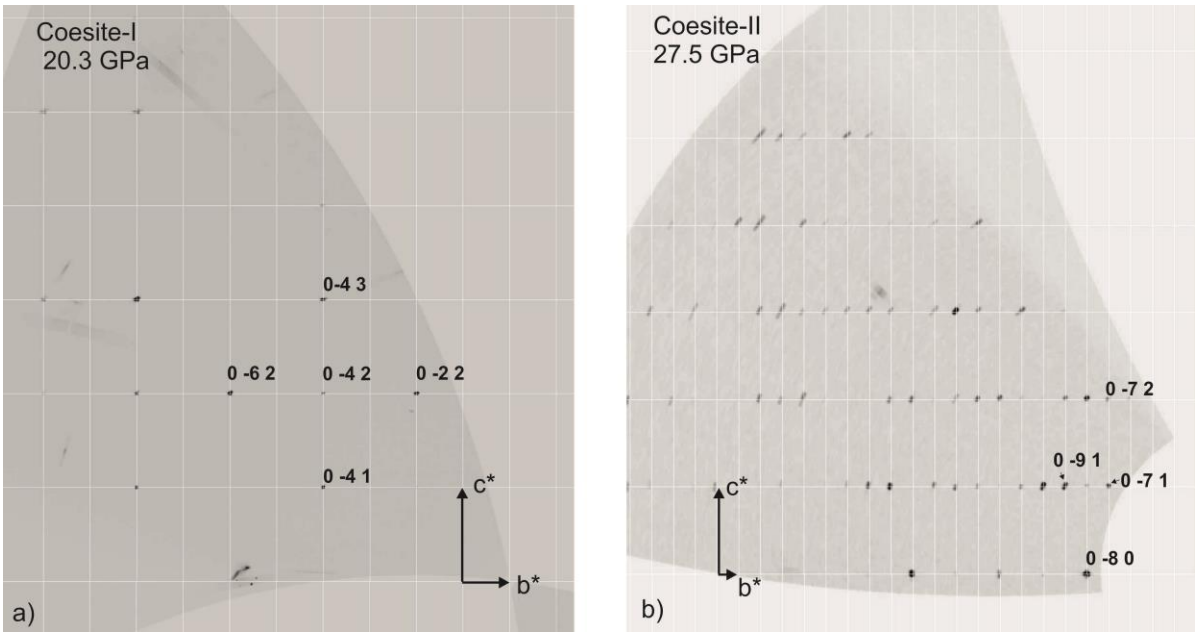

FIGURE 5.1. Reciprocal space reconstruction of the *b***c** plane for a) coesite-I at 20.3 GPa and b) coesite-II at 27.5 GPa. Some reflections are labeled as example. The reciprocal lattice of coesite-II has a larger *c*/*b* ratio than coesite-I, due to the larger unit-cell. The number of reflections collected for coesite-II increased due to the lower symmetry.

5.4.1 Coesite-I

5.4.1.1 Compressibility

The smooth and continuous evolution of the coesite-I unit cell volume with pressure (Fig. 5.2) indicates that it remains stable up to 20.30(15) GPa. By fitting the *P*-*V* data with a third-order Birch-Murnaghan equation of state (BM3-EoS) using the EosFit software v5.2 (Angel, 2000), we obtain a

room pressure unit cell volume, V_0, of 547.26(66) Å^3, which within uncertainties of our measurements coincides with the V_0 values reported in two other experimental high-pressure studies: i.e. 546.46(5) Å^3 by Levien and Prewitt (1981) and 546.80(3) Å^3 by Angel et al. (Angel et al., 2001). The unit cell volume is well within the range of the reported values from various XRD studies at ambient conditions of synthetic, e.g. 549.47 Å^3 ((Araki and Zoltai, 1969)Araki and Zoltai, 1969) or 546.4(1) Å^3 (Gibbs et al. 1977) and natural, e.g. 546.74(30) Å^3 (Smyth et al., 1987) or 546.98(13) Å^3 ((Ikuta et al., 2007), samples. The total decrease of the unit cell volume from room pressure up to 20.30(15) GPa is about 14.2%, with a correspondent density increase of about 16.5 %.

Table 5.1: Unit-cell parameters of coesite-I and II at various pressures

P (GPa)[a]	*a* (Å)	*b* (Å)	*c* (Å)	*β*	*V* (Å^3)	*ρ* (g/cm^3)
Coesite-I (C 2/c)						
0.00010(1)	7.1436(51)[b]	12.3621(57)[b]	7.1752(19)[b]	120.248(76)[b]	547.26(66)[b]	2.92[c]
2.42(5)	7.0612(6)	12.2936(5)	7.1417(4)	120.520(9)	534.10(20)	2.99
5.16(6)	6.9837(6)	12.2255(5)	7.1081(4)	120.736(9)	521.60(20)	3.06
9.24(9)	6.8746(6)	12.1220(5)	7.0549(4)	120.965(10)	504.10(20)	3.17
12.14(9)	6.8070(7)	12.0623(5)	7.0223(4)	121.057(11)	493.94(18)	3.23
14.90(25)	6.7549(11)	12.0019(9)	6.9863(7)	121.075(18)	485.11(16)	3.29
17.80(5)	6.6921(11)	11.9470(9)	6.9581(7)	121.179(19)	475.95(15)	3.35
20.30(15)	6.6533(12)	11.9018(10)	6.9336(10)	121.250(20)	469.38(15)	3.40
Coesite-II ($P2_1/n$)						
27.52(13)	6.5591(10)	23.2276(14)	6.7953(9)	121.062(19)	886.84(19)	3.60
30.94(41)	6.5446(15)	23.0389(17)	6.7325(13)	121.37(3)	866.7(3)	3.68

Note: [a]Average values of pressures, measured before and after X-ray data collection; [b]Values obtained by fitting BM3 EoS to the *P-V* dataset with EOSfit; [c]Literature value (Angel et al. 2003); Numbers in parentheses are the esd's in the last decimal place of each value.

Table 5.2: Parameters of the 3rd order Birch-Murnhagan EoS fit to coesite-I data

Volume compressibility	V_0 (Å^3)	K_0 (GPa)	K'	K'' (GPa^{-1})	$\chi^2_{weighted}$
Unit cell volume	547.26(66)	96(4)	4.11(38)	[-0.042]	0.7355
SiO_4 tetrahedra					
Si1	2.1465(71)	283(23)	[4]	[-0.014]	1.2560
Si2	2.1428(40)	445(31)	[4]	[-0.008]	0.9840
Axial compressibility	L_0 (Å)	K_0 (GPa)	K'	K'' (GPa^{-1})	$\chi^2_{weighted}$
X1∥*a**	6.1710(51)	52(2)	3.7(3)	[-0.070]	1.2676
X2∥b	12.3621(57)	143(8)	3.6(8)	[-0.026]	4.1513
X3∥c	7.1751(19)	173(7)	2.5(6)	[-0.026]	1.9640

Note: Data used for BM3 EoS are reported in Table 1. Numbers in square brackets are implied values. X1 compressional direction is parallel to $a^* = a \sin\beta$. Numbers in parentheses are the esd's in the last decimal place of each value.

Although Angel et al. (2001) suggested that a 4th-order BM-EoS is necessary to describe adequately the high-pressure behaviour of coesite, the normalized stress, F_E, vs. Eulerian strain, f_E, plot (Angel 2000) constructed from our *P-V* data shows a linear trend consistent with a 3rd-order BM-EoS (Fig. 5.3). The intersection of the linear fit through the F_E data points with the F_E-axis suggests a value of the bulk modulus,K_{T0}, of about 95 GPa and the slope of such linear fits yields its pressure derivative K'_{T0} of 4.3. Such results are in good agreement with the BM3-EoS parameters obtained by fitting our

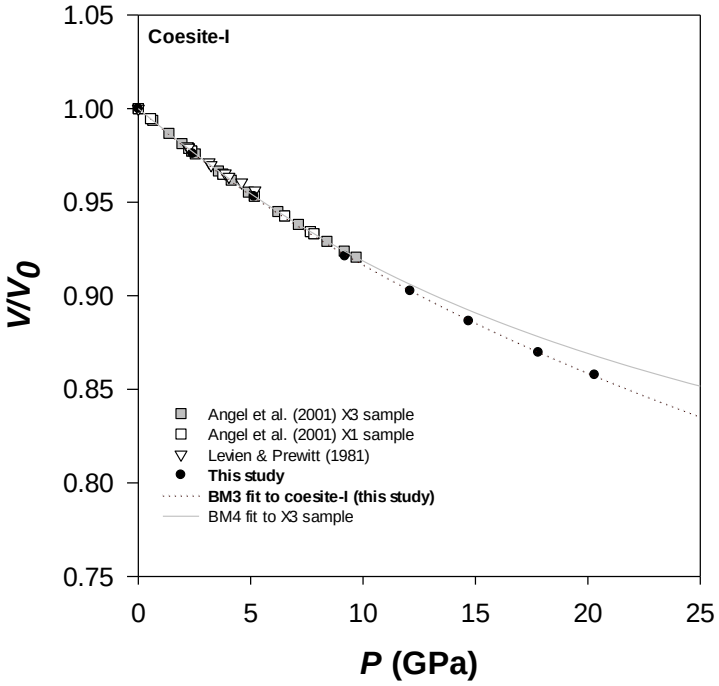

FIGURE 5.2. Unit-cell volumes, normalized with respect to the V_0 BM3 parameter, plotted against pressure. Literature data are reported for comparison. The dashed line is a 3rd order Birch-Murnaghan EoS (BM3) fitted to the coesite-I *P-V* data from this study. The grey line is the 4th order BM EoS reported by Angel et al. (2001) for the sample X3 *P-V* data.

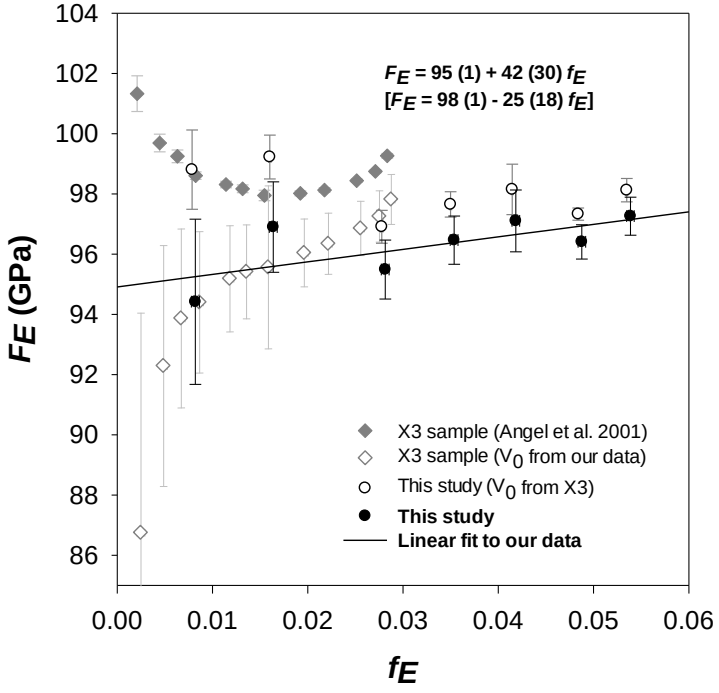

FIGURE 5.3. Pressure-volume data of coesite-I collected up to 20.3 GPa, plotted as normalized pressure, F_E, against Eulerian strain, f_E. Our data (circles) are compared with those of the X3 sample (diamonds) from Angel et al. (2001): both data sets are plotted using their original V_0 (full symbols), as well as by substituting the values of V_0 (see text). The uncertainties in F_E and f_E were calculated by propagation of the experimental uncertainties in volume and pressure, according to Heinz and Jeanloz (1984). The reported relationships are the linear fit through our data with the BM3 EoS V_0 (top) and with the V_0 from X3 sample (bottom). The two bulk moduli so obtained differ only slightly.

P-V data, which are the following: V_0 = 547.26 (66) Å^3, K_{T0} = 96(4) GPa, K'_{T0} = 4.1(4). The value of the bulk modulus is very close to that reported by Levien and Prewitt (1981): K_{T0} = 96(3) GPa, which was obtained using a BM3 fit to their data collected up to 5.1 GPa. However, their pressure derivative is significantly larger (K'_{T0} = 8 (2)). Our data are in excellent agreement with the BM3-EoS parameters obtained from the fit to the data collected up to ~9 GPa by Angel et al. (2001): i.e. K_{T0} = 97.4(6) GPa and K'_{T0} = 4.3(2). The F_E-f_E plot calculated for the *P–V* data of Angel et al. (2001) is also shown in Figure 3, for comparison. Our data are significantly more scattered than those from Angel et al. (2001), but clearly do not show the curvature of the data presented by Angel et al (2001). Since the values of V_0 can have a strong effect on the F_E-f_E plot (Angel and Jackson, 2002) we have considered two further F_E-f_E plots: one using our volume data with V_0 from the X3 sample of Angel et al. (2001), and one using the data from Angel et al. (2001) with the V_0 values from this study (Fig. 5.3). The different V_0 does not significantly affect the linear trend of our data and gives EoS parameters which are indistinguishable within the uncertainties. On the contrary, the F_E-f_E data of Angel et al. (2001) are clearly more dependent on the choice of V_0 and the slight increase in V_0 of 0.4 Å^3 results in a F_E-f_E plot which is more similar to that of our data (Fig. 5.3).

The evolution of the unit-cell axes under pressure is in good agreement with previous studies, as illustrated by comparison to the X3 data set of Angel et al. (2001) and it implies that the axial compression of coesite-I is very anisotropic (Fig. 5.4). Due to the monoclinic symmetry, one of the principal axis of compression is constrained to lie along the *b*-axis, and the other two principal axes must lie in the (010) plane. Previous analyses of the strain ellipsoid (Angel et al. 2001) showed that in the case of coesite, the principal axes of compression lie within uncertainties parallel to the $a^*=a\sin\beta$, *b* and the *c* axes, with the a^* being the most compressible and the *b* and *c* axes showing similar compressional rates. We confirm this compressional regime (Fig. 5.4) and find that the axes of the strain ellipsoid rotate only ~2° up to 20.3 GPa, i.e. less than the uncertainty on their position.

The axial F_E-f_E plots are compared to the values from Angel et al. (2001) in a way similar to the unit cell volume (Fig. 5.5). The linear trend of our data is less affected by the variation of zero-pressure values, particularly in the case of the least compressible *b*-axis. The axial F_E-f_E plots constructed for the X3 dataset using our zero-pressure values indicate linearity that corresponds closer to our data. Following Angel (2000), estimates of the zero-pressure lattice constants as well as the linear moduli along the crystallographic axes have been obtained by fitting the cubes of the unit-cell parameters

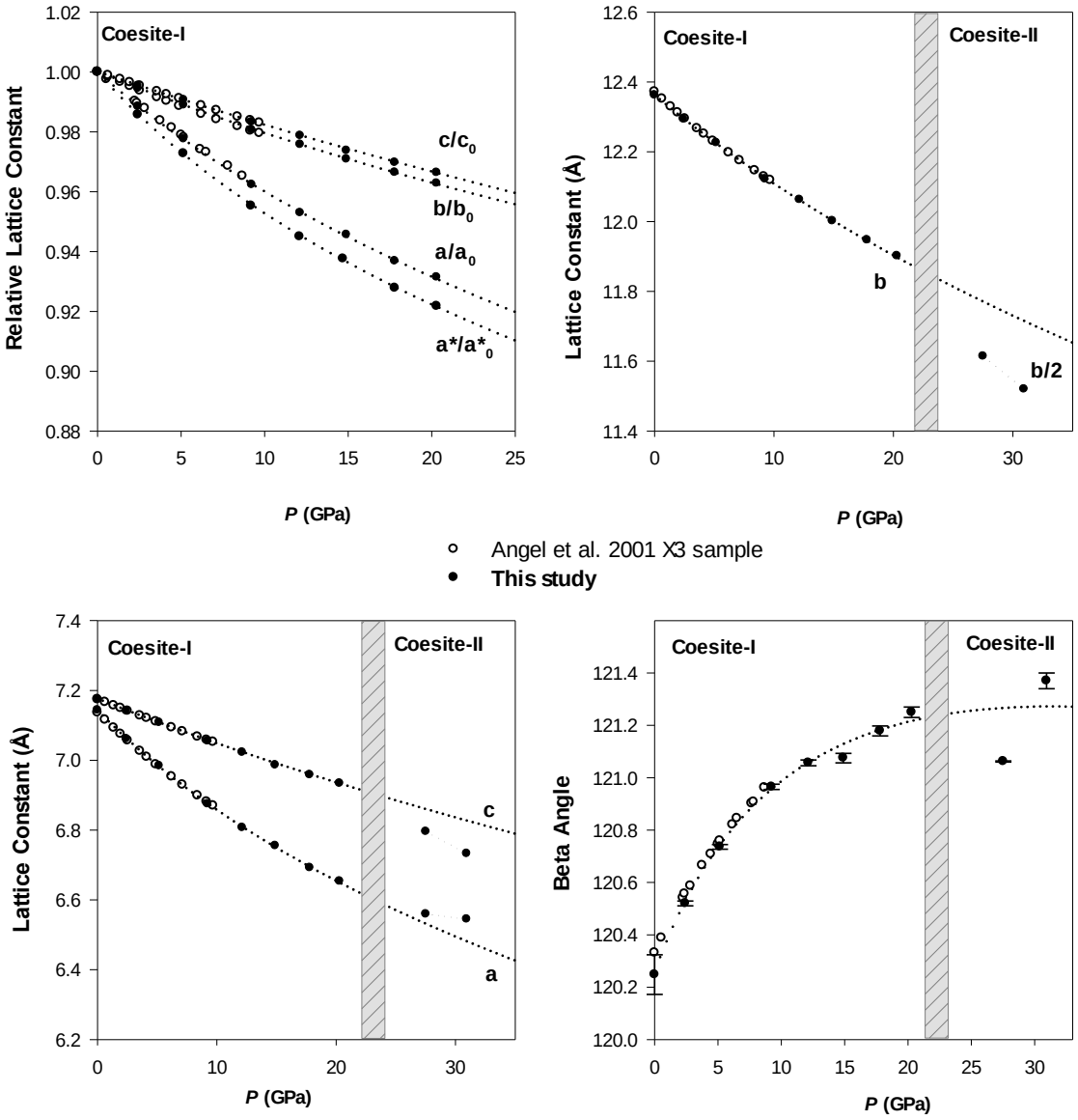

FIGURE 5.4. Compressibility of the unit-cell parameters of coesite-I and II. Half-values of the *b*-constant for coesite-II is reported. Literature values are given for comparison. In addition to the relative unit cell constants, we also plot $a^*=a \sin\beta$, which is the most compressible direction in coesite. Dotted lines are BM3 fits through our experimental data. BM3 fit of the β-angle was obtained from the BM3 fit to the a^* values.

with a 3rd-order Birch-Murnagham EoS. The resulting linear EoS parameters are the following: a_0=7.1436(51) Å, $K_0(a)$=67(3) GPa, K'=3.3(3); b_0=12.3621(57) Å, $K_0(b)$=143(8) GPa K'=3.6(9); c_0=7.1752(19)Å, $K_0(c)$=173(7) GPa, K'=2.5(6) and a^*_0.=6.1710(56), $K_0(a^*)$=52(2) GPa, K'=3.7(3). The linear moduli and their respective pressure derivatives obtained from the BM3 fits are in good agreement with the values determined from the axial F_E-f_E plots.

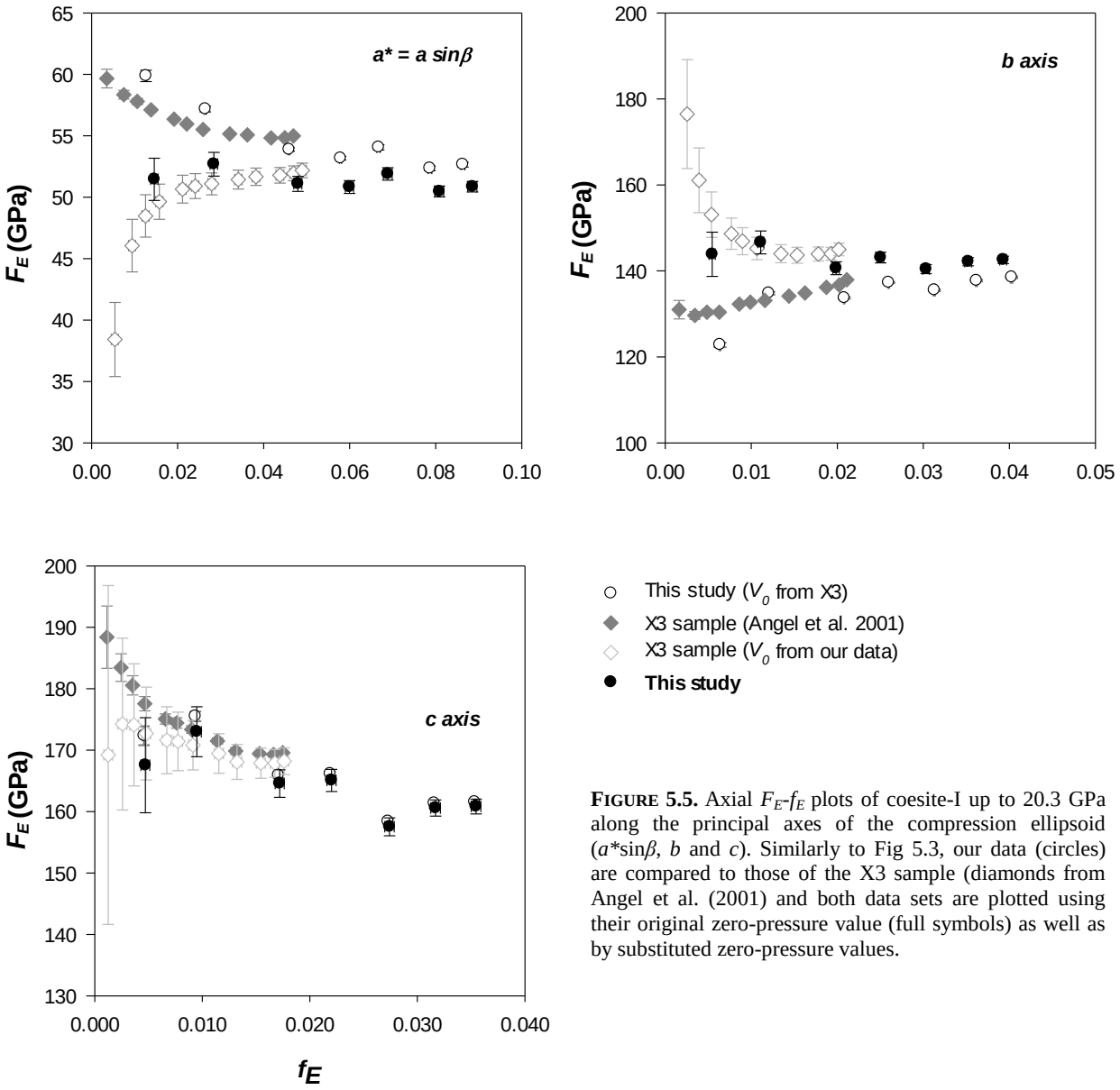

FIGURE 5.5. Axial F_E-f_E plots of coesite-I up to 20.3 GPa along the principal axes of the compression ellipsoid ($a^*\sin\beta$, b and c). Similarly to Fig 5.3, our data (circles) are compared to those of the X3 sample (diamonds from Angel et al. (2001) and both data sets are plotted using their original zero-pressure value (full symbols) as well as by substituted zero-pressure values.

5.4.1.2 Mechanisms of compression

The structure of coesite-I shown in Figures 5.6a and b is illustrating the characteristic features and the nomenclature in detail. As in previous studies, we find no evidence of kinking of the linear Si1-O1-Si1 angle throughout the pressure range of the coesite-I stability field. The rate of compression of the four other Si-O-Si angles (Fig. 5.7), with the smaller angles being more compressible, is in good agreement with the experimental studies at lower pressures (Levien and Prewitt, 1981; Angel et al. 2003). The *ab initio* calculations (Gibbs et al. 2000) suggest compressional rates similar to those obtained in all of experiments, although the calculated angles appear to be smaller than those measured. Decrease of the smallest Si1-O5-Si2 angle from 137.44º (ambient, Angel et al. 2003) to 125.54º at ~20 GPa contributes to the shortening along the *b*-axis. Kinking of the Si2-O2-Si2 angle (142.69º ambient to 127.70º at 20 GPa) brings the four-membered rings closer along [001]. However, the internal shape of the 4-rings in coesite-I is controlled by the much faster decrease of the Si1-O3-Si2 angle with respect to the Si1-O4-Si2, which results in shearing of the rings along [001]. An increase of the O3-O3 ring diagonal by ~5% up to the transition pressure contributes to the large stiffness along the *c*-axis, giving rise to its stiffest linear modulus (Table 5.6).

Two neighboring (010) planes of the rings can be seen as two semi-close-packed planes of O3 and O4 oxygen atoms connected by the linear Si1-O1-Si1 angle (Fig. 5.6a). The spacing between these oxygen planes increases with pressure up to 12 GPa, in agreement with the lower pressure studies (Angel et al. 2003) but it levels off above ~12 GPa (Fig. 5.6a). This is probably a consequence of the fact that Si2 tilting has reached a limiting value and Si1 cannot rotate further around the Si1-Si1 axis. Further tilting of Si2 would invoke the Si1 to tilt as well, which is unfeasible due to the symmetry of coesite-I.

5.4.1.3 Tetrahedral distortion

The two symmetrically distinct SiO_4 tetrahedra of the coesite-I structure respond differently to compression up to ~20 GPa, following a trend similar to that observed at lower pressures (Levien and Prewitt, 1981; Angel et al. 2003). The Si1 tetrahedron shows a volume decrease of about 5.4 % and the Si2 of 4.4 % in the investigated pressure range. A larger increase in angular variance and quadratic elongation with pressure shows that the Si1 tetrahedron undergoes much more distortion than the Si2 tetrahedron (Table 5.5).

The compression and distortion of the Si1 tetrahedron are accommodated by highly anisotropic shortening of the Si-O bonds, with the shortest Si1-O1 bond (1.5859(13) Å at 2.42 GPa) undergoing the largest compression (3.2%, Fig. 5.8). Similarly, the shortest O1-O4 distance (2.5841(30) Å at 2.42 GPa) is the most compressible tetrahedron edge of the coesite-I structure, showing a decrease of 4.9% up to 20.3 GPa. This is a consequence of the larger distortion of the O1-Si1-O4 angle with respect to the rest of the tetrahedral (O-Si-O) angles (Table 5.5). In spite of large Si1-O1 bond compressibility and the absence of Si1-O1-Si1 kinking, the Si1-Si1 distance remains the longest cation-cation distance throughout the compression of coesite-I. The Si2 tetrahedron shows less anisotropic

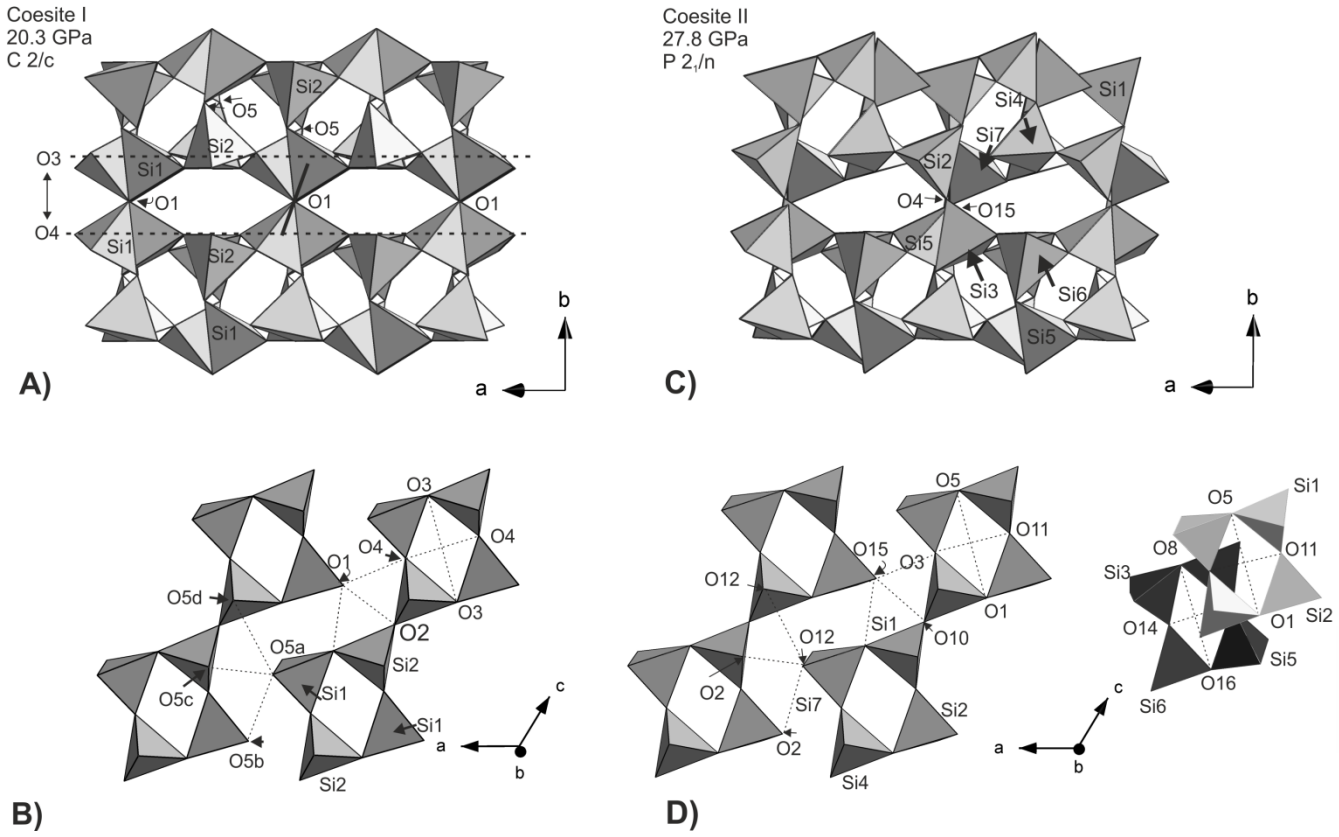

FIGURE 5.6. Structure of coesite-I at 20.3 GPa and of coesite-II at 27.5 GPa viewed in different directions. **A**) Coesite-I seen down the *c*-axis. Dominant features are the symmetric hollow channels that run parallel to [001], placed between the linear Si1-O1-Si1 angles. Dashed lines indicate semi-close-packed O3 and O4 planes of oxygens in (010) and the plot on the right shows the O3 and O4 distance under pressure. **B**) Coesite-I seen along the *b*-axis. Characteristic features are the four-membered rings of corner sharing SiO_4 tetrahedra. Each ring consists of two opposite Si1 and two Si2 tetrahedra connected by O3 and O4 atoms. Neighboring rings are connected by O2 atoms to form chains aligned parallel to the *c*-axis. The chains are not connected with the neighboring chains within the same (010) plane. Instead, they are linked to the chains from a plane above and a plane below alternately by O1 or O5 atoms. Dotted lines indicate various O-O distances (nomenclature after Angel et al. 2003) between unconnected chains within the same (010) plane and within the 4-rings (O3-O3 and O4-O4 diagonals). The values of these distances are reported in Table 5.5. **C**) Coesite-II seen down the c-axis. The hollow channels parallel to the *c*-axis are asymmetric and are places between Si7-O4-Si5 (~178º) and Si2-O15-Si3 (~153º) angels. Few distinct Si tetrahedra are labeled. **D**) Planes of 4-rings in coesite-II seen along the *b*-axis. Each ring consists of four distinct Si tetrahedra. Dotted lines indicate similar O-O distances as in coesite-I, with oxygen nomenclature of coesite-II. Small sketch on the right illustrates two different sizes of 4-rings in coesite-II.

compressional behaviour, with smaller changes in Si-O and O-O distances with pressure (Fig. 5.8), as well as smaller changes of O-Si2-O angles (Table 5.5). In contrast to Si1 and according to the expected behaviour with pressure, the shortest Si2-O3 bond is the stiffest bond of the Si2 tetrahedron and of the entire structure (0.1% compression).

The major difference in compressibility of the two tetrahedral sites is clearly reflected in their respective bulk moduli, calculated for the tetrahedral volume changes: 283(23) GPa for $Si1O_4$ and 445(31) GPa for $Si2O_4$. The Si1 tetrahedral site is anomalously compressible relative to SiO_4 tetrahedra in other silicates. To our knowledge, the only other common silicate minerals for which the reported bulk moduli of the tetrahedral Si sites are comparable to that of Si1 tetrahedron in coesite-I are zircon and forsterite (summarized in Smyth et al. 2000). Note, however, that in such structures the tetrahedra do not form three-dimensional framework as in the case of coesite.

5.4.2 Phase transition and the structure of coesite-II

The displacive phase transition from coesite-I to coesite-II is characterized by a change of symmetry from *C* 2/c to *P* 2_1/n (Fig. 5.6a and c). Due to the rearrangement of the atoms, doubling along the *b*-axis is achieved, resulting in the disappearance of the *C*-centering after the transition, in a doubled unit cell volume, and in a number of molecular units Z=32 per unit cell. The asymmetric unit of coesite-II contains eight silicons and sixteen oxygens. The effect of the symmetry reduction can be better understood by observing the changes that occur within the hollow channels that run parallel to the *c*-cell edge (Fig 6a and c). In the coesite-I structure these chains are separated by the linear Si1-O1-Si1 linkages, and they appear symmetric due to a 2-fold axis in [010] perpendicular to a mirror plane in (010). The mirror plane is placed in the middle of the channels, running exactly trough the O1 atoms.

After the phase transition and distortion of the linear S1-O1-S1 angle (Fig. 5.7), the shape of these channels is distorted with consequent disappearance of the mirror plane and loss of the *C* center. Bending of the linear Si1-O1-Si1 angle results in four non-equivalent silicon atoms connected by two non-equivalent oxygens, thus forming two independent angles. These are Si7-O4-Si5 (~178º) and Si2-O15-Si3 (~153º). Very likely, the extreme compression of the shortest Si1-O1 bond drives the bending of the Si1-O1-Si1 angle and the consequent loss of the mirror plane. Above the transition, those Si-O distances within the Si5 and Si7 tetrahedra, which are related to an angle still very close to 180º, compress down to ~1.52 Å at 30.94(41) GPa (Fig. 5.8). In the case of the Si2-O15-Si3, the previously linear angle decreases by nearly 30º and the related Si-O bonds increase to ~1.55 Å.

Upon completion of the phase transition, the planes described by the O3 and O4 oxygens do not appear semi-close-packed as in coesite-I (Fig. 5.6d) and all tetrahedra of coesite-II are subjected to tilting resulting in a steady reduction in Si-O-Si angles down to extreme values, the smallest being ~120º (Fig. 5.7). The kinking enables the structure of the four-membered rings to become "loose" and less coplanar. The non-planar (i.e. outside of 010 plane) distortion of the rings contributes to the compression in all directions and the structure of coesite-II appears much more compressible than that of coesite I. Unlike coesite-I, which consists of only one characteristic 4- ring, there are two distinct rings, i.e. two alternating layers consisting of two different sizes of the 4-rings in the structure of coesite-II (Fig. 5.6d).

Volume reduction of the coesite structure is most efficiently achieved by reducing the distance between the unconnected chains within the (010) plane. This is illustrated by the reduction of the distances between the six closest oxygen atoms (Table 5.6). The rate of this reduction is quite anisotropic. The greatest reduction is achieved along the *a*-axis, i.e. the O5a-O5c distance (O12-O2b in coesite-II) that compresses about ~23% down to ~2.4 Å (at 30.94 GPa). This oxygen-oxygen distance between the chains is shorter than the average tetrahedral O-O edge at this pressure. High reduction is achieved along *c*, as well, by ~14% reduction in O5a-O5b (O12-O2a) distance down to ~2.6 Å at 30.94 GPa.

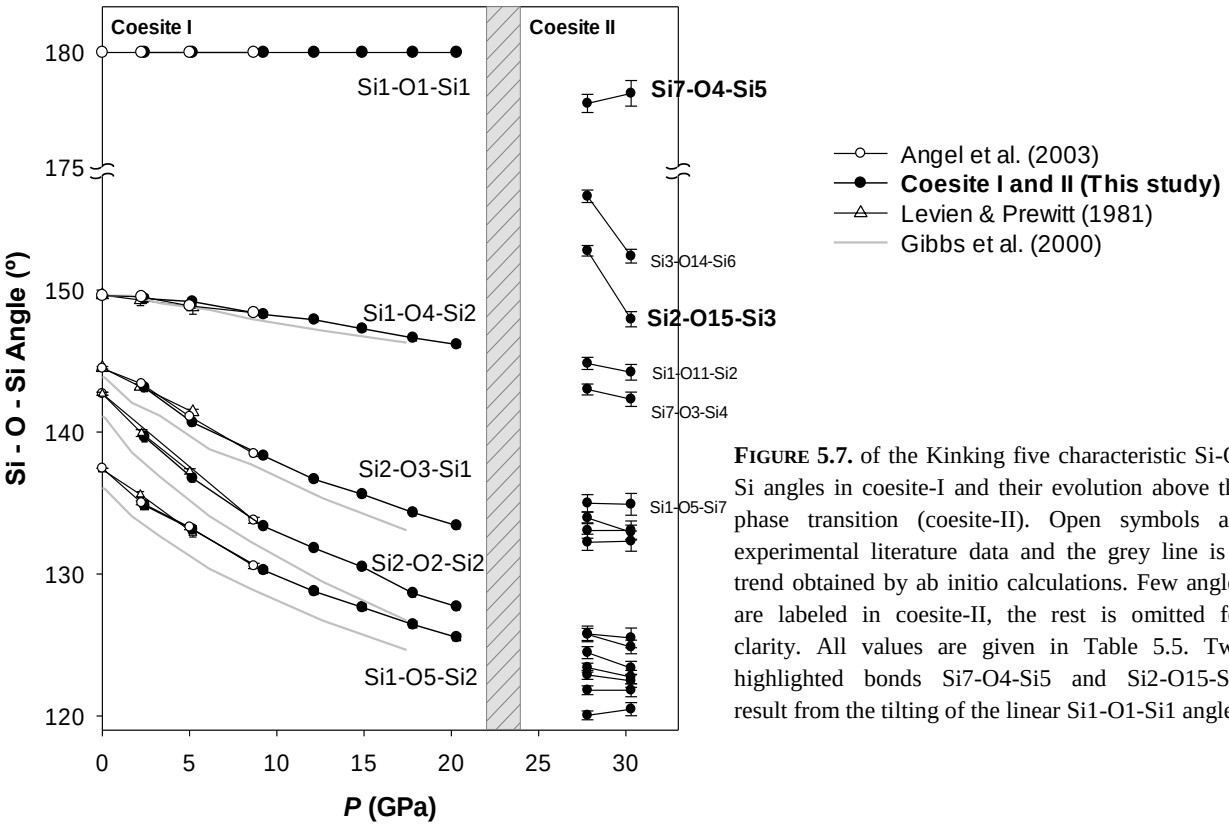

FIGURE 5.7. of the Kinking five characteristic Si-O-Si angles in coesite-I and their evolution above the phase transition (coesite-II). Open symbols are experimental literature data and the grey line is a trend obtained by ab initio calculations. Few angles are labeled in coesite-II, the rest is omitted for clarity. All values are given in Table 5.5. Two highlighted bonds Si7-O4-Si5 and Si2-O15-Si3 result from the tilting of the linear Si1-O1-Si1 angle.

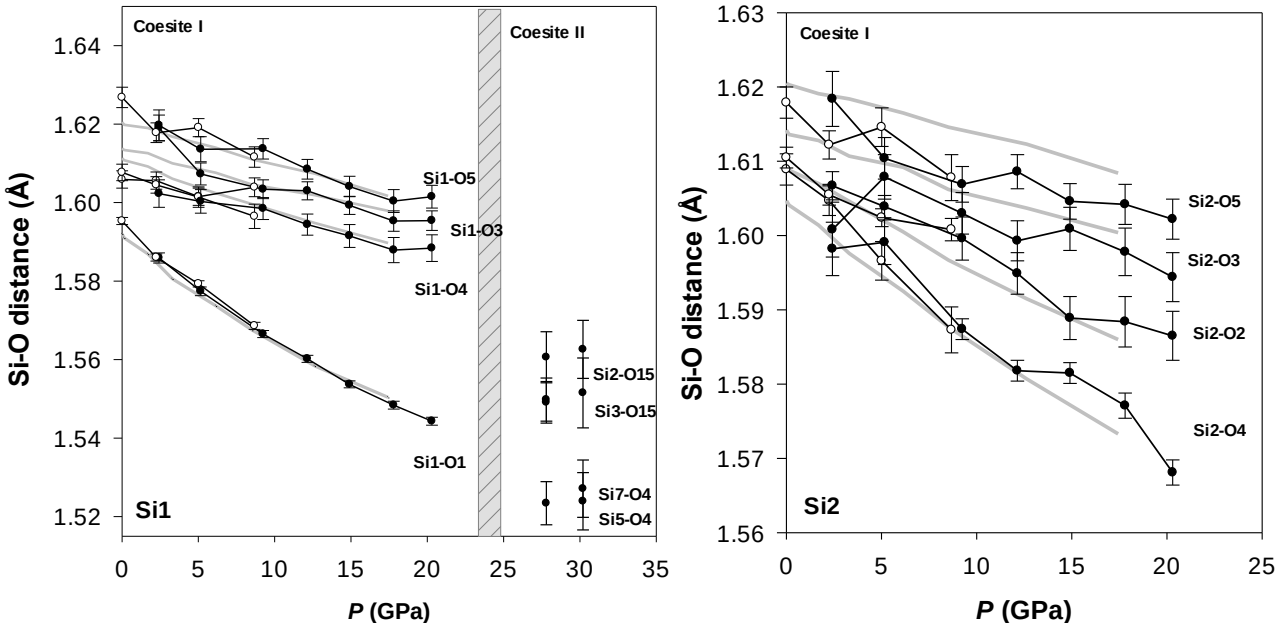

FIGURE 5.8. Si-O bonds for Si1 (left) and Si2 (right) tetrahedra in coesite-I. For the Si1 tetrahedron we also show the evolution of the shortest Si1-O1 bond above the phase transition in coesite-II. The two bonds related to the almost linear Si5-O4-Si7 angle are compressed down to ~1.52 Å at 30.9 GPa.

5.4.3 Further phase transitions

At 30.94(41) GPa we observe reflections that, albeit weak, can be indexed by a triclinic unit cell coexisting with the coesite-II phase. The unit cell parameters of this phase are a=6.788(4) Å, b=7.040(4) Å, c=8.714(5) Å, α=69.47(5)°, β=82.26(5)°, and γ=80.89(5)° at 30.94(41) GPa. At 34.20(28) GPa the intensities of the reflections for this triclinic phase are much stronger. At this highest pressure point we still observe some coesite-II reflections, but their intensities are too weak to allow for proper integration. The appearance of a triclinc phase is consistent with our previous Raman spectroscopy observation (Černok et al., 2014) that indicates a structural change near ~34 GPa to a phase with symmetry lower than that of coesite-II. This additional structural change is probably related to the bending of the remaining stiff Si5-O4-Si7 angle driven by the extremely short Si5-O4 and Si7-O4 bonds, which are highly unlikely to compress any further.

A possible explanation for the presence of two phases at ~31 GPa may reside on the fact that, although the triclinic phase is more stable than coesite-II at such pressure, the complete transition is hindered due to the slow kinetics of the transformation. If this is the case, coesite-II appears above 31 GPa as an "overpressurized" phase out of its (meta)stability field. A similar behaviour was seen in cristobalite I, which compresses smoothly far out of its stability field, suppressing the formation of the more stable high-pressure polymorph cristobalite II (Dera et al. 2011).

5.5 Conclusion

The displacive phase transition from coesite-I to coesite-II above ~20 GPa is driven by extreme shortening of the shortest and most compressible Si1-O1 bond (Fig. 5.8). In order to allow more compression of this individual bond the Si1-O1-Si1 angle, constrained by symmetry to be 180º in coesite-I, starts to bend with consequent breaking of the symmetry from *C*2/*c* to $P2_1/n$ and formation of two different, independent angles. One of the angles remains close to 180º, though, whereas the other one decreases by nearly 30º. The tetrahedra in coesite-II are rearranged in such a way that two slightly different 4-membered rings are created (Fig. 5.6d). Our previous Raman spectroscopy study on the pressure-induced phase transition in coesite reveals that the main A_g vibration mode of coesite at ~521cm^{-1} is a breathing mode of the 4-membered rings. The two rings in coesite-II with two slightly different sizes are expected to have breathing modes at slightly different frequencies, and we indeed observed appearance of a doublet in the experimental Raman spectra upon the coesite-I to coesite-II transition (Chapter 4). The computational spectra of coesite-I under pressure reveal that two modes become most unstable between 20 and 30 GPa: a B_g Raman active mode at 77 cm^{-1} and an A_u infrared active mode at 111 cm^{-1} (see the computed spectra in WURM database for details, http://www.webcitation.org/6NAEOl1G6). The softening of the Raman active mode was previously considered to be related to the structural instability (Hemley 1987). The computational data, however, clearly indicate that the A_u mode involves large atomic displacement of the O1 atom from the linear Si-O-Si angle, while the B_g mode has no impact on it. Therefore, we conclude that the softening of the A_u mode is more likely responsible for the symmetry breakdown and the bending of the Si-O-Si angle.

The very short Si-O bond found in coesite and its high compressibility is a good example of how such bonds are restricted to the (almost) linear Si-O-Si geometry, and appear highly unfavorable in other Si-O-Si arrangements. This experimental evidence conforms well to theoretical predictions. For example, Oberhammer and Boggs (1980) ascribed short Si-O lengths to the highly ionic character of the bond and found that the ionicity of the bond increases as the length of the bond decreases. A later calculation by Nicholas et al (1992) contributed to this conclusion, by finding that the ionicity of the bond increases by ~25% if the Si-O-Si angle widens from 130º to 180° and the Si-O shortens. In general, the force field that governs the Si-O bond length and the related Si-O-Si angle, as well as their respective stretching and bending, can be seen as independent from the long-range forces of an entire crystal (Gibbs et al. 1994). Therefore, the sequence of the phase transitions and symmetry breakdowns in coesite under pressure is most likely controlled by highly compressible S1 tetrahedron and, in particular, by its most compressible Si1-O1 bond.

5.6 Acknowledgements

This work was partially funded by Bavarian Elite Network (ENB) Graduate Program *Oxides*. Portions of this research were carried out at the light source PETRA III at DESY, a member of the Helmholtz Association (HGF). The samples were partially analyzed at the beamline ID09 at European Synchrotron Radiation Facility (ESRF) in Grenoble. A.Č. is very thankful to Mattia Giannini for his help with software installation and application.

Table 5.3: Parameters of isotropic refinements of coesite-I and II structures at various pressures

P (GPa)	**2.42**	**5.16**	**9.24**	**12.14**	**14.90**	**17.80**	**20.30**	**27.52**	**30.94**
Total number / unique reflections	627 / 439	667 / 427	518 / 396	563 / 405	637 / 412	609 / 396	600 / 393	2019 / 1123	1781/ 1002
$R_{int}/R\sigma$	0.0220/0.0296	0.0189/ 0.0291	0.0159 / 0.0261	0.0129 / 0.0189	0.0150 / 0.0193	0.0128 / 0.0162	0.0116 / 0.0185	0.0405/0.0459	0.0628 / 0.0611
$[F_{obs} > 4\sigma(F_{obs})]$ /restraints /parameters	376/ 0 / 24	348 / 0 / 24	329 / 0 / 24	351 / 0 / 24	366 / 0 / 24	355 / 0 / 24	345 / 0 / 24	811 / 0 / 97	715 / 0 / 97
Goodness of fit on F^2 [S]	1.057	1.123	1.078	1.161	1.148	1.109	1.139	1.124	1.045
Final R indices $[F_{obs} > 4\sigma(F_{obs})]$ R_1/wR_2	0.0553 / 0.1622	0.0346 / 0.0907	0.0302 / 0.0789	0.0344 / 0.1021	0.0340 / 0.0981	0.0375 / 0.1097	0.0372 / 0.1023	0.051 / 0.1369	0.0959 / 0.2636
Final R indices R_1/wR_2 for all data	0.0608 / 0.1622	0.0445 / 0.0907	0.0384 / 0.0789	0.0400 / 0.1021	0.0378 / 0.0981	0.0415 / 0.1097	0.0422 / 0.1023	0.0787 / 0.1369	0.1221 / 0.2636
Largest diff. peak and hole (e / Å^3)	0.86 and -0.76	0.53 and -0.43	0.37 and -0.38	0.46 and -0.47	0.58 and -0.67	0.54 and -0.51	0.65 and -0.58	0.64 and -0.71	1.32 and -1.01
Systematic absences violations	0	0	0	0	0	0	0	0	1
Inconsistent equivalents	9	5	2	7	11	14	1	6	17
Recommended weighting	0.1270	0.0487 1.2285	0.0429 1.2410	0.0706	0.0615 0.9135	0.0684 1.8125	0.0593 1.8117	0.0568 6.2280	0.1958

Table 5.4a: Fractional atomic coordinates and isotropic displacement parameters of coesite-I at various pressures

	x	*y*	*z*	U_{iso}
2.42 GPa				
Si1	0.13887(24)	0.10923(10)	0.07142(18)	0.00571(41)
Si2	0.50807(22)	0.15748(10)	0.54309(17)	0.00523(41)
O1	0.0000	0.0000	0.0000	0.01073(92)
O2	0.5000	-0.11219(36)	0.2500	0.00772(86)
O3	0.73923(60)	0.12738(27)	0.56621(47)	0.00866(66)
O4	0.31575(62)	0.10210(27)	0.32678(47)	0.01032(71)
O5	-0.02328(65)	0.21177(27)	0.02517(50)	0.00921(69)
5.16 GPa				
Si1	0.13660(19)	0.11018(8)	0.07000(15)	0.00524(25)
Si2	0.50930(18)	0.15704(8)	0.54508(14)	0.00510(25)
O1	0.0000	0.0000	0.0000	0.01032(73)
O2	0.5000	-0.10878(27)	0.2500	0.00635(65)
O3	0.74830(49)	0.13069(20)	0.57351(39)	0.00891(51)
O4	0.31886(49)	0.10081(20)	0.32531(40)	0.00964(53)
O5	-0.02687(51)	0.21251(20)	0.02911(40)	0.00853(49)
9.24 GPa				
Si1	0.13451(19)	0.11145(7)	0.06828(14)	0.00513(23)
Si2	0.50985(18)	0.15649(7)	0.54689(13)	0.00529(24)
O1	0.0000	0.0000	0.0000	0.01190(67)
O2	0.5000	-0.10426(23)	0.2500	0.00643(60)
O3	0.75574(48)	0.13439(17)	0.58087(37)	0.00782(45)
O4	0.32389(50)	0.09922(18)	0.32404(40)	0.00992(49)
O5	-0.03370(47)	0.21271(18)	0.03181(36)	0.00844(45)
12.14 GPa				
Si1	0.13325(19)	0.11217(7)	0.06720(13)	0.00570(27)
Si2	0.50994(17)	0.15615(7)	0.54780(12)	0.00553(28)
O1	0.0000	0.0000	0.0000	0.01353(68)
O2	0.5000	-0.10218(24)	0.2500	0.00669(59)
O3	0.76001(47)	0.13676(18)	0.58549(35)	0.00841(45)
O4	0.32622(50)	0.09864(18)	0.32287(39)	0.00979(47)
O5	-0.03741(47)	0.21258(18)	0.03317(35)	0.00875(47)
14.90 GPa				
Si1	0.13137(19)	0.11291(7)	0.06571(13)	0.00487(25)
Si2	0.50954(17)	0.15583(7)	0.54838(13)	0.00445(26)
O1	0.0000	0.0000	0.0000	0.01368(69)
O2	0.5000	-0.10041(24)	0.2500	0.00606(58)
O3	0.76338(49)	0.13854(18)	0.58882(37)	0.00784(45)
O4	0.32655(53)	0.09786(18)	0.32154(41)	0.00905(47)
O5	-0.04076(49)	0.21284(18)	0.03394(36)	0.00796(46)
17.80 GPa				
Si1	0.13063(21)	0.11348(8)	0.06491(16)	0.00970(29)
Si2	0.50958(21)	0.15565(8)	0.54919(16)	0.00937(30)
O1	0.0000	0.0000	0.0000	0.01782(77)
O2	0.5000	-0.09804(27)	0.2500	0.00994(66)
O3	0.76676(58)	0.13999(20)	0.59224(44)	0.01264(53)
O4	0.32846(60)	0.09716(20)	0.32088(46)	0.01338(54)
O5	-0.04371(56)	0.21274(21)	0.03537(42)	0.01253(54)
20.30 GPa				
Si1	0.13034(21)	0.11379(8)	0.06437(16)	0.00636(28)
Si2	0.50942(21)	0.15551(8)	0.54951(16)	0.00582(28)
O1	0.0000	0.0000	0.0000	0.01697(81)
O2	0.5000	-0.09678(28)	0.2500	0.00683(65)
O3	0.76866(57)	0.14133(21)	0.59464(43)	0.00901(52)
O4	0.33018(60)	0.09676(21)	0.32117(48)	0.01081(53)
O5	-0.04608(56)	0.21279(21)	0.03575(43)	0.00925(53)

Note: Numbers in parentheses are the esd's in the last decimal place of each value.

Table 5.4b: Fractional atomic coordinates and isotropic displacement parameters of coesite-II at various pressures

	x	*y*	*z*	U_{iso}
27.52 GPa				
Si1	0.20478(40)	-0.20401(8)	0.46914(35)	0.00559(47)
Si2	0.32858(42)	-0.32003(8)	0.47855(36)	0.00543(46)
Si3	0.62880(42)	-0.06085(8)	0.94771(35)	0.00486(46)
Si4	0.70453(40)	-0.30081(8)	0.38018(35)	0.00517(46)
Si5	0.89180(41)	-0.07579(7)	0.58105(34)	0.00510(46)
Si6	0.77086(40)	0.04027(8)	0.55025(34)	0.00515(46)
Si7	0.58700(42)	-0.18435(7)	0.37450(36)	0.00516(45)
Si8	0.72817(41)	0.05686(8)	0.94088(35)	0.00533(46)
O1	0.44079(104)	-0.30040(19)	0.33058(88)	0.00631(104)
O2	0.14544(104)	-0.27186(19)	0.45578(85)	0.00657(105)
O3	0.88777(104)	-0.32975(19)	0.61640(88)	0.00662(105)
O4	0.73734(109)	-0.12909(20)	0.47533(91)	0.00902(111)
O5	0.47143(110)	-0.19929(20)	0.52022(93)	0.00864(107)
O6	0.73618(113)	-0.02535(19)	0.59720(90)	0.00888(110)
O7	0.81220(100)	-0.00947(19)	1.01289(85)	0.00539(104)
O8	0.53945(106)	-0.06247(19)	1.12206(88)	0.00699(107)
O9	1.08814(105)	-0.09258(18)	0.84076(86)	0.00531(104)
O10	0.20972(105)	-0.16994(19)	0.67212(87)	0.00607(103)
O11	0.02704(105)	-0.17197(19)	0.24174(89)	0.00708(108)
O12	0.76450(110)	-0.23356(19)	0.39227(90)	0.00832(109)
O13	0.72586(103)	0.07886(20)	0.71930(87)	0.00705(107)
O14	0.39220(108)	-0.04909(20)	0.71465(92)	0.00973(114)
O15	0.71371(107)	-0.11932(19)	0.90380(92)	0.00928(114)
O16	0.97940(115)	-0.05569(20)	0.41236(94)	0.01028(112)
30.94 GPa				
Si1	0.20106(51)	-0.20373(10)	0.46011(47)	0.00753(78)
Si2	0.32239(54)	-0.32007(10)	0.46922(50)	0.00774(79)
Si3	0.63015(53)	-0.06046(10)	0.94741(48)	0.00756(77)
Si4	0.70065(54)	-0.30134(10)	0.37210(48)	0.00802(77)
Si5	0.88998(52)	-0.07636(11)	0.58174(46)	0.00699(76)
Si6	0.77115(50)	0.03963(10)	0.55068(45)	0.00665(78)
Si7	0.58594(54)	-0.18504(10)	0.37046(50)	0.00748(75)
Si8	0.72692(51)	0.05769(10)	0.93825(47)	0.00772(78)
O1	0.43607(141)	-0.29983(25)	0.32223(120)	0.00780(142)
O2	0.13900(134)	-0.27178(25)	0.44832(114)	0.00807(142)
O3	0.88562(143)	-0.33040(27)	0.61051(125)	0.01114(150)
O4	0.73619(143)	-0.13020(27)	0.47243(124)	0.01374(161)
O5	0.46907(150)	-0.19970(27)	0.51681(132)	0.01224(157)
O6	0.73390(139)	-0.02588(25)	0.59980(118)	0.00862(140)
O7	0.81109(136)	-0.00919(27)	1.01288(120)	0.01181(151)
O8	0.54118(142)	-0.06344(26)	1.12732(122)	0.01114(152)
O9	1.08697(140)	-0.09403(26)	0.84255(113)	0.00807(152)
O10	0.20496(129)	-0.16907(25)	0.66384(109)	0.00666(143)
O11	0.01992(151)	-0.17140(27)	0.23066(133)	0.01397(160)
O12	0.76065(142)	-0.23402(25)	0.38418(130)	0.01025(150)
O13	0.72485(130)	0.07951(26)	0.71142(114)	0.00849(143)
O14	0.38789(138)	-0.04672(27)	0.71732(118)	0.01091(148)
O15	0.70703(151)	-0.11848(28)	0.88842(136)	0.01630(169)
O16	0.97500(142)	-0.05568(27)	0.41117(123)	0.01185(155)

Note: Numbers in parentheses are the esd's in the last decimal place of each value.

Table 5.5: Selected tetrahedral distances (Å) and angles (°) in coesite-I at various pressures

P (GPa)	**2.42**	**5.16**	**9.24**	**12.14**	**14.90**	**17.80**	**20.30**
Si1 tetrahedra							
Bond length							
Si1-O1	1.5865(13)	1.5770(10)	1.5665(9)	1.5602(9)	1.5537(9)	1.5484(10)	1.5440(10)
Si1-O4	1.6063(34)	1.6017(28)	1.5985(28)	1.5944(27)	1.5915(29)	1.5879(32)	1.5884(33)
Si1-O3	1.6174(32)	1.6087(26)	1.6034(24)	1.6030(23)	1.5993(23)	1.5953(26)	1.5948(25)
Si1-O5	1.6201(37)	1.6167(29)	1.6137(26)	1.6085(25)	1.6041(26)	1.6004(29)	1.6012(29)
<Si(1)-O>	1.6076	1.6010	1.5955	1.5915	1.5872	1.5830	1.5821
Edge length							
O1-O3	2.6368(44)	2.6164(35)	2.6048(33)	2.6004(31)	2.5939(33)	2.5851(37)	2.5848(37)
O1-O4	2.5841(30)	2.5607(23)	2.5284(22)	2.5085(22)	2.4852(22)	2.4663(26)	2.4568(27)
O1-O5	2.6222(37)	2.619(25)	2.6088(22)	2.5991(22)	2.5932(22)	2.5846(25)	2.5791(25)
O3-O4	2.6488(55)	2.6485(44)	2.6519(43)	2.6538(38)	2.6512(42)	2.6522(47)	2.6575(47)
O3-O5	2.6196(59)	2.5981(57)	2.5977(52)	2.5923(49)	2.5885(52)	2.5851(59)	2.5853(48)
O4-O5	2.6306(46)	2.6303(34)	2.6402(33)	2.6380(32)	2.6365(33)	2.6331(38)	2.6364(39)
<O-O> in Si1	2.6237	2.6122	2.6053	2.5987	2.5914	2.5844	2.5833
Intratetrahedral angles							
O3-Si1-O1	110.74(14)	110.54(10)	110.51(9)	110.58(9)	110.70(9)	110.62(11)	110.81(11)
O4-Si1-O1	108.43(14)	107.38(10)	106.04(9)	105.34(9)	104.39(9)	103.69(11)	103.29(11)
O5-Si1-O1	109.61(17)	110.28(13)	110.23(12)	110.21(12)	110.40(12)	110.33(13)	110.13(13)
O3-Si1-O4	110.52(20)	111.37(16)	111.83(15)	112.19(15)	112.38(15)	112.85(18)	113.17(17)
O5-Si1-O3	107.93(17)	107.53(14)	107.07(12)	107.65(12)	107.81(12)	107.99(14)	107.94(14)
O5-Si1-O4	109.60(18)	109.77(14)	110.55(13)	110.90(12)	111.18(12)	111.35(14)	111.48(14)
Tetrahedral volume	2.1380	2.0985	2.0803	2.0632	2.0444	2.0265	2.0228
Quadratic elongation	1.0004	1.0008	1.0015	1.0020	1.0026	1.0032	1.0037
Angle variance	1.3210	2.6823	4.6662	6.3271	8.4654	10.5368	12.1043
Si2 tetrahedra							
Bond lenght							
Si2-O4	1.6010(35)	1.5994(29)	1.5874(28)	1.5818(27)	1.5815(29)	1.5771(32)	1.5680(33)
Si2-O2	1.6070(19)	1.6033(15)	1.5996(14)	1.5949(14)	1.5889(14)	1.5884(17)	1.5860(17)
Si2-O3	1.5984(37)	1.6080 (30)	1.6030 (30)	1.5993(28)	1.6009(29)	1.5978(34)	1.5941(33)
Si2-O5	1.6187(36)	1.6096(27)	1.6069(24)	1.6086(23)	1.6046(24)	1.6042(27)	1.6018(27)
<Si(2)-O>	1.6063	1.6051	1.5992	1.5962	1.5940	1.5919	1.5875
Edge length							
O2-O3	2.6172(48)	2.6232(40)	2.6089(39)	2.5982(36)	2.5905(38)	2.5830(44)	2.5766(44)
O2-O4	2.6197(33)	2.6129(26)	2.5993(26)	2.5955(26)	2.5910(27)	2.5854(33)	2.5756(34)
O2-O5	2.6456(56)	2.6428(41)	2.6418(32)	2.6412(30)	2.6362(33)	2.6409(40)	2.6398(40)
O3-O4	2.6061(50)	2.6142(40)	2.5968(39)	2.5909(38)	2.5969(38)	2.5876(44)	2.5784(45)
O3-O5	2.6193(59)	2.6173(46)	2.6088(41)	2.6018(41)	2.5955(41)	2.5919(48)	2.5849(48)
O4-O5	2.6289(46)	2.6232(34)	2.613(31)	2.6103(30)	2.6066(31)	2.6068(35)	2.6003(35)
<O-O> in Si2	2.6228	2.6223	2.6114	2.6063	2.6028	2.5993	2.5926
Intratetrahedral angles							
O2-Si2-O4	109.34(15)	109.25(12)	109.30(11)	109.58(11)	109.62(11)	109.52(13)	109.46(14)
O3-Si2-O4	108.81(18)	109.16(14)	108.96(13)	109.07(13)	109.38(13)	109.18(15)	109.25(15)
O5-Si2-O4	109.33(18)	109.56(14)	109.77(13)	109.81(13)	109.79(13)	110.05(15)	110.19(16)
O3-Si2-O2	109.63(14)	109.48(11)	109.10(10)	108.86(10)	108.61(10)	108.33(12)	108.19(12)
O5-Si2-O2	110.46(18)	110.54(14)	110.95(12)	111.07(11)	111.27(12)	111.62(13)	111.76(13)
O5-Si2-O3	109.24(18)	108.83(14)	108.73(12)	108.40(12)	108.13(13)	108.09(15)	107.93(14)
Polyhedral volume	2.1261	2.1249	2.0984	2.0860	2.0775	2.0688	2.0528
Quadratic elongation	1.0001	1.0001	1.0002	1.0003	1.0003	1.0005	1.0006
Angle variance	0.2276	0.3618	0.6527	0.8729	1.1825	1.6556	1.9684

Note: Quadriatic elongation and tetrahedral variance calculated using PROGRAM METRIC Ver. 6.1 by Bartelmehs et al. 2002., which is based on Robinson et al. 1971. Numbers in parentheses are the esd's in the last decimal place of each value.

Table 5.6: Selected intertetrahedral distances (Å) and angles (°) in coesite-I at various pressures

P (GPa)	**2.42**	**5.16**	**9.24**	**12.14**	**14.90**	**17.80**	**20.30**
Si1-O1-Si1	180	180	180	180	180	180	180
Si2-O2-Si2	139.46 (31)	136.76 (25)	133.36 (20)	131.82 (19)	130.50 (20)	128.64 (22)	127.70 (22)
Si1-O3-Si2	143.13 (24)	140.76 (20)	138.32 (17)	136.67 (17)	135.61 (18)	134.33 (21)	133.41 (20)
Si1-O4-Si2	149.40 (23)	149.15 (19)	148.28 (16)	147.91 (15)	147.28 (16)	146.63 (18)	146.17 (18)
Si1-O5-Si2	134.62 (27)	133.14 (22)	130.26 (18)	128.77 (18)	127.65 (18)	126.44 (20)	125.54 (20)
Si2-Si2	3.9109 (17)	3.8825 (14)	3.8416 (12)	3.8165 (12)	3.7914 (12)	3.7717 (14)	3.7560 (14)
Si1-Si1	7.0601 (6)	6.9829 (6)	6.8746 (6)	6.8070 (7)	6.7549 (11)	6.6921 (11)	6.6548 (15)
O3-O4 planes	2.9953 (54)	3.0163 (38)	3.0243 (34)	3.0348 (34)	3.0341 (34)	3.0335 (39)	3.0345 (39)
O(1)-O(1)	3.5703 (2)	3.5535 (2)	3.5274 (2)	3.5111 (2)	3.4931 (3)	3.4791 (3)	3.4679 (5)
O(3)-O(3)	4.0372 (39)	4.1094 (31)	4.1555 (31)	4.1860 (25)	4.2051 (32)	4.2216 (33)	4.2299 (36)
O(4)-O(4)	3.3062 (68)	3.2064 (56)	3.0910 (55)	3.0243 (55)	2.9836 (54)	2.9304 (66)	2.8983 (66)
O(1)-O(2)	3.3401 (21)	3.2815 (15)	3.2072 (10)	3.1655 (10)	3.1337 (11)	3.0929 (15)	3.0686 (17)
O(1)-O(3)	3.1052 (31)	3.0627 (24)	3.0177 (23)	2.9927 (19)	2.9719 (23)	2.9495 (24)	2.9346 (25)
O(1)-O(4)	3.2932 (47)	3.2953 (38)	3.2850 (37)	3.2775 (37)	3.2622 (37)	3.2513 (44)	3.2440 (44)
O5a-O5b	3.0561 (59)	2.9664 (47)	2.8680 (44)	2.8162 (35)	2.7754 (43)	2.7299 (44)	2.7042 (43)
O5a-O5c	3.1797 (71)	3.0718 (59)	2.9137 (49)	2.8314 (47)	2.7615 (48)	2.6931 (56)	2.6452 (56)
O5a-O5d	3.6448 (44)	3.6028 (35)	3.5494 (31)	3.5209 (28)	3.4965 (32)	3.4700 (35)	3.4501 (37)

Note: Si1-Si1 and Si2-Si2 are distances across the hollow channels. O3-O4 planes are marked in Figure 6. Numbers in parentheses are the esd's in the last decimal place of each value.

6. HIGH-PRESSURE BEHAVIOUR OF CRISTOBALITE: BRIDGING THE GAP TOWARDS THE "SEIFERTITE ENIGMA"

Ana Černok[1], Katharina Marquardt[1], Razvan Caracas[2], Elena Bykova[1], Gerlinde Habler[3], Hanns-Peter Liermann[4], Michael Hanfland[5], Mohamed Mezouar[5], and Leonid Dubrovinsky[1]

[1]Bayerisches Geoinstitut, Universitätsstrasse 30, 95447 Bayreuth, Germany,

[2]Centre National de la Recherche Scientifique Laboratoire de Geologie de Lyon (LGLTPE) UMR 5276 Ecole Normale Supérieure de Lyon 46, allée d'Italie, 69364 Lyon, France

[3]Department of Lithospheric Research, University of Vienna, Althanstrasse 14, 1090 Vienna, Austria

[4]Photon Sciences, Deutsches Elektronen-Synchrotron (DESY), Notkestraße 85, 22607 Hamburg, Germany

[5]European Synchrotron Radiation Facility (ESRF), 6 Rue Jules Horowitz, 38000 Grenoble, France

(Manuscript ready to be submitted)

6.1 Abstract

In order to reconcile contradictory results available so far on high-pressure behaviour of α-cristobalite regarding different outcomes when the same starting material is compressed at different levels of hydrostaticity, we conducted series of experiments at high-pressures and at room temperature at variable stress conditions, using starting material in form of single crystals and powders. We find that in highly hydrostatic environment α-cristobalite remains untransformed to at least ~15 GPa. Under quasi-hydrostatic conditions, intermediated by cristobalite-II, α-phase undergoes a first-order reconstructive phase transition to cristobalite X-I above ~10 GPa at ambient temperature. The phase X-I is found to exist at least up to ~80 GPa and to convert back to the starting cristobalite upon pressure release. We solve the structure of cristobalite X-I - a polymorph containing kinked chains of octahedra similar to those in seifertite - by means of single-crystal X-ray diffraction. This polymorph shows a distorted anion close-packing arrangement with randomly distributed cations, thus belonging to the same family as the "3 x 2 zigzag" polymorph found on compression of quartz. The increase in

coordination number of silicon from 4 to 6 on cold compression has not been observed to occur at such low pressures (~10 GPa) in any other silica polymorph. In non-hydrostatic environment cristobalite eventually transforms to seifertite, the high-pressure silica polymorph (α-PbO_2 type) at maximum of ~50 GPa. Seifertite formed far below its *P-T* thermodynamic stability field following the sequence of transitions α -> II -> X-I -> α-PbO_2 bypasses the equilibrium formation of stishovite and $CaCl_2$ structured polymorph, and, as reported earlier, it can be recovered to ambient conditions.

6.2 Introduction

The Si-O bond is significantly stronger than the bond of any other element with oxygen (Putnis, 1992) thus providing for silica, SiO_2, to be the dominant (~60 wt %) oxide constituent of the earth's crust and it comprises ~45 wt % of the entire *Silicate Earth* (McDonough and Sun, 1995). Not only does this strong bond, that requires a lot of energy to be broken, causes the rich polymorphism amongst thermodynamically stable SiO_2 phases, but it also plays the essential role in facilitating numerous metastable polymorphs to exist in a wide range of pressure and temperature conditions. In terms of studying the structure and behaviour of materials at elevated pressures utilizing cutting-edge experimental procedures, silica remains one of the most challenging compounds due to its relatively low X-ray scattering factor, as well as its abundant polymorphism.

Cristobalite, a high-temperature, low-pressure polymorph of silica, that consists of an open framework of SiO_4 tetrahedra, can be metastably preserved at ambient conditions in its α-form. Although it has a subordinate and rather exotic terrestrial occurrence among silica phases, α-cristobalite is observed as the predominant SiO_2 polymorph in various planetary materials: from dust particles in proto-planetary disks surrounding T-Tauri stars (Koike et al., 2013), over lunar basalts (Rasmussen et al., 2008) to chondrules and matrix of chondritic meteorites (Brearley and Jones, 1998). Cristobalite was documented alongside all the natural occurrences of the high-pressure, post-stishovite silica polymorph seifertite (e.g. Bläß, 2013; Miyahara et al., 2013), related to the heavily shocked meteorites. The intriguing questions on importance of cristobalite high-pressure behaviour, however, arise from the fact that it was often documented in the meteorites that lack any high-pressure silica polymorphs (Leroux and Cordier, 2006; Weber et al., 2000), albeit the rest of the mineral record indicates peak shock pressures exceeding 10 GPa, at which at least coesite or stishovite are expected to form and be preserved. The response of α-cristobalite to high-pressures has been a subject of numerous experimental (Dera et al., 2011; Dove et al., 2000; Downs and Palmer,

1994; Dubrovinsky et al., 2001; Onodera et al., 1997; Palmer et al., 1994; Tsuchida and Yagi, 1990) and theoretical (Donadio et al., 2008; Dubrovinsky and Belonoshko, 1996; Huang et al., 2006; Martoňák et al., 2007; Teter et al., 1998) studies for more than two decades, indicating abundant polymorphism at elevated pressures. Yet, no consensus has emerged on what is the exact sequence of the pressure-induced transformations, particularly due to contradictory outcomes arising when different levels of hydrostaticity are applied in experiments (Dera et al., 2011; Dubrovinskaia et al., 2001; Prokopenko et al., 2001). The structure of the "bridging phase" that appears above ~10 GPa in either highly-, low- or non-hydrostatic conditions – hereafter cristobalite X-I – remained elusive in earlier attempts (Tsuchida and Yagi, 1990; Dera et al., 2011). Single-crystals of α-cristobalite have never been studied at pressures exceeding the formation of cristobalite X-I. Experimental studies (Dubrovinsky et al., 2001; Dubrovinskaia and Dubrovinsky, 2001; Prokopenko et al., 2001) carried out at non-hydrostatic conditions by using powders as starting material report transformation of α-cristobalite, via intermediates cristobalite-II and cristobalite X-I, directly to the post-stishovite phase seifertite - α-PbO_2-type silica. This "enigmatic" transformation path provides an evidence that seifertite, the highest-pressure polymorph of SiO_2 ever found in nature (Dubrovinskaia et al., 2001), can form at pressures much lower than its thermodynamic equilibrium i.e. in excess of 80 GPa (Driver et al., 2010; Dubrovinsky et al., 1997; Grocholski et al., 2013; Murakami et al., 2003) bypassing formation of stishovite and post-stishovite $CaCl_2$ polymorph. The structure of cristobalite X-I may therefore represent a direct link between the low-pressure (silicon in SiO_4 tetrahedra) and the high-pressure (SiO_6 octahedra) forms of silica.

We conducted series of experiments at high-pressures and at room temperature in order to reconcile contradictory outcomes available so far, by compressing powders and single crystals α-cristobalite in different environment thus providing different stress conditions. We mostly focused on the stability and structure of cristobalite X-I phase. We used diamond-anvil cells (DAC) for high-pressure experiments; *in situ* high-pressure data were obtained by Raman spectroscopy and synchrotron based single-crystal X-ray diffraction (SCXRD). The experimental investigations of cristobalite X-I were complemented by *ab initio* calculations of the Raman modes. After high-pressure treatment, recovered samples were additionally examined by powder X-ray diffraction (PXRD) and transmission electron microscopy (TEM). The results reveal that the mechanism which α-cristobalite adapts to respond to compression is even more sensitive to stress conditions than previously anticipated.

6.3 Experiments & methods

6.3.1 Samples and high-pressure experiments

For the experiments we used synthetic cristobalite as well as the natural samples kindly provided by Harvard Museum (Ellora Caves MGMH Cristobalite 97849). Composition of the starting material for synthesizing cristobalite was SiO_2 glass of very low impurity content (Černok et al., 2014). Composition of natural cristobalite was measured using ICP-MS at BGI, and showed content of Al, Fe and Na in trace amounts of maximal of ~1000 ppm, comparable to that reported before (Peacor, 1973.). Cristobalite was synthesized by heating the glass granules at the temperatures of ~1650 °C for 3 hours and then cooling down slowly over 15 hours to ~1500 °C (temperature slightly higher than that of cristobalite-trydimite transition), and then rapidly quenched. This procedure allowed the growth of cristobalite crystals up to ~100 μm in linear dimension; however it was not possible to avoid twinning which occurs on cooling due to the transition from the cubic *β*-cristobalite to the tetragonal *α*-cristobalite. These crystals were of the sufficient quality for the Raman spectroscopy but for the single crystal X-ray diffraction we had to use the natural cristobalite.

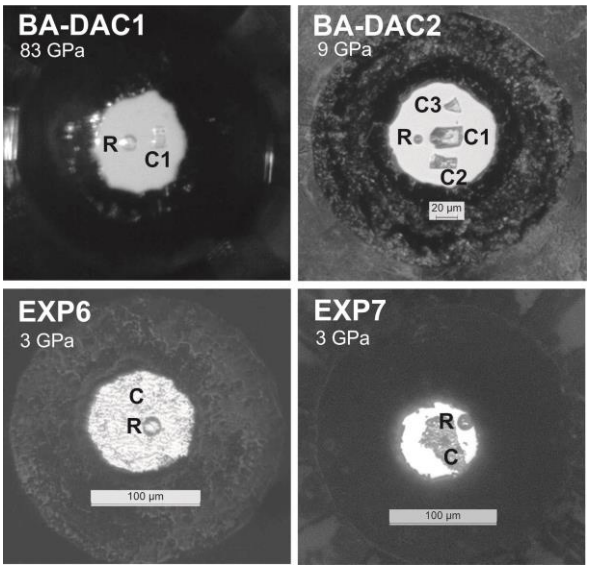

FIGURE 6.1. Photos of the representative DAC experiments. We carried out seven compression & decompression experiments on single crystals and powders of α-cristobalite up to variable pressures (max. ~83 GPa). All experiments were carried out at room temperature. R stands for ruby; C1, C2 and C3 are single crystals of cristobalite; C is powder of cristobalite. BA-DAC 1 & 2 are the single crystal set-ups, analyzed at synchrotron. EXP 6 & 7 are powder samples analyzed *in situ* using Raman spectroscopy, and upon quenching by in-house X-ray diffractometer and TEM.

High-pressure experiments were carried out on both single crystals and powders (Fig. 6.1; Table 6.1). All single crystal experiments were conducted in quasi-hydrostatic conditions, using a pressure-transmitting medium, whereas powders were also studied in non-hydrostatic environment. We used piston-cylinder BX90 type diamond anvil cells (DAC) produced at BGI (Kantor et al., 2012) with 250 μm culet size of the anvils. Samples were loaded together with a ~5 μm in diameter ruby sphere into a cylindrical pressure chamber of 30–40 μm height and ~125 μm diameter drilled in a pre-indented rhenium gasket. Neon, used as pressure transmitting medium, was loaded into the DAC using the BGI gas loading system (Kurnosov et al., 2008). We chose neon for the pressure-transmitting medium, because it was shown that helium, providing slightly better hydrostaticity, can be easily incorporated in cavities of the cristobalite structure (Sato et al., 2013). For Raman experiments we used Ia type diamonds with low fluorescence. For *in situ* single crystal X-ray diffraction we used Boehler-Almax diamond anvils (Boehler and De Hantsetters, 2004) and apertures of 80°, to allow for large reciprocal space coverage.

Table 6.1: List of the conducted experiments.

Exp1 & Exp4	Single crystals of α-cristobalite up to ~60 GPa, in neon pressure medium: Raman spectra recorded on compression & decompression; synchrotron XRD carried out on the quenched samples; TEM on Exp1.
Exp5	Rapid compression on a single crystal up to 12 GPa and immediate quench; Raman spectroscopy.
Exp6	Powder with no pressure medium up to ~50 GPa; quenched sample analyzed by in-house XRD + TEM
Exp7	Powder with pressure medium up to ~50GPa; quenched sample analyzed by Raman spectroscopy
BA-DAC1	(Böhler-Almax DAC): In-situ synchrotron single crystal X-ray diffraction up to ~83 GPa (ESRF ID09A & Petra III)
BA-DAC 2	*In situ* synchrotron SC-XRD at 14.1 GPa (ESRF ID27)

6.3.2 Raman spectroscopy

Raman spectroscopy measurements were performed using a Dilor XY Raman spectrometer with Ar^+ ion laser (514.5 nm, Coherent Innova 300). The spectrometer is equipped with confocal optics, a CCD detector cooled by liquid nitrogen, and a double-stage spectrometer with a 1800 g/mm grating, resulting in spectral resolution of 1 cm^{-1}. The output power was varied according to the sample signal between 0.3 and 1.0 W. The spectrometer was calibrated using the silicon peak at 520 cm^{-1}. Raman spectra were collected between 100 and 1200 cm^{-1} in all DAC experiments at room temperature by pressurizing the stating material in steps of several GPa up to a maximum of ~83 GPa, and, in the same manner, also during decompression to ambient conditions. Data were typically collected for 120

seconds, using Labspec software. Peak positions in the Raman spectra were determined using Lorentzian peak fitting setup in Igor Pro v. 6.22 software.

6.3.3 In-house X-ray diffraction

Single crystals of α-cristobalite were selected at the Bayerisches Geoinstitut (BGI) based on their optical quality – size, transparency, crystal shape, surface appearance, etc. Very small crystals (up to ~30 μm in linear dimension) were tested using a rotating anode high-brilliance Rigaku diffractometer with MoKα radiation (λ=0.7080 Å) operated at 60 kV and 50 mA, equipped with Osmic focusing X-ray optics and a Bruker Apex CCD detector. The same diffractometer was used to analyze the quenched powder from the EXP6. The fine-grained powder was collected on a capillary and powder-diffraction data were collected for 3600 seconds. To improve the quality of the data, we subtracted the pattern collected on an empty capillary for the same duration of time.

6.3.4 Synchrotron X-ray diffraction

The structural behaviour of cristobalite was investigated up to ~83 GPa at room temperature. High-pressure single crystal X-ray diffraction experiments were performed at the beamlines ID09A and ID27 at ESRF (Grenoble, France) and at the Extreme Conditions Beamline (ECB, P02.2) at PETRA III in Hamburg. At each pressure point, wide-scan diffraction images were collected in the ω range of ± 40 ° for 3 s. In addition, 80 (or sometimes 160) independent step-scan diffraction frames were collected with time exposure of 1 s/step in the same ω range. At ID09A, data were collected for the experiment BA-DAC1 up to the pressure of phase transition α-cristobalite to cristobalite –II (~4.5 GPa) using 30 μm X-ray beam with a wavelength of 0.4144 Å and a MAR555 flat panel detector, located at the distance of 300 mm from the sample. At PETRA III we continued the experiment on the same crystal up to ~83 GPa GPa, using 2 × 4 μ m 2 (FWHM) X-ray beam with a wavelength of 0.29004 Å. The detector used was a PerkinElmer XRD1621 flat panel, located at the distance of 400.8 mm. At ID27 we analyzed new crystal loaded as BA-DAC2 at 13.8 GPa. A PerkinElmer flat panel detector was located at 389 mm. The wavelength of the used radiation was 0.3738 Å. Pressure was determined using the ruby pressure gauge (Mao et al., 1986) both before and after collection of X-ray. As well as by using neon EOS reported by Fei et al. (Fei et al., 2007). Single-crystal data have been reduced with the CrysAlis software package (Oxford Diffraction) and analyzed with the SHELX97 (Sheldrick, 2008) program package as implemented in the WingX software (Farrugia, 1999). Isotropic structure refinements of intermediate polymorphs were performed based on F^2 starting from the atomic coordinates for α-cristobalite and cristobalite II at ambient conditions, reported by Dera et al. (Dera et al., 2011). The structure of cristobalite X-I was solved by direct

method using SHELXS and refined by full matrix least squares in the isotropic approximation using SHELXL, both programs being implemented in SHELX97 software.

6.3.5 TEM sample preparation and Focused Ion Beam (FIB) sputtering

Two samples recovered after high-pressure experiments were prepared for the TEM analyses, the single crystal from experiment EXP4 and powder from the EXP6. We aimed at investigating the crystal from BA-DAC1 but it was unfortunately lost during preparation. Two different sample preparation methods were applied.

The larger amount of the fine-grained EXP6 powder was first analyzed by PXRD and then prepared for additional TEM analyses. The agglomerate of several grains was crushed between two glass slides. The obtained powder was dissolved with a drop of ethanol. On this drop we placed a copper grid with at lacey carbon film on which the powder remained fixed after the ethanol evaporated.

The EXP4 single crystal, as well as the small amount EXP6 powder which remained fixed to the rhenium gasket after the DAC was opened, were prepared using Focused Ion Beam (FIB) sputtering. The EXP4 quenched crystal were fixed by superglue to a glass, so that only a very thin layer of the superglue was covering the surface (< 3 μm), and coated by a ~15 nm thin carbon layer. The EXP6 powder was extracted directly from the gasket. We used two dual-beam instruments, one FEI QuantaTM 3D FEG located at the Faculty of Geosciences, Geography and Astronomy at the University of Vienna and one newly installed FEI Scios dual-beam instrument located at BGI, Bayreuth. The sample preparation followed the general path of Ga^+ ions being accelerated by applying an accelerating voltage of 30 kV. During foil extraction by FIB the sample surface was oriented perpendicular to the ion beam incidence direction by sample tilting. An Omniprobe 100.3 micromanipulator and an Easylift system with a tungsten needle were used respectively for *in situ* lift-out of the pre-thinned foil and transfer of the foil to a Cu-grid. The foil was fixed to the tungsten needle was fixed to the foil by Pt deposition. The foil was finally thinned at both sides using progressively lower ion beam currents from 1.0 nA to 30 pA in order to produce ~100 nm thin, electron-transparent foils of the quenched material. The final polishing was perfomed at lower accelearation voltages, down to 2 kV to minimize surface amorphization (e.g. Kato, 2004; Schaffer et al., 2011).

6.3.6 Transmission electron microscopy

The FEI Titan G2 80-200 with ChemiSTEM technology at BGI was operated at an acceleration voltage of 200 keV, event thought the X-FEG allows obtaining very high brightness; we tuned the microscope to lower the current and minimize beam damage of the sensitive samples. The particles

were either first imaged in BF mode or in STEM mode. For the former, we either used a selected area aperture of 10 or 40μm to obtain diffraction pattern (SEAD). The composition of the agglomerates was confirmed using EDX-ray spectroscopy either in scanning transmission electron microscopy (STEM) in combination with the high angle annular dark field (HAADF), bright field (BF), dark field (DF) detector or in nano-diffraction. Some particles were imaged in high resolution mode and 2D Fourier transformation patterns were calculated to obtain the *d*-spacings and angles between so obtained diffraction spots.

6.3.7 *Ab initio* calculations

We analyze the phonon softening also from first-principles calculations. We determine the ground-state properties using standard density-functional theory (Kohn and Sham 1965; Payne et al. 1992; Martin 2003) in the ABINIT implementation, based on planewaves and pseudopotentials (Gonze et al. 2002, 2009). Starting from the crystal structure refined in this study we determine the theoretical structure of cristobalite X-I at three different steps: 10, 40 and 100 GPa. Then we compute the energy derivatives to build the dynamical matrices and the Raman tensors in the framework of the density-functional perturbation theory (Baroni et al. 2001; Gonze et al. 2005; Veithen et al. 2005). We employ a 4x4x4 grid of special k points (Monkhorst and Pack) to sample the electron density in the reciprocal space and a kinetic energy cutoff of 38 Hartrees (1 Hartree = 27.2116 eV). With these parameters the precision of the calculation is typical on the order of 0.001 Hartree in energy and better than 1 GPa in pressure. We store all the Raman spectra computed under pressure on the WURM website (http://www.wurm.info). More details of the Raman calculations can be found in the original WURM paper (Caracas and Bobocioiu, 2011).

6.4 Results and discussion

6.4.1 Transformation path and the effect of hydrostaticity

Single-crystal experiments, carried out under quasi-hydrostatic conditions in Ne pressure-transmitting medium, indicated that the pressure-induced transformation path of α-cristobalite to its final product largely depends on the geometry of stresses applied to the crystals i.e. hydrostaticity. This effect is illustrated in Figure 6.2: three different in size α-cristobalite single crystals inside the same pressure chamber are surrounded by neon pressure medium. Upon compression, the smallest and the thinnest crystal C3 (~10 μm), that does not bridge between the anvils, thus remaining in highly hydrostatic

conditions, retains the structure of α-cristobalite up to at least ~15 GPa. On the other hand, the two larger crystals (C1 & C2) are bridged by anvils and undergo a displacive phase transition to cristobalite-II near 1 GPa, and, following this transitional path, eventually transform to cristobalite X-I just above ~10 GPa, supporting earlier findings (Prokopenko et al., 2001; Dera et al., 2011). The spectra of cristobalite X-I can be followed up to ~80 GPa under compression (the maximal pressures studied here). All experiments carried out on powders, regardless on the presence of the pressure-transmitting medium, showed no difference in the transformation path, and resulted in formation of seifertite (Figs. 6.8, 6.9), in agreement with previous experiments (Dubrovinsky et al., 2001; Dubrovinskaia et al., 2001; Prokopenko et al., 2001).

6.4.2 The "highly" hydrostatic compression

The thinnest crystal of α-cristobalite does not bridge between the anvils and experiences highly hydrostatic compression, thereby retaining the tetragonal structure up to at least ~15 GPa. Above this pressure we observed that single crystal α-cristobalite disintegrated into a powder-like material. The Raman spectra collected on α-cristobalite far outside its stability field ("overpressurized"), up to ~15 GPa are shown in Figure 6.2. The complementary XRD analyses delivered three important conclusions: 1) α-cristobalite can transform to cristobalite-II at pressures higher than ~1.5 GPa (in BA-DAC1 α-cristobalite was last observed at ~3 GPa, before it transformed to cristobalite-II); 2) it is impossible to distinguish between α-cristobalite and cristobalite-II above ~2 GPa solely based on the main A_g mode position, because the doublet characteristic of cristobalite-II merges into one intense peak upon further compression, having the same pressure shift as that of the α-cristobalite main mode (see below); 3) the "overpressurization" of α-cristobalite (in BA-DAC1, as well as in crystal C3 of BA-DAC2), is consistent with the observation by Dera et al. (2011); however, we do not find any evidences that it is caused by very rapid compression far beyond the α->II transition pressure (~1.5 GPa) as suggested by Dera et al. (2011). The observed transition at higher pressure (BA-DAC1), as well as the coexistence of α-cristobalite with cristobalite-II and cristobalite X-I (BA-DAC2, Fig. 6.2) to at least ~14 GPa strongly suggest that the main cause for the onset of the α->II transition is the change in stress conditions. Moreover, in order to test Dera et al. (2011) hypothesis we conducted an experiment applying the rapid compression (EXP5) by instantly increasing pressure to ~9 and then ~12 GPa. We still observed formation of phases II and X-I. The XRD analysis of the compressed α-cristobalite was measured at 1.55 and 14.1 GPa. It shows nice diffraction pattern of a single crystal with no indication of twinning, resulting in good *R* values of the integration and refinement (Table 6.2).

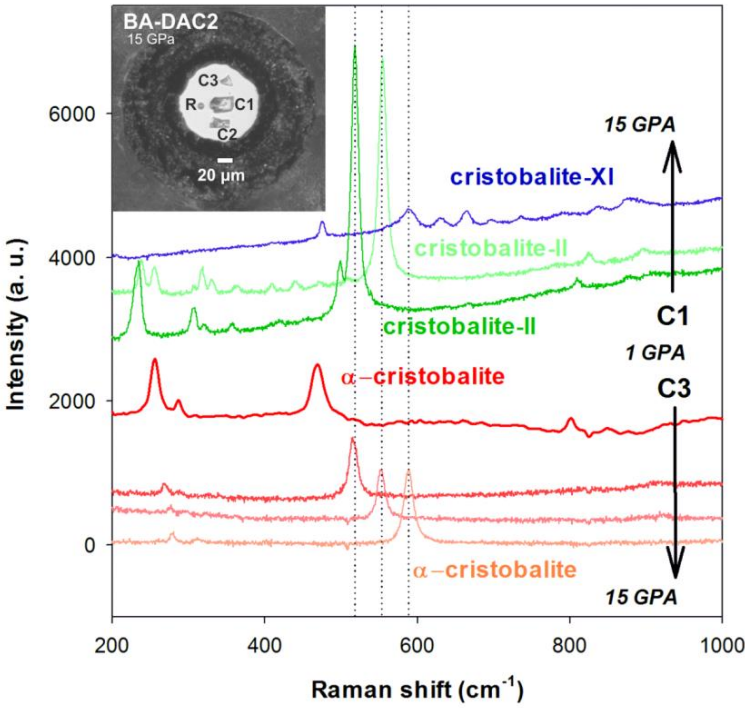

FIGURE 6.2. *In situ* Raman spectra collected on three different single crystals of α-cristobalite at 1.1, 4.6, 8.6 and 15.0 GPa and at room temperature. Inset shows the DAC pressure chamber seen at 14.1 GPa. In quasi-hydrostatic conditions the starting cristobalite (red) transforms via intermediate cristobalite-II (green) to cristobalite X-I (blue), but it retains its initial structure (orange) in the case of high hydrostaticity (smallest crystal size). All spectra are unsmoothed, the background is subtracted. Ar^+ laser was used (514 nm excitation wavelength) with ~0.8 W incident beam power.

Table 6.2: Unit cell parameters and refinement statistics of α-cristobalite and cristobalite-II.

	P_{ruby} [GPa]	a [Å]	b [Å]	c [Å]	β [°]	V [Å^3]	ρ [g/cm^3]	R_{int}	R_1
α-cristobalite ($P4_12_12$)									
in air[#Bruker]	0.00	4.9806(15)		6.9260(30)		171.82(11)	2.33	0.053	0.042
BA-DAC1[#ID09A]	1.55	4.8520(7)		6.6683(13)		156.99(7)	2.54	0.045	0.078
BA-DAC2[#ID27]	14.1	4.5202(15)		5.9645(16)		121.87(7)	3.27	0.021	0.067
cristobalite-II ($P2_1/c$)									
BA-DAC1[#ID09A]	4.50	8.0750(60)	4.5745(3)	8.9600(30)	121.03(7)	279.7(18)	2.88	0.046	0.150

Note: The structures were refined starting from the atomic coordinates of the respective polymorphs reported by Dera et al. (2011). Numbers in parentheses are the esd's in the last decimal place of each value.

6.4.3 Quasi-hydrostatic compression: α -> II ->X-I transitions

6.4.3.1 α-cristobalite and cristobalite-II

We started the compressional experiments using α-cristobalite. The formation of cristobalite-II was observed near ~1±0.2 GPa in most of the Raman experiments. Representative Raman spectra of one of the compression experiments are shown in Figure 6.2. The displacive transition to cristobalite-II is consistent with previous observations (Palmer et al., 1994), characterized by a decrease in intensity of the strongest A_g mode located at ~410 cm^{-1} followed by the appearance of an additional peak of comparable intensity near it, at slightly lower frequency, as well as an increase in the total number of vibrational modes due to the symmetry reduction from $P4_12_12$ to $P2_1/c$. The position of the main A_g mode continuously changes upon transition, in cristobalite-II. We, too, observe the cross-over of the two near modes described earlier (Palmer et al., 1994) that contributes to an abrupt increase in intensity upon further compression, after the two modes merge together.

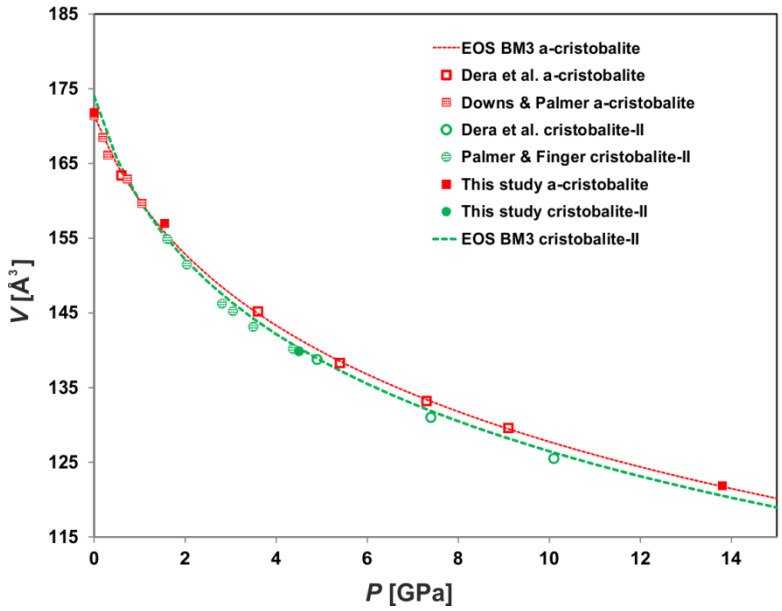

FIGURE 6.3. Unit-cell volume compressibility of α-cristobalite (red) and cristobalite-II (green; half unit cell volume) from this study, compared to various literature data. Full symbols are this study.

Upon the transition to cristobalite-II, the intense twinning is initiated. Analyzing one of crystal domains we were able to refine the structure with final *R* indices of ~15% (Table 6.2). The twinning is also observed in the previous study (Dera et al., 2011). The measured unit cell volumes of the polymorphs are within the error comparable to the previous studies (Dera et al., 2011; Dove et al., 2000; Downs and Palmer, 1994; Palmer and Finger, 1994). The parameters of the third-order Birch-Murnhagan equation of state (BM3 EOS) previously reported for α-cristobalite V_0=171.42 $Å^3$,

K_0=11.5(7) GPa and K´=9(2) (Dera et al. 2011) reproduce well our measured volumes even at the highest pressure (Fig. 6.3). However, we were not able to fit the EOS neither to our nor to literatures values using the parameters reported for cristobalite-II (Dera et al., 2011): V_0=348(14) Å^3, K_0=25(2) GPa and K´=4. Instead, we add our data point to the literature data set and refine following parameters: V_0=348(14) Å^3, K_0=8(4) GPa and K´=10(4). The EOS parameters we obtain by fixing the value of K´ to 4 are indistinguishable from those reported by Dera et al. (2011) within the error; however, they do not reproduce the *P-V* data.

6.4.3.2 Formation of cristobalite X-I

Cristobalite-II is observed up to ~11 GPa, after which it undergoes a first-order transition to cristobalite X-I, consistent with previous observations (Yahagi et al., 1994; Prokopenko et al., 2001). The abrupt change in Raman spectra appearance suggests that the structure of X-I phase is quite distinct from its α- and II precursors (Fig. 6.2). The spectra of cristobalite X-I can be followed up to ~80 GPa under compression (Fig. 6.4a), the maximal pressures studied here. On the decompression

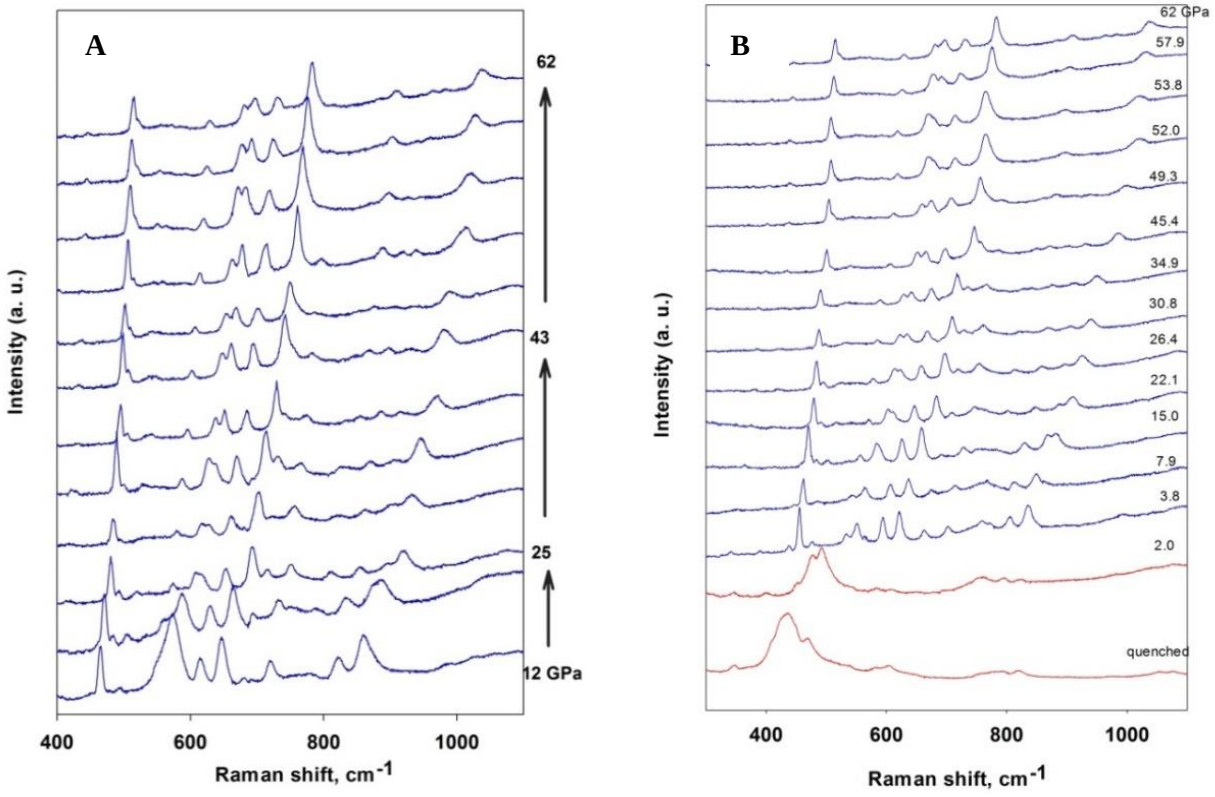

FIGURE 6.4. *In situ* Raman spectra collected under compression **(A)** and decompression **(B)** of cristobalite X-I. The pressure (in GPa) indicated on the right of the spectra. Upon decompression, cristobalite X-I transforms back to the starting α-cristobalite near 2 GPa.

route Raman modes of cristobalite X-I can be followed down to ~2 GPa , when it transforms back to the starting α-cristobalite (Fig. 6.4b, 6.7a). Due to similarity in spectra of α- and II phase, we cannot be sure whether the phase II is obscured on the decompression path or it exists in a very narrow range. In either case, the hysteresis of ~8 GPa suggests that the formation of the X-I phase involves a first-order phase transition. The experimental spectra of cristobalite X-I at various pressures were complemented with computational spectra, with which they show remarkable agreement throughout the pressure range (within 5 cm^{-1} or better, Fig. 6.5a and b). The computational spectra were calculated starting from the atomic coordinates obtained in this study (see below). None of the Raman modes is showing softening under pressure, strongly suggesting that cristobalite X-I, although thermodynamically metastable and unquenchable to ambient conditions, can exist in a wide pressure range.

6.4.3.3 The structure of cristobalite X-I

We reveal the structure of cristobalite X-I shown in Figure 6.6 by means of *in situ* synchrotron-based single crystal X-ray diffraction studies. All previously reported studies of this phase were based on powder diffraction insufficient to solve the structure. The atomic positions and structural refinements from this study are presented in Table 6.3. The structure was solved and refined in two independent experiments, analyzing different crystals in separate DAC loadings, at ~11 and ~14 GPa, respectively. In the first attempt we were only able to obtain a model of the structure, but the very weak intensities of the diffraction spots had led to poor refinement statistics (R_{int}=5 %, R_1=18%). However, the second experiment (~14 GPa) delivered data of sufficient quality for the proper structural solution and refinement, also confirming that the model of the structure is correct. Atomic parameters of the structure with lattice parameters: a=6.5700(23) Å, b=4.0633(6) Å, c=6.8345(45) Å, β=98.00(6)°, V=180.69(15) $Å^3$ in $P2_1/n$ (Z=8, ρ=4.42 g/cm^3) determined by single crystal XRD at 14.1 GPa are reported in Table 3. The refinement parameters are as follows: total number of unique reflections 209, R_{int}=4.6%, R_1=9.3%, wR_2=0.2588, GooF=1.127, 30 parameters refined, 0 restrictions.

Table 6.3: Structure of cristobalite X-I at 14.1 GPa in $P2_1/n$.

Atom	Site	Occupancy	*x*	*y*	*z*	U_{iso} [$Å^2$]
Si1	2d	1	0	0.5	0.5	0.0412(12)
Si2	4e	1	-0.1398(2)	0.49819(16)	0.1205(3)	0.0310(11)
Si3	4e	0.5	-0.2282(6)	-0.0061(4)	0.7663(9)	0.0416(11)
O2	4e	1	-0.2097(4)	0.2355(6)	0.5462(6)	0.0307(12)
O3	4e	1	-0.0446(5)	0.7240(9)	0.7099(6)	0.0379(13)
O4	4e	1	-0.1686(5)	0.7311(8)	0.3306(7)	0.0362(12)
O5	4e	1	-0.0772(5)	0.2738(8)	-0.0844(7)	0.0384(12)

Note: $P2_1/n$ is SG Number 14, b-unique, setting 1. Tranformation matrix to $P2_1/c$: [100 0-10 -10-1]. U_{iso} [$Å^2$] is isotropic displacement paramter.

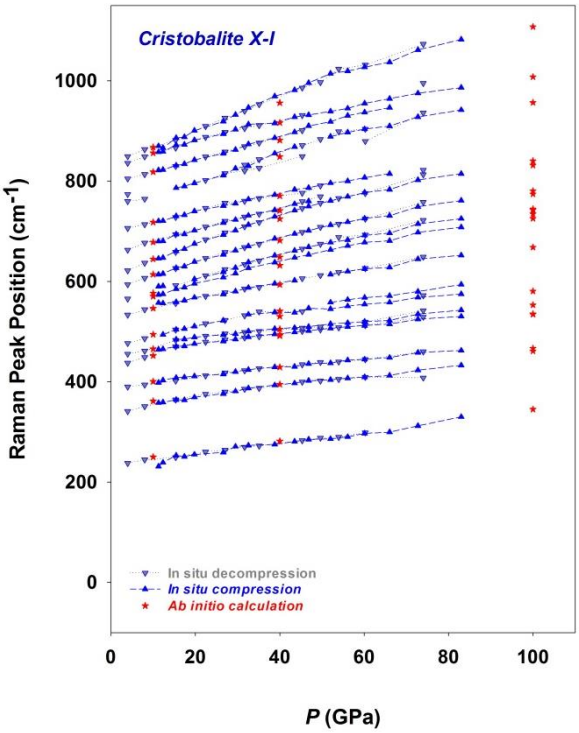

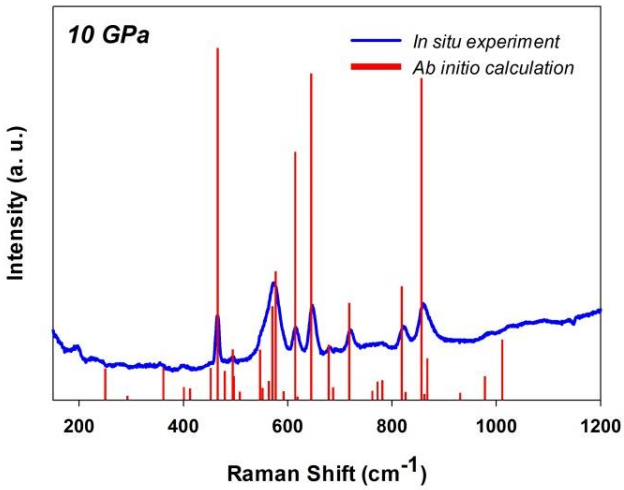

FIGURE 6.5. Pressure dependence of the Raman active modes in cristobalite X-I (left) at ambient temperature obtained experimentally (blue) and theorethically (red). Comparison of the theorethical and experimental spectra for 10 GPa (right).

The polymorph cristobalite X-I found above ~10 GPa in quasi-hydrostatic conditions belongs to the family of high-pressure silica phases comprised of a distorted hexagonal close-packed array of oxygen ions in which silicon atoms fully or partially occupy octahedral sites (Liu et al., 1978, Teter et al., 1998; Dubrovinsky et al., 2004). In the structure of cristobalite X-I, the "3x2 zigzags" of edge-sharing octahedra, theoretically proposed by Teter et al. (1998) and later demonstrated in a $P2_1/c$ post-quartz phase by means of powder XRD analyses (Haines et al., 2001) are formed by fully occupied Si positions. However, the fully-occupied octahedra do not account for the stoichiometric SiO_2: Si1 has the site multiplicity of 2, and Si2 that of 4. The zigzags are surrounded by two half-occupied Si3 octahedra, thereby providing exact stoichiometric ratio. The concept of randomly distributed Si cations over half of the octahedral sites was proposed by Liu et al. (1978) as the modified niccolite structure, but such structure has never been observed by a single-crystal study before. Another unique feature of this structure is the connectivity of the zigzags: the five octahedra in one row (3 fully-occupied surrounded by 2 half-occupied) are joined to the adjacent row by six octahedra distributed in a 2x2x2 pattern. Due to symmetry constraints, only one of the half-occupied positions of this element can be filled, thereby resulting in four (2x2) edge-sharing octahedra, an arrangement never proposed before. Seen in the 010 plane, the structure can be visualized as containing 3x2 zigzag chains separated by one half-occupied

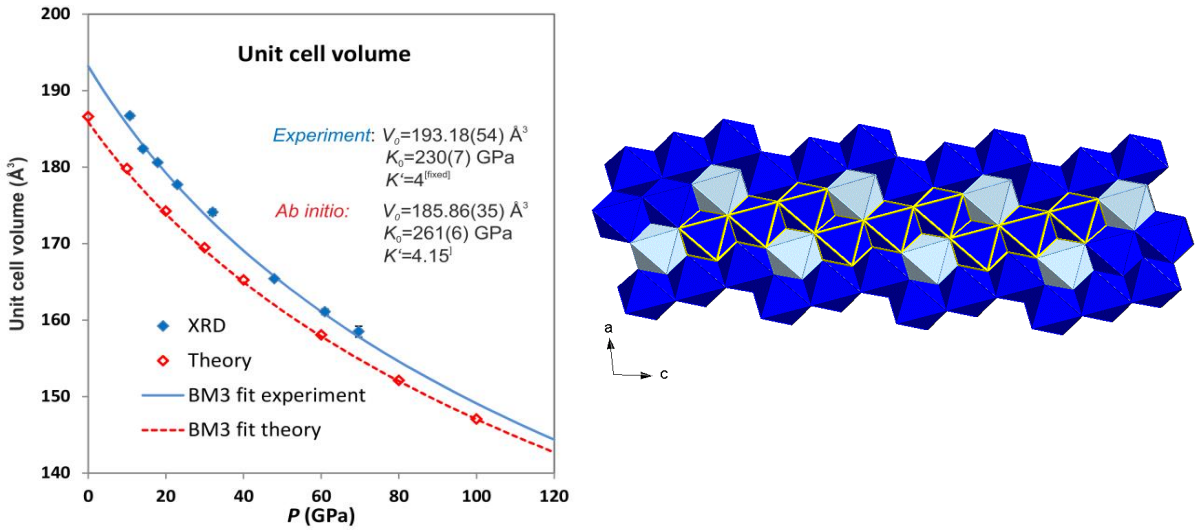

FIGURE 6.6. Structure and compressibility of cristobalite X-I. Birch-Murnaghan Equation of State fitted to the *P-V* data (left) obtained in experiment (blue) and by *ab initio* calculations (red). The structure of cristobalite X-I (right): dark blue are fully occupied octahedra (Si1 and Si2), light blues are half-occupied positions (Si3) and yellow-edged octahedra represent the "3x2 skeleton".

Table 6.4a: Experimental unit-cell parameters of cristobalite X-I at various pressures.

P_{ruby} [GPa]	a [Å]	b [Å]	c [Å]	β [°]	V [Å^3]	R_{int}
10.75(20)	6.664(11)	4.1066(7)	6.894(1)	98.35(5)	186.7(3)	0.05
14.10(10)	6.611(11)	4.0700(14)	6.853(5)	98.40(1)	182.4(3)	0.05
17.91(12)	6.582(1)	4.0443(6)	6.852(9)	98.13(4)	180.6(2)	0.08
22.95(34)	6.580(1)	4.0120(6)	6.802(13)	98.25(5)	177.7(3)	0.06
32.06(53)	6.556(15)	3.9654(8)	6.771(2)	98.16(8)	174.1(4)	-
47.94(10)	6.446(9)	3.8848(5)	6.670(1)	98.01(4)	165.4(2)	0.03
60.95(77)	6.393(1)	3.8371(7)	6.630(11)	98.05(5)	161.1(3)	0.07
69.65(55)	6.400(3)	3.8236(15)	6.527(4)	97.01(2)	158.5(7)	0.04

Note: Numbers in parentheses are the esd's in the last decimal place of each value.

Table 6.4b: Unit-cell parameters of cristobalite X-I obtained by *ab initio* calculations.

P [GPa]	a [Å]	b [Å]	c [Å]	β [°]	V [Bohr^3]	V [Å^3]
0.0	6.6415	4.1035	6.8863	98.0	1259.16	186.59
10.0	6.5808	4.0337	6.8240	98.0	1213.43	179.81
20.0	6.5289	3.9741	6.7684	98.0	1175.95	174.26
30.0	6.4832	3.9222	6.7179	98.0	1143.51	169.45
40.0	6.4419	3.8764	6.6719	98.0	1115.03	165.23
60.0	6.3694	3.7985	6.5898	98.0	1066.58	158.05
80.0	6.3066	3.7341	6.5179	98.0	1026.55	152.12
100.0	6.2509	3.6794	6.4535	98.0	992.47	147.07

Note: Numbers in parentheses are the esd's in the last decimal place of each value.

octahedron, placed between the kinks of the two adjacent chains. The Si3 octahedron is considerably larger in comparison to Si1 and Si2, and has one bond (1.91 Å) and volume V_{oct}=7.4 Å^3 similar to seifertite at ambient conditions. The Si1 and Si2 are more similar to stishovite at relevant pressure in terms of bond lengths and volume.

The theoretical calculations of the Raman spectra were restricted to two extreme fully-occupied Si3 positions, so that the zigzags consisted of rows containing either 1) five and three, or 2) four fully occupied octahedra. In either case the connecting element between the rows contained 2 x 2 fully occupied octahedra. The first arrangement resulted in Raman spectra highly inconsistent with the experimental data, however the spectra computed using the second arrangement show remarkable agreement with experimentally obtained Raman spectra (Fig. 6.5).

The continuous and smooth evolution of the unit cell volume with pressure (Fig. 6.6) can be followed up to 80 GPa. By fitting the experimental *P-V* data with a 3rd-order Birch-Murnaghan equation of state (BM3-EoS), we obtain following room pressure parameters by fixing *K'* to 4: V_0=193.18(51) Å^3, K_0=230(7) GPa. Starting from this value of V_0, we construct the plot of the normalized stress, F_E, vs. Eulerian strain, f_E, (Angel, 2000) from our *P-V* data, and find that it reflects linearity of data consistent with a BM3 fit, yielding comparable values of the bulk modulus, K_0, of about 228 GPa and its pressure derivative *K'* of 4.3.

The *ab initio* calculations result in systematically smaller values of the lattice constants and the unit-cell volumes (Tables 6.4a and b). The volume-offset has the largest value at zero-pressure (ΔV_0=9 Å) and it decreases with pressure. The BM3 fit to the theoretically obtained *P-V* data yield slightly higher K_0=261(6) and *K'*=4.15. Although data of much better quality are required to constrain the compressional behaviour of cristobalite X-I with better accuracy, it is certain that the bulk modulus of this phase is considerably lower than that of any other high-pressure SiO_2 phase containing silicon in octahedral coordination – stishovite (300-310 GPa), $CaCl_2$ (320-330 GPa) or seifertite (320-330 GPa) (summarized in Grocholski et al., 2013). This conforms well to the fact that the structure contains significant amount of partially occupied octahedra. Important to note is that metastable polymorphs are considered extremely difficult in studying their compressional behaviour, because they usually do not have such wide range of existence, thus the X-I phase can be considered exceptional.

The pressure dependence of the Raman modes (*dv/dP*) of cristobalite X-I, where ν is the ambient-pressure phonon frequency and *P* is the pressure, was derived from the data presented in Figure 6.5 and it ranges from 0.9(1)-3.2(1) cm^{-1} /GPa. These values match well with pressure shifts reported for the only two octahedra-based SiO_2 forms studied by Raman spectroscopy, the rutile structured stishovite and its high-pressure, $CaCl_2$-structured polymorph. Based on the zero-pressure bulk

modulus K_0=230(7) GPa determined in this study and using the formulation of the mode-Grüneisen parameter as $\gamma_v=(K_0/\nu)$ (dv/dP), we obtain an average of γ=0.7±0.1. None of the Raman bands is showing softening under pressure, strongly suggesting that cristobalite X-I, although thermodynamically metastable and unquenchable to ambient conditions, can exist in a wide (or even wider than we studied) pressure range.

6.4.3.4 The quenched sample

Raman spectra collected on the samples recovered from the experiments carried out up to variable maximal pressures or compressed at different rates show signature similar to that of the starting α-cristobalite. Given that the Raman spectra of all these products look very similar (Fig. 6.7), we conclude that both slow compression followed by either a rapid quench (Exp1) or slow decompression (Exp4), as well as a rapid compression (exp5) up to only 12 GPa followed by immediate pressure release, resulted in the same product. Samples recovered from Exp1 and Exp4 were investigated by wide-scan synchrotron XRD and both samples give a strong signal of α-cristobalite. Unfortunately, Exp4 was lost during further sample preparation, so we only investigated Exp1 by means of TEM. The sample (Exp1) was recovered after being compressed to ~50 GPa**.** Raman spectra collected during compression in Exp1 are indistinguishable from the spectra obtained in several other compression experiments. At the maximal pressures achieved in all these experiments we always evidenced cristobalite X-I phase as the final compressional product.

TEM foil from the Exp1 sample, prepared by FIB was not equally thinned throughout the sample. Even during the thinning procedure we were able to see internal structural features indicating domains of variable crystallinity. Quenched crystal from the Exp1 is solid and compact, primarily composed of amorphous matrix in which isolated, crystalline clumps of several ~100 nm up to 1 μm in size can be observed (Fig. 6.7). Amorphous matrix has lamellar appearance intersected by layers that are crystalline. We investigated most of the crystallites and all of them can be indexed as α-cristobalite. Representative diffraction patterns are shown in the inset in Figure 6.7. Cristobalite was relatively stable under the electron beam and we did not observe it undergoing amorphization during the exposure to the beam and during acquisition. Most of the cristobalite crystallites are lamellarly twinned, with three distinct lamellae directions. However, most of the crystals in the sample showed similar orientation, indicating that the crystallites had belonged to the same single crystal prior the initial crystalline material underwent amorphization.

Cristobalite X-I is not quenchable and it is believed to partially convert back to α-cristobalite upon pressure-release, however most of the high-pressure phase does not convert into crystalline material but it rather remains amorphous. Another possible interpretation is that the amorphous material formed already under compression and that only a small amount of initial α-cristobalite had transformed to cristobalite X-I. The amorphous matrix might cause broadening of the main Raman bands found on the quenched samples (Fig. 6.7).

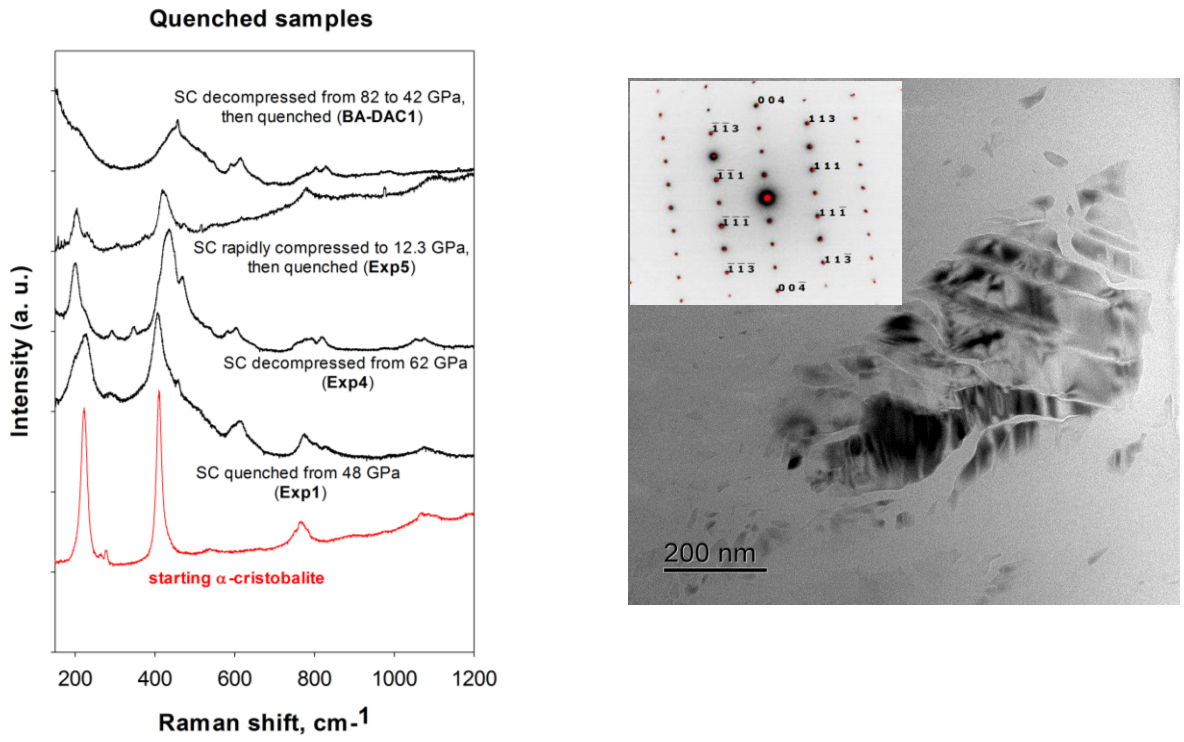

FIGURE 6.7. Representative Raman spectra collected on the single crystals (SC) recovered from various pressures and unde different compressional rates, compared to the starting α-cristobalite (left). Fractured crystalline grain (dark grey to black surrounded by amorphous matrix (right). The inset shows diffraction pattern indexed as α-cristobalite along zone axix [-1 1 0] indicating that the entire grain has the same crystallographic orientation. Black reflections in the inset are from this study whereas the red reflections are simulated electron diffraction spots, starting from the structure reported by Dera et al. 2011 Closed red symbols correspond to allowed reflections; open symbols are the forbidden reflections that appear in SAED due t dynamical diffraction effects.

6.4.4 Non-hydrostatic compression

6.4.4.1 Formation of seifertite

In the experiments on powders, upon compression up to ~50 GPa we find seifertite as the final product. The experiment without pressure medium (Exp6) is a repetition of an earlier experiment (Dubrovinsky et al., 2001; Dubrovinskaia et al., 2001; Prokopenko et al., 2001), that investigated only a non-hydrostatic compression. The experiment on powder surrounded by neon (Exp7) is similar to the one performed earlier by (Yagi and Yamakata, 2000). In agreement with previous studies, in both

experiments on powders with and without the pressure-transmitting medium, we followed the sequence of transitions α->II->X-I by means of *in situ* Raman spectroscopy. Above 20 GPa we lost the signal from the sample and we do not recover it up to the maximum compression (~50 GPa) nor during slow decompression down to pressures very close to ambient. At room pressure we again could see a weak signal, which improved significantly by opening the DAC and exposing the sample to the laser beam directly (Fig. 6.8). Therefore we cannot confirm that cristobalite X-I is the last phase occurring prior formation of seifertite, but as no changes in powder-diffraction pattern of this phase have ever been reported previously prior the transition, it seems justified to assume that no other phases form in this sequence.

6.4.4.2 Quenched seifertite

The sample analyzed by Raman spectroscopy remained stable after 120 seconds exposure to a 1.2 W direct Ar^+ laser beam and was afterwards analyzed by powder XRD and TEM. The collected Raman spectrum of the sample recovered after compression to ~50 GPa is almost identical to the spectrum reported in a similar experiment (Prokopenko et al., 2001) and it is quite close to the theoretically computed spectra of seifertite which could be found in WURM database (Fig. 6.8). There are no apparent similarities between the Raman spectra of seifertite and cristobalite X-I, with the main difference being the strongest mode in seifertite close to 500 cm^{-1}, which is absent in the spectrum of X-I phase.

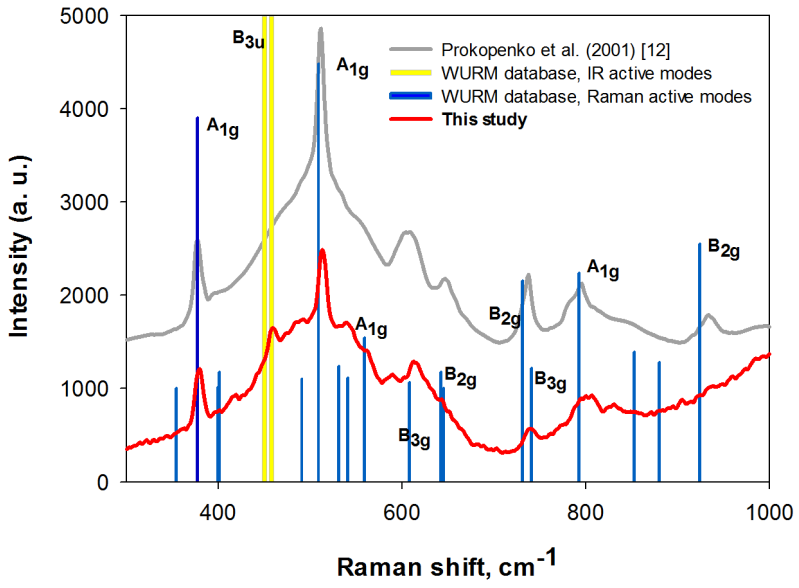

FIGURE 6.8. Raman spectrum of recovered seifertite (red), collected outside diamond anvil cell. Ar^+ laser beam conditions: excitation wavelength 514 nm; power 0.7 W, acquisition 3x120 seconds. For comparison, Raman spectra of experimentally (grey) and computationally (symmetry labeled bulks) obtained seifertite is given.

The sample was afterwards placed on a glass capillary and analyzed using an in-house powder diffractometer. Thus obtained two-dimensional image (Fig. 6.9) contains a halo at d > 4.5 Å, indicating large amounts of amorphous material. The poor crystallinity gives rise to broaden diffraction rings and their weak intensities, so that no proper data integration was possible. But the relative intensities and peak positions show very good agreement with a product of a similar experiment on cristobalite cold-compression (Prokopenko et al., 2001), as well as with seifertite formed at equilibrium conditions (Grocholski et al., 2013). All measured reflections correspond very well to those of seifertite (α-PbO_2 structured silica) and we calculated the orthorhombic unit cell in *P*bcn space group by given peak positions, *hkl* indices and relative intensities (Table 6.5) to be: *a*=4.067(21) Å, *b*=5.090(38) Å, *c*=4.477(14) Å.

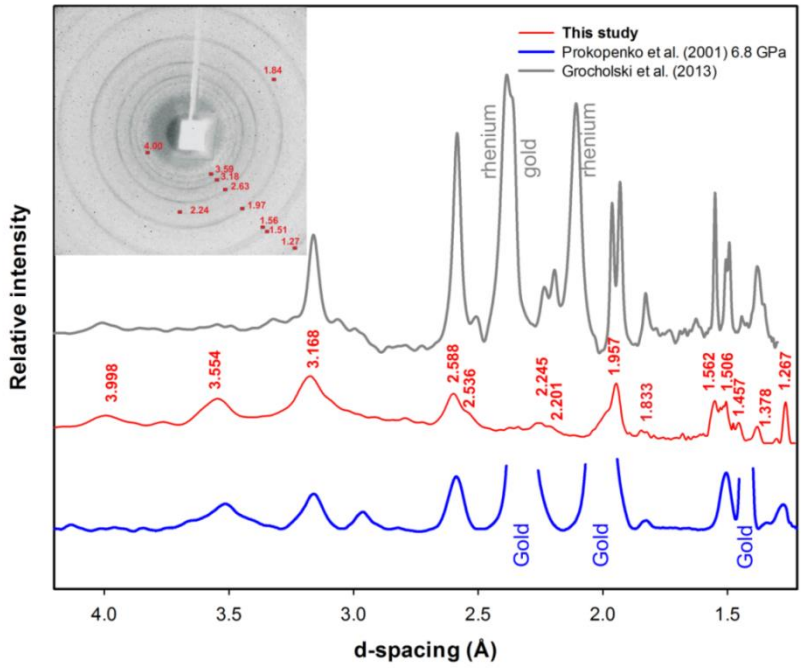

FIGURE 6.9. Powder-diffraction analysis of the sample recovered from 50 GPa, using an in-house diffractometer compared to earlier studies: Prokopenko et al. (2001) compressed cristobalite to ~50 GPa at room temperature and without pressure medium and quenched seifertite; Grocholski et al. (2013) quenched seifertite synthesized at high PT conditions.

At last, the same material determined as seifertite by means of Raman spectroscopy and XRD, was analyzed by TEM. We applied two different methods of sample preparation: 1) we crushed the sample removed from the glass capillary and dispersed it on lacey carbon; 2) we prepared an electron-transparent foil out of the remnant material found inside the gasket using an FIB instrument. Both techniques showed similar outcomes. The analyzed material contained small crystallites (~100 nm) surrounded by amorphous matrix. The crystallites were highly unstable under the beam and became

amorphous instantly during data acquisition, resulting in poor electron diffraction pattern. We performed the analyses by alternating between a direct SAED (large surface, lower beam current, longer exposure) and a High Resolution TEM mode (more selective, high beam current, shorter acquisition time), in order to collect diverse information of the material. From the diffraction measurements in HRTEM mode on isolated grains we derived FFT (Fast Fourier Transform) diffraction images. The *d*-spacings we obtain by FFT can be interpreted as reflections of seifertite, however the indexing agrees with the α-cristobalite unit cell even better than with the cell of seifertite (Fig. 6.10). We suspect that the beam could cause short-range

Table 6.5: XRD and TEM reflections of quenched seifertite

Our study			Seifertite (El Goresy et al. 2008)		hkl (*Pbcn*)
XRD d [Å]	I/I_0	HRTEM d [Å]	d [Å]	I/I_0	
4.004	20				
3.558	40				
3.176	76		3.1807	70	110
2.96	13	2.94			
2.785	7				
2.395	4				
2.597	63	2.58	2.5963	67	111
		2.51	2.5231	11	020
2.249	21	2.29	2.2473	12	002
			2.2001	10	021
2.026	27		2.0485	2.5	200
1.954	100		1.9703	65	102
			1.9383	66	121
1.843	13		1.8354	13	112
			1.7485	2	211
1.677	7		1.6782	4	022
1.59	1		1.5903	4	220
1.557	68		1.556	33	130
1.515	58		1.5139	81	202
			1.4993	69	221
1.47	1		1.4704	1	131
1.439	1		1.3554	17	113
			1.2982	2	
1.27	70		1.2882	100	

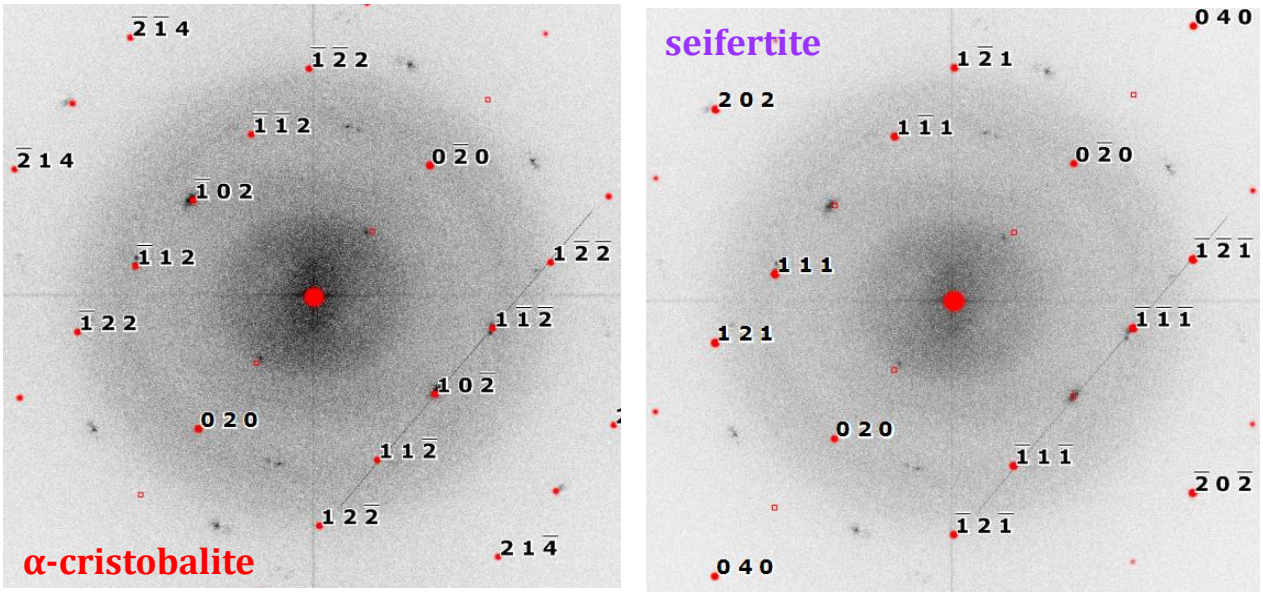

FIGURE 6.10. FFT (Fast Fourier Transform) diffraction pattern derived from HRTEM images of isolated grains within th EXP6 powder sample. The *d*-spacings we obtain by FFT can be indexed by cristobalite and seifertite, in this particula direction. Due to the instability under the beam, only one orientation of the specimen was acquired.

transformation of highly unstable seifertite to more stable cristobalite, before the entire material becomes amorphous. To obtain good diffraction pattern of this material was difficult due to the small particle size and its relatively high beam sensitivity compared to the quenched cristobalite of EXP1 (Fig. 6.7). This beam sensitivity is interpreted as a result of poor crystallinity. Following the interpretation by Biskupek and Kaiser (2004), we find our maximal Δd/d error of 6.3% for the (110_{seif}) acceptable, given the small size of the grain, extraordinary instability of the sample under the beam as well as the fact that the sample is not a compact but rather loose powder. We eliminated the possibility of ruby, graphite, diamond and stishovite by EDS and indexing trials. The indexing of diffraction patterns seemed more efficient and less erroneous when direct SAED measurements were performed. Due to destruction of material, direct diffraction was rarely possible. In one such measurement we were able to index only cristobalite and no seifertite, however, we cannot conclude based on this sole example that seifertite is completely absent from the sample.

6.5 Conclusions and Implications

Cristobalite was often documented in the meteorites that lack any high-pressure silica polymorphs (e.g. Weber et al., 2000; Leroux and Cordier, 2006), albeit the rest of the mineral record indicates peak shock pressures exceeding 10 GPa, at which at least coesite or stishovite are expected to form and be preserved. Most of cristobalite in shocked materials is believed to form after pressure release due to high post-impact temperatures, but here we propose that it can form as a product of X-I phase back-transformation. Understanding the pressure-induced transition sequence of cristobalite, capacity of the cristobalite X-I structure to "hold" under pressure, as well as taking into account its stability at slightly elevated temperatures (Dubrovinsky et al., 2001), there is a great possibility that this phase can be accommodated in (quasi)-hydrostatic environment where temperature is not sufficient to form stishovite, removing all its high-pressure signature once the pressure is released and it back-transforms to the α-form. The reconstructive transition that involves increase in coordination number of silicon from four in (α- or II) cristobalite to its six-fold coordinated polymorph X-I does not require any thermal activation; however the high-pressure polymorph cannot be preserved at ambient conditions.

Cristobalite was documented alongside all the natural occurrences of the high-pressure, post-stishovite silica polymorph seifertite (e.g. Miyahara et al., 2013; Bläß, 2013), related to the heavily shocked Martian or Lunar meteorites. As shown in our experiments, also in a non-hydrostatic environment cristobalite follows α -> II -> X-I transformation path, but if the pressures are

sufficiently high (~37-40 GPa according to (Dubrovinsky et al., 2001; Tsuchida and Yagi, 1990; Yagi and Yamakata, 2000) it will eventually transform quenchable seifertite, bypassing the equilibrium formation of stishovite and $CaCl_2$ structured polymorph. Although the burning question - what is the lowest pressure and temperature at which seifertite can form - remains unclear, an ever growing number of evidences speaks in favor of seifertite formation far below its thermodynamic stability. To this adds our finding that 4-to-6 increase in coordination number of silicon in cristobalite occurs as low as ~10 GPa without requiring substantial heating, and can be followed by seifertite formation at highest of about ~50 GPa in a non-hydrostatic environment. This leads us to the conclusion that the transformation path via the X-I phase is a scenario of seifertite formation more likely to occur in nature than via its equilibrium, supported by the argument that seifertite-cristobalite parageneses is commonly observed in in shocked meteorites. This, in turn, raises the question whether any of the natural seifertite occurrences represents a formation at equilibrium conditions.

Based on our observation, we conclude that particularly in quasi-hydrostatic or non-hydrostatic conditions cristobalite may occur on decompression path after and could not, therefore, be used as a proof of the absence of high-pressures. Neither cristobalite nor seifertite should be considered reliable tracers of the peak shock conditions. Keeping in mind the similarity in structures of cristobalite X-I and seifertite, we conclude that if there were any phases intermediating the two polymorphs, then they are formed by a simple rearrangement of the octahedra within the chains. Cristobalite X-I has a structure most similar to that of seifertite (containing kinked chains of octahedra) ever studied in terms of precise single-crystal analysis and determination of exact atomic positions. To our knowledge, single crystals of seifertite have never been produced. Given a relatively simple experimental procedures for the X-I-> seifertite transition, it seems justified to propose similar experimental procedure in order to investigate single-crystal properties of seifertite in the future.

6.6 Acknowledgements

This work was made possible by the support of the University of Bayreuth Graduate School, as well by the stipend provided by the Women´s representative & Equal Opportunities Department of the University of Bayreuth, to whom A.Č. is truly grateful. Hubert Schulze and Raphael Njul are gratefully acknowledged for the sample preparation, Andreas Audétat for helping us analyze the starting material using LA-ICP-MS and Tiziana Boffa Ballaran for the productive discussions and help in data analysis. Portions of this research were carried out at the light source PETRA III at DESY, Helmholz group, as well as at the European Synchrotron Radiation Facility (ESRF).

7. BIBLIOGRAPHY

Akaogi, M., Yusa, H., Shiraishi, K., Suzuki, T., 1995. Thermodynamic properties of α-quartz, coesite, and stishovite and equilibrium phase relations at high pressures and high temperatures. J. Geophys. Res. 100, 22337. doi:10.1029/95JB02395

Andrault, D., Angel, R.J., Mosenfelder, J.L., Le Bihan, T., 2003. Equation of State of Stishovite to Lower Mantle Pressures. Am. Mineral. 88, 301–307.

Andrault, D., Fiquet, G., Guyot, F., Hanfland, M., 1998. Pressure-Induced Landau-Type Transition in Stishovite. Science 282, 720 –724. doi:10.1126/science.282.5389.720

Angel, R.J., 2000. Equations of State. In Hazen, RM, Downs, RT (Eds.), in: High-Pressure, High-Temperature Crystal Chemistry, Reviews in Mineralogy and Geochemistry. pp. 35–60.

Angel, R.J., Bujak, M., Zhao, J., Gatta, G.D., Jacobsen, S.D., 2007. Effective hydrostatic limits of pressure media for high-pressure crystallographic studies. J. Appl. Crystallogr. 40, 26–32. doi:10.1107/S0021889806045523

Angel, R.J., Jackson, J.M., 2002. Elasticity and equation of state of orthoenstatite, MgSiO3. Am. Mineral. 87, 558–561.

Angel, R.J., Ross, N.L., Seifert, F., Fliervoet, T.F., 1996. Structural characterization of pentacoordinate silicon in a calcium silicate. Nature 384, 441–444. doi:10.1038/384441a0

Angel, R.J., Shaw, C.S.J., Gibbs, G.V., 2003. Compression mechanisms of coesite. Phys. Chem. Miner. 30, 167–176. doi:10.1007/s00269-003-0303-9

Angel, R.., Mosenfelder, J.., Shaw, C.S.., 2001. Anomalous compression and equation of state of coesite. Phys. Earth Planet. Inter. 124, 71–79. doi:10.1016/S0031-9201(01)00184-4

Araki, T., Zoltai, T., 1969. Refinement of a Coesite Structure. Z. Krist. Krist. Krist. Krist. 129, 381–&. doi:10.1524/zkri.1969.129.5-6.381

Asahara, Y., Hirose, K., Ohishi, Y., Hirao, N., Ozawa, H., Murakami, M., 2013. Acoustic velocity measurements for stishovite across the post-stishovite phase transition under deviatoric stress: Implications for the seismic features of subducting slabs in the mid-mantle. Am. Mineral. 98, 2053–2062. doi:10.2138/am.2013.4145

Audétat, A., Garbe-Schönberg, D., Kronz, A., Pettke, T., Rusk, B., Donovan, J.J., Lowers, H.A., 2014. Characterisation of a Natural Quartz Crystal as a Reference Material for Microanalytical Determination of Ti, Al, Li, Fe, Mn, Ga and Ge. Geostand. Geoanalytical Res. n/a–n/a. doi:10.1111/j.1751-908X.2014.00309.x

Badro, J., Teter, D.M., Downs, R.T., Gillet, P., Hemley, R.J., Barrat, J.-L., 1997. Theoretical study of a five-coordinated silica polymorph. Phys. Rev. B 56, 5797–5806. doi:10.1103/PhysRevB.56.5797

Baroni, S., de Gironcoli, S., dal Corso, A., Giannozzi, P., 2001. Phonons and related crystal properties from density-functional perturbation theory. Rev. Mod. Phys. 73, 515–562. doi:10.1103/RevModPhys.73.515

Bartelmehs, Boisen, Gibbs, and Downs 2002et al. PROGRAM METRIC Ver. 6.1**, Science 172 (1971) 567-570.

Bassett, W.A., 2009. Diamond anvil cell, 50th birthday. High Press. Res. 29, 163–186. doi:10.1080/08957950802597239

Bläß, U.W., 2013. Shock-induced formation mechanism of seifertite in shergottites. Phys. Chem. Miner. 40, 425–437. doi:10.1007/s00269-013-0580-x

Boehler, R., De Hantsetters, K., 2004. New anvil designs in diamond-cells. High Press. Res. 24, 391–396. doi:10.1080/08957950412331323924

Boyer, H., Smith, D.C., Chopin, C., Lasnier, B., 1985. Raman microprobe (RMP) determinations of natural and synthetic coesite. Phys. Chem. Miner. 12, 45–48. doi:10.1007/BF00348746

Bragg, S.W.L., 1937. Atomic Structure of Minerals. Cornell University Press.

Bragg, W., Gibbs, R.E., 1925. The Structure of $ \alpha $ and $ \beta $ Quartz. Proc. R. Soc. Lond. Math. Phys. Eng. Sci. 109, 405–427. doi:10.1098/rspa.1925.0135

Bragg, W.H., Bragg, W.L., 1913. The Reflection of X-rays by Crystals. Proc. R. Soc. Lond. Math. Phys. Eng. Sci. 88, 428–438. doi:10.1098/rspa.1913.0040

Brearley, A.J., Jones, R.H., 1998. Chondritic meteorites. Rev. Mineral. Geochem. 36, 3.1–3.398.

Bromiley, G.D., Keppler, H., 2004. An experimental investigation of hydroxyl solubility in jadeite and Na-rich clinopyroxenes. Contrib. Mineral. Petrol. 147, 189–200. doi:10.1007/s00410-003-0551-1

Buerger, M.J. and Zoltai, T. (1959) Crystal structure of coesite, the high density form of silica. Zeitschrift fuer Kristallographie, Kristallgeometrie, Kristallphysik, Kristallchemie, 111, 129-141.

Caracas, R., Bobocioiu, E., 2011. The WURM project-a freely available web-based repository of computed physical data for minerals. Am. Mineral. 96, 437–443. doi:10.2138/am.2011.3532

Černok, A., Ballaran, T.B., Caracas, R., Miyajima, N., Bykova, E., Prakapenka, V., Liermann, H.-P., Dubrovinsky, L., 2014. Pressure-induced phase transitions in coesite. Am. Mineral. 99, 755–763. doi:10.2138/am.2014.4585

Chao, E.C.T., Shoemaker, E.M., Madsen, B.M., 1960. First Natural Occurrence of Coesite. Science 132, 220–222. doi:10.1126/science.132.3421.220

Chen, T., Gwanmesia, G.D., Wang, X., Zou, Y., Liebermann, R.C., Michaut, C., Li, B., 2015. Anomalous elastic properties of coesite at high pressure and implications for the upper mantle X-discontinuity. Earth Planet. Sci. Lett. 412, 42–51. doi:10.1016/j.epsl.2014.12.025

Chen, Ming, Wansheng Xiao, and Xiande Xie. 2010. "Coesite and Quartz Characteristic of Crystallization from Shock-Produced Silica Melt in the Xiuyan Crater." Earth and Planetary Science Letters 297, 306–14. doi:10.1016/j.epsl.2010.06.032

Chervin, J., B. Canny, and M. Mancinelli (2003), Erratum: "ruby-spheres as pressure gauge for optically transparent high pressure cells," High Pressure Research 23, 493.

Chijioke, A.D., Nellis, W.J., Soldatov, A., Silvera, I.F., 2005. The ruby pressure standard to 150 GPa. J. Appl. Phys. 98, 4905. doi:10.1063/1.2135877

Chopin, C., 1984. Coesite and pure pyrope in high-grade blueschists of the Western Alps: a first record and some consequences. Contrib. Mineral. Petrol. 86, 107–118. doi:10.1007/BF00381838

Coes, L., 1953. A New Dense Crystalline Silica. Science 118, 131–132. doi:10.1126/science.118.3057.131

Dera P. HPCAT/CDAC Short Course Script "Synchrotron High-pressure Techniques", Argonne, IL, September 16, 2010.

Dera, P., Lazarz, J.D., Prakapenka, V.B., Barkley, M., Downs, R.T., 2011. New insights into the high-pressure polymorphism of SiO2 cristobalite. Phys. Chem. Miner. 38, 517–529. doi:10.1007/s00269-011-0424-5

Dewaele, A., Datchi, F., Loubeyre, P., Mezouar, M., 2008. High pressure-high temperature equations of state of neon and diamond. Phys. Rev. B 77. doi:10.1103/PhysRevB.77.094106

Dewaele, A., Loubeyre, P., Mezouar, M., 2004. Equations of state of six metals above 94 GPa. Phys. Rev. B 70, 094112. doi:10.1103/PhysRevB.70.094112

Dmitriev, V., Tolédano, P., Torgashev, V., Salje, E., 1998. Theory of reconstructive phase transitions between SiO2 polymorphs. Phys. Rev. B 58, 11911–11921. doi:10.1103/PhysRevB.58.11911

Donadio, D., Martoňák, R., Raiteri, P., Parrinello, M., 2008. Influence of Temperature and Anisotropic Pressure on the Phase Transitions in $$\alpha${}$-Cristobalite. Phys. Rev. Lett. 100, 165502. doi:10.1103/PhysRevLett.100.165502

Dove, M.T., Craig, M.S., Keen, D.A., Marshall, W.G., Redfern, S. a. T., Trachenko, K.O., Tucker, M.G., 2000. Crystal structure of the high-pressure monoclinic phase-II of cristobalite, SiO2. Mineral. Mag. 64, 569–576. doi:10.1180/002646100549436

Downs, R., Palmer, D., 1994. The Pressure Behavior of Alpha-Cristobalite. Am. Mineral. 79, 9–14.

Driver, K.P., Cohen, R.E., Wu, Z., Militzer, B., Ríos, P.L., Towler, M.D., Needs, R.J., Wilkins, J.W., 2010. Quantum Monte Carlo computations of phase stability, equations of state, and elasticity of high-pressure silica. Proc. Natl. Acad. Sci. 107, 9519–9524. doi:10.1073/pnas.0912130107

Dubrovinskaia, N.A., Dubrovinsky, L.S., Saxena, S.K., Tutti, F., Rekhi, S., Le Bihan, T., 2001. Direct transition from cristobalite to post-stishovite alpha-PbO2-like silica phase. Eur. J. Mineral. 13, 479–483. doi:10.1127/0935-1221/2001/0013-0479

Dubrovinskaia, N., Dubrovinsky, L., 2003. Whole-cell heater for the diamond anvil cell. Rev. Sci. Instrum. 74, 3433–3437. doi:10.1063/1.1578151

Dubrovinsky, L.., Dubrovinskaia, N.., Prakapenka, V., Seifert, F., Langenhorst, F., Dmitriev, V., Weber, H.-P., Le Bihan, T., 2004. A class of new high-pressure silica polymorphs. Phys. Earth Planet. Inter. 143–144, 231–240. doi:10.1016/j.pepi.2003.06.006

Dubrovinsky, L.., Dubrovinskaia, N.., Saxena, S.., Tutti, F., Rekhi, S., Le Bihan, T., Shen, G., Hu, J., 2001. Pressure-induced transformations of cristobalite. Chem. Phys. Lett. 333, 264–270. doi:10.1016/S0009-2614(00)01147-7

Dubrovinsky, L.S., Belonoshko, A.B., 1996. Pressure-induced phase transition and structural changes under deviatoric stress of stishovite to CaCl2-like structure. Geochim. Cosmochim. Acta 60, 3657–3663. doi:10.1016/0016-7037(96)00194-9

Dubrovinsky, L.S., Saxena, S.K., Lazor, P., Ahuja, R., Eriksson, O., Wills, J.M., Johansson, B., 1997. Experimental and theoretical identification of a new high-pressure phase of silica. Nature 388, 362–365. doi:10.1038/41066

Eloïse Gaillou, E.F., 2008. Common gem opal: An investigation of micro-to nano-structure. Am. Mineral. 93, 1865–1873. doi:10.2138/am.2008.2518

Fanderlik, I., 1991. Silica glass and its application. Elsevier.

Farrugia, L.J., 1999. *WinGX* suite for small-molecule single-crystal crystallography. J. Appl. Crystallogr. 32, 837–838. doi:10.1107/S0021889899006020

Fei, Y., Ricolleau, A., Frank, M., Mibe, K., Shen, G., Prakapenka, V., 2007. Toward an internally consistent pressure scale. Proc. Natl. Acad. Sci. 104, 9182–9186. doi:10.1073/pnas.0609013104

Ferriere, L., Koeberl, C., Reimold, W.U., 2009. Characterisation of ballen quartz and cristobalite in impact breccias : new observations and constraints on ballen formation. Eur. J. Mineral. 21, 203–217.

Finger, L.W., Hazen, R.M., 2000. Systematics of High-Pressure Silicate Structures. Rev. Mineral. Geochem. 41, 123–155. doi:10.2138/rmg.2000.41.5

Finger, L.W., Hazen, R.M., 1991. Crystal chemistry of six-coordinated silicon: a key to understanding the earth's deep interior. Acta Crystallogr. Sect. B 47, 561–580. doi:10.1107/S0108768191004214

Gibbs, G.V., Boisen, M.B., Rosso, K.M., Teter, D.M., Bukowinski, M.S.T., 2000. Model structures and electron density distributions for the silica polymorph coesite at pressure: An assessment of OO bonded interactions. J. Phys. Chem. B 104, 10534–10542. doi:10.1021/jp002113a

Gibbs G.V, Meagher E.P, Newton M.D. Swanson D.K. 1981. A comparison of experimental and theoretical bond length and angle variations for minerals, inorganic solids, and molecules. In O'Keeffe M.,Navrotsky A, Eds. Structure and Bonding in Crystals, Vol. 1. 195-225. Academic Press, New York.

Gibbs, G.V., Downs, J.W., Boisen, M.B., 1994. The elusive SiO bond. Rev. Mineral. Geochem. 29, 331–368.

Gibbs, G.V.;Prewitt, C.T.;Baldwin, K.J. (1977) A study of the structural chemistry of coesite. Zeitschrift fuer Kristallographie, Kristallgeometrie, Kristallphysik, Kristallchemie, 145, 108-123.

Gibbs, G.V., Wallace, A.F., Cox, D.F., Downs, R.T., Ross, N.L., Rosso, K.M., 2009. Bonded interactions in silica polymorphs, silicates, and siloxane molecules. Am. Mineral. 94, 1085–1102. doi:10.2138/am.2009.3215

Gillet, P., 1996. Raman spectroscopy at high pressure and high temperature. Phase transitions and thermodynamic properties of minerals. Physics and Chemistry of Minerals 23, 263-

Glinnemann, J., King, H., Schulz, H., Hahn, T., Laplaca, S., Dacol, F., 1992. Crystal-Structures of the Low-Temperature Quartz-Type Phases of Sio2 and Geo2 at Elevated Pressure. Z. Krist. 198, 177–212. doi:10.1524/zkri.1992.198.3-4.177

Goncharov, A., 2012. Raman Spectroscopy at High Pressures. International Journal of Spectroscopy 2012.

Gonze, X., Rignanese, G.-M., and Caracas, R. (2005) First-principles studies of the lattice dynamics of crystals, and related properties. Zeitschrift für Kristallographie, 220, 458–472.

Gonze, X., Amadon, B., Anglade, P.-M., Beuken, J.-M., Bottin, F., Boulanger, P., Bruneval, F., Caliste, D., Caracas, R., Côté, M., Deutsch, T., Genovese, L., Ghosez, P., Giantomassi, M., Goedecker, S., Hamann, D.R., Hermet, P., Jollet, F., Jomard, G., Leroux, S., Mancini, M., Mazevet, S., Oliveira, M.J.T., Onida, G., Pouillon, Y., Rangel, T., Rignanese, G.-M., Sangalli, D., Shaltaf, R., Torrent, M., Verstraete, M.J., Zerah, G., Zwanziger, J.W., 2009. ABINIT: First-principles approach to material and nanosystem properties. Comput. Phys. Commun., 40 YEARS OF CPC: A celebratory issue focused on quality software for high performance, grid and novel computing architectures 180, 2582–2615. doi:10.1016/j.cpc.2009.07.007

Gonze, X., Beuken, J.-M., Caracas, R., Detraux, F., Fuchs, M., Rignanese, G.-M., Sindic, L., Verstraete, M., Zerah, G., Jollet, F., Torrent, M., Roy, A., Mikami, M., Ghosez, P., Raty, J.-Y., Allan, D.C., 2002. First-principles computation of material properties: the ABINIT software project. Comput. Mater. Sci. 25, 478–492. doi:10.1016/S0927-0256(02)00325-7

Goresy, A.E., Dera, P., Sharp, T.G., Prewitt, C.T., Chen, M., Dubrovinsky, L., Wopenka, B., Boctor, N.Z., Hemley, R.J., 2008. Seifertite, a dense orthorhombic polymorph of silica from the Martian meteorites Shergotty and Zagami. Eur. J. Mineral. 20, 523–528. doi:10.1127/0935-1221/2008/0020-1812

Grocholski, B., Shim, S.-H., Prakapenka, V.B., 2013. Stability, metastability, and elastic properties of a dense silica polymorph, seifertite. J. Geophys. Res. Solid Earth 118, 4745–4757. doi:10.1002/jgrb.50360

Haines, J., Léger, J.M., Gorelli, F., Hanfland, M., 2001. Crystalline Post-Quartz Phase in Silica at High Pressure. Phys. Rev. Lett. 87, 155503. doi:10.1103/PhysRevLett.87.155503

Hazen, R., Finger, L., Hemley, R., Mao, H., 1989. High-Pressure Crystal-Chemistry and Amorphization of Alpha-Quartz. Solid State Commun. 72, 507–511. doi:10.1016/0038-1098(89)90607-8

Heaney, P.J., 1994. Structure and chemistry of the low-pressure silica polymorphs. Rev. Mineral. Geochem. 29, 1–40.

Heinz, D.L, and Jeanloz, R. (1984) The equation of state of the gold calibration standard. Journal of Applied Physics, 55, 885-893.

Hemley, R.J., 1987. Pressure Dependence of Raman Spectra of SiO2 Polymorphs: α-Quartz, Coesite, and Stishovite, in: H.nghnani, M., Syono, Y. (Eds.), High-Pressure Research in Mineral Physics: A Volume in Honor of Syun-Iti Akimoto. American Geophysical Union, pp. 347–359.

R. J. Hemley, C. S. Zha. "X-Ray Diffraction and Equation of State of Solid Neon to 110 GPa." Physical Review. B, Condensed Matter 39, no. 16 (1989): 11820–27. doi:10.1103/PhysRevB.39.11820.

Hemley, R.J., Prewitt, C.T., Kingma, K.J., 1994. High-pressure behavior of silica. Rev. Mineral. Geochem. 29, 41–81.

Horwell, C.J., Williamson, B.J., Donaldson, K., Le Blond, J.S., Damby, D.E., Bowen, L., 2012. The structure of volcanic cristobalite in relation to its toxicity; relevance for the variable crystalline silica hazard. Part. Fibre Toxicol. 9, 44. doi:10.1186/1743-8977-9-44

Huang, L., Durandurdu, M., Kieffer, J., 2006. Transformation pathways of silica under high pressure. Nat. Mater. 5, 977–981. doi:10.1038/nmat1760

Ikuta, D., Kawame, N., Banno, S., Hirajima, T., Ito, K., Rakovan, J.F., Downs, R.T., Tamada, O., 2007. First in situ X-ray identification of coesite and retrograde quartz on a glass thin section of an ultrahigh-pressure metamorphic rock and their crystal structure details. Am. Mineral. 92, 57–63. doi:10.2138/am.2007.2228

Irifune, T., Ringwood, A., Hibberson, W., 1994. Subduction of Continental-Crust and Terrigenous and Pelagic Sediments -. Earth Planet. Sci. Lett. 126, 351–368. doi:10.1016/0012-821X(94)90117-1

Jacobsen, S.D., Holl, C.M., Adams, K.A., Fischer, R.A., Martin, E.S., Bina, C.R., Lin, J.-F., Prakapenka, V.B., Kubo, A., Dera, P., 2008. Compression of single-crystal magnesium oxide to 118 GPa and a ruby pressure gauge for helium pressure media. Am. Mineral. 93, 1823–1828. doi:10.2138/am.2008.2988

Jatkar, K., Jyengar, B.: Indian J. Phys., 23 (1949), 4, p. 145-152.

Johannes W. (1973). A simplified piston-cylinder apparatus of high precision. Neues Jahrbuch für Mineralogie, Monatshefte, 337-351.

Kantor, I., Prakapenka, V., Kantor, A., Dera, P., Kurnosov, A., Sinogeikin, S., Dubrovinskaia, N., Dubrovinsky, L., 2012. BX90: A new diamond anvil cell design for X-ray diffraction and optical measurements. Rev. Sci. Instrum. 83. doi:10.1063/1.4768541

Kato, N.I., 2004. Reducing focused ion beam damage to transmission electron microscopy samples. J. Electron Microsc. (Tokyo) 53, 451–458. doi:10.1093/jmicro/dfh080

Keppler H.and Frost D. J., 2005. Introduction to minerals under extreme conditions. In R. Miletich, (Ed.): Mineral Behaviour at Extreme Conditions/EMU Notes in Mineralogy, Vol. 7, Chapter 1, p. 1–30. Eötvös University Press, Budapest.

Kihara, K., Hirose, T., Shinoda, K., 2005. Raman spectra, normal modes and disorder in monoclinic tridymite and its higher temperature orthorhombic modification. J. Mineral. Petrol. Sci. 100, 91–103. doi:10.2465/jmps.100.91

Kim-Zajonz, J., Werner, S., Schulz, H., 1999. High pressure single crystal X-ray diffraction study on alpha-quartz. Z. Krist. 214, 324–330. doi:10.1524/zkri.1999.214.6.324

Kingma, K.J., Hemley, R.J., Mao, H., Veblen, D.R., 1993. New high-pressure transformation in α-quartz. Phys. Rev. Lett. 70, 3927–3930. doi:10.1103/PhysRevLett.70.3927

Klotz, S., Chervin, J.-C., Munsch, P., Le Marchand, G., 2009. Hydrostatic limits of 11 pressure transmitting media. J. Phys. -Appl. Phys. 42. doi:10.1088/0022-3727/42/7/075413

Koch-Muller, M., Fei, Y., Hauri, E., Liu, Z., 2001. Location and quantitative analysis of OH in coesite. Phys. Chem. Miner. 28, 693–705. doi:10.1007/s002690100195

Kohn, W., Sham, L.J., 1965. Self-Consistent Equations Including Exchange and Correlation Effects. Phys. Rev. 140, A1133–A1138. doi:10.1103/PhysRev.140.A1133

Koike, C., Noguchi, R., Chihara, H., Suto, H., Ohtaka, O., Imai, Y., Matsumoto, T., Tsuchiyama, A., 2013. Infrared Spectra of Silica Polymorphs and the Conditions of Their Formation. Astrophys. J. 778, 60. doi:10.1088/0004-637X/778/1/60

Korsakov, A.V., Hutsebaut, D., Theunissen, K., Vandenabeele, P., Stepanov, A.S., 2007. Raman mapping of coesite inclusions in garnet from the Kokchetav Massif (Northern Kazakhstan). Spectrochim. Acta. A. Mol. Biomol. Spectrosc. 68, 1046–1052. doi:10.1016/j.saa.2007.04.005

Kurnosov, A., Kantor, I., Boffa-Ballaran, T., Lindhardt, S., Dubrovinsky, L., Kuznetsov, A., Zehnder, B.H., 2008. A novel gas-loading system for mechanically closing of various types of diamond anvil cells. Rev. Sci. Instrum. 79. doi:10.1063/1.2902506

Kuwayama, Y., Hirose, K., Sata, N., Ohishi, Y., 2005. The Pyrite-Type High-Pressure Form of Silica. Science 309, 923 –925. doi:10.1126/science.1114879

Lakatos, B. Bohus, J. Medgyesi, G.J. Acta Chim. Acad. Sei. Hung., 20 (1959), 1, p. 2-52

Leroux, H., Cordier, P., 2006. Magmatic cristobalite and quartz in the NWA 856 Martian meteorite. Meteorit. Planet. Sci. 41, 913–923. doi:10.1111/j.1945-5100.2006.tb00495.x

Levien, L., Prewitt, C., 1981. High-Pressure Crystal-Structure and Compressibility of Coesite. Am. Mineral. 66, 324–333.

Levien, L., Prewitt, C., Weidner, D., 1980. Structure and Elastic Properties of Quartz at Pressure. Am. Mineral. 65, 920–930.

Liu, L.-G., Bassett, W.A., Sharry, J., 1978. New high-pressure modifications of GeO2 and SiO2. J. Geophys. Res. Solid Earth 83, 2301–2305. doi:10.1029/JB083iB05p02301

Luo, S.-N., Tschauner, O., Asimow, P.D., Ahrens, T.J., 2005. A new dense silica polymorph: A possible link between tetrahedrally and octahedrally coordinated silica. Am. Mineral. 89, 455 –461.

Mao. H. K., Bell P. M., Shaner J., and Steinberg D. 1979. Specific volume measurements of Cu, Mo, Pd, and Ag and calibration of the ruby R1 fluorescencc pressure gauge from 0.06 to 1 Mbar. Journal of Applied Physics 49, 3276-3283.

Mao, H., Xu, J., Bell, P., 1986. Calibration of the Ruby Pressure Gauge to 800-Kbar Under Quasi-Hydrostatic Conditions. J. Geophys. Res.-Solid Earth Planets 91, 4673–4676. doi:10.1029/JB091iB05p04673

Mao H.K. & Hemley R.J. 1998. New windows on the Earth's deep interior. In Hemley, R. J. (Ed.): Ultrahigh-pressure mineralogy: Physics and chemistry of the Earth's deep interior/ Reviews in Mineralogy, Vol. 37. pp. 1-32. Mineralogical Society of America, Washington D.C.

Martin, R.M., 2004. Electronic Structure: Basic Theory and Practical Methods. Cambridge University Press.

Martoňák, R., Donadio, D., Oganov, A.R., Parrinello, M., 2007. From four- to six-coordinated silica: Transformation pathways from metadynamics. Phys. Rev. B 76, 014120. doi:10.1103/PhysRevB.76.014120

McDonough, W.F., 2001. Chapter 1 The composition of the earth, in: Roman Teisseyre and Eugeniusz Majewski (Ed.), International Geophysics, Earthquake Thermodynamics and Phase Transformations in the Earth's Interior. Academic Press, pp. 3–23.

McDonough, W.F., Sun, S. 1995. The composition of the Earth. Chem. Geol. 120, 223–253. doi:10.1016/0009-2541(94)00140-4

Miletich, Ronald, David R. Allan, and Werner F. Kuhs. 2000. High-Pressure Single-Crystal Techniques. In R. Hazen and R. T. Downs, Eds., High-Temperature and High-Pressure Crystal Chemistry, Reviews Reviews in Mineralogy and Geochemistry 41 (1): 445–519. doi:10.2138/rmg.2000.41.14

Mitra. S. 2004. High Pressure Geochemistry & Mineral Physics-Basics for Planetology and Geo-Material Science, Elsevier.

Miyahara, M., Kaneko, S., Ohtani, E., Sakai, T., Nagase, T., Kayama, M., Nishido, H., Hirao, N., 2013. Discovery of seifertite in a shocked lunar meteorite. Nat. Commun. 4, 1737. doi:10.1038/ncomms2733

Monkhorst, H.J., Pack, J.D., 1976. Special points for Brillouin-zone integrations. Phys. Rev. B 13, 5188–5192. doi:10.1103/PhysRevB.13.5188

Mosenfelder, J.., Bohlen, S.., 1997. Kinetics of the coesite to quartz transformation. Earth Planet. Sci. Lett. 153, 133–147. doi:10.1016/S0012-821X(97)00159-3

Mosenfelder, J.L., 2000. Pressure dependence of hydroxyl solubility in coesite. Phys. Chem. Miner. 27, 610–617. doi:10.1007/s002690000105

Murakami, M., Hirose, K., Ono, S., Ohishi, Y., 2003. Stability of CaCl2-type and α-PbO2-type SiO2 at high pressure and temperature determined by in-situ X-ray measurements. Geophys. Res. Lett. 30, 1207. doi:10.1029/2002GL016722

M. Veithen, X.G., 2005. Nonlinear optical susceptibilities, Raman efficiencies, and electro-optic tensors from first-principles density functional perturbation theory. Phys Rev B 71, 125107.

Nasdala L., Götze J., Hanchar J.M., Gaft M., and Krbetschek M.R., 2000. Luminescence techniques in Earth sciences. In Beran A. & Libowitzky E. (Eds.): Spectroscopic methods in Mineralogy/EMU Notes in Mineralogy, Vol. 6, Chapter 2, pp43-80. Eötvös University Press, Budapest.

Nasdala L., Smith D., Kaindl R.,and Ziemann M.A. 2000. Raman spectroscopy: Analytical perspectives in mineralogical research. In Beran A. & Libowitzky E. (Eds.): Spectroscopic methods in Mineralogy/EMU Notes in Mineralogy, Vol. 6, Chapter 7, pp 281-329. Eötvös University Press, Budapest.doi:10.1103/PhysRevB.71.125107

Nicholas J.B., Winans R. E, Harrison R. J. Iton L. E. , Curtiss L. A. (1992) An ab initio investigation of disiloxane using extended basis sets and electron correlation. Journal of Physical Chemistry, 96, 7958-7965.

Nukui, A., Yamaoka, S., Nakazawa, H., 1980. Pressure-induced phase transitions in tridymite. Am. Mineral. 65, 1283–1286.

Oberhammer, H., and Boggs, J:E. (1980) Importance of (p-d)π bonding in the siloxane bond. Journal of American Chemical Society, 102, 7241-7244.

Ohtani, E., Ozawa, S., Miyahara, M., Ito, Y., Mikouchi, T., Kimura, M., Arai, T., Sato, K., Hiraga, K., 2011. Coesite and stishovite in a shocked lunar meteorite, Asuka-881757, and impact events in lunar surface. Proc. Natl. Acad. Sci. U. S. A. 108, 463–466. doi:10.1073/pnas.1009338108

Onodera, A., Suito, K., Namba, J., Taniguchi, Y., Horikawa, T., Miyoshi, M., Shimomura, O., Kikegawa, T., 1997. Synchrotron x-ray-diffraction study of α-cristobalite at high pressure and high temperature. High Press. Res. 15, 307–319. doi:10.1080/08957959708240478

Ono, S., Ito, E., Katsura, T., 2001. Mineralogy of subducted basaltic crust (MORB) from 25 to 37 GPa, and chemical heterogeneity of the lower mantle. Earth Planet. Sci. Lett. 190, 57–63. doi:10.1016/S0012-821X(01)00375-2

Oxford Diffraction, CrysAlis CCD, Oxford Diffraction Ltd, Abingdon, England, 2006 .

Palmer, D., Finger, L., 1994. Pressure-Induced Phase-Transition in Cristobalite - an X-Ray-Powder Diffraction Study to 4.4 Gpa. Am. Mineral. 79, 1–8.

Palmer, D., Hemley, R., Prewitt, C., 1994. Raman spectroscopic study of high-pressure phase transitions in cristobalite. Phys. Chem. Miner. 21. doi:10.1007/BF00203922

Parkinson, C.D., 2000. Coesite inclusions and prograde compositional zonation of garnet in whiteschist of the HP-UHPM Kokchetav massif, Kazakhstan: a record of progressive UHP metamorphism. Lithos 52, 215–233. doi:10.1016/S0024-4937(99)00092-4

Pauling, L., 1980. The nature of silicon-oxygen bonds. Am. Mineral. 65, 321–323.

Pauling, L., 1960. The Nature of the Chemical Bond and the Structure of Molecules and Crystals: An Introduction to Modern Structural Chemistry. Cornell University Press.

Payne, M.C., Teter, M.P., Allan, D.C., Arias, T.A., Joannopoulos, J.D., 1992. Iterative minimization techniques for \textit{ab initio} total-energy calculations: molecular dynamics and conjugate gradients. Rev. Mod. Phys. 64, 1045–1097. doi:10.1103/RevModPhys.64.1045

Peacor D.R., 1973. High-temperature single-crystal study of the cristobalite inversion. Z. Kristallogr. 138(1), 274–298.

Perrillat, J.-P., Ricolleau, A., Daniel, I., Fiquet, G., Mezouar, M., Guignot, N., Cardon, H., 2006. Phase transformations of subducted basaltic crust in the upmost lower mantle. Phys. Earth Planet. Inter. 157, 139–149. doi:10.1016/j.pepi.2006.04.001

Prokopenko, V.B., Dubrovinsky, L.S., Dmitriev, V., Weber, H.-P., 2001. In situ characterization of phase transitions in cristobalite under high pressure by Raman spectroscopy and X-ray diffraction. J. Alloys Compd. 327, 87–95. doi:10.1016/S0925-8388(01)01402-5

Pryde, A.K.A., Dove, M.T., 1998. On the Sequence of Phase Transitions in Tridymite. Phys. Chem. Miner. 26, 171–179. doi:10.1007/s002690050174

Putnis, A., 1992. Introduction to mineral sciences. Cambridge University Press, Cambridge.

Rasmussen, B., Fletcher, I.R., Muhling, J.R., 2008. Pb/Pb geochronology, petrography and chemistry of Zr-rich accessory minerals (zirconolite, tranquillityite and baddeleyite) in mare basalt 10047. Geochim. Cosmochim. Acta 72, 5799–5818. doi:10.1016/j.gca.2008.09.010

Rekhi, S., Dubrovinsky, L., Saxena, S., 1999. Temperature-induced ruby fluorescence shifts up to a pressure of 15 GPa in an externally heated diamond anvil cell. High Temp. - High Press. 31. doi:10.1068/htrt161

R. J. Hemley, C.S.Z., 1989. X-ray diffraction and equation of state of solid neon to 110 GPa. Phys. Rev. B Condens. Matter 39, 11820–11827. doi:10.1103/PhysRevB.39.11820

Robinson, K., Gibbs, G., Ribbe, P., 1971. Quadriatic Elongation - Quantitative Measure of Distortion in Coordination Polyhedra. Science 172, 567–&. doi:10.1126/science.172.3983.567

Rohrer, G.S., 2001. Structure and Bonding in Crystalline Materials. Cambridge University Press.

Ross, N.L., 2000. Framework Structures. Rev. Mineral. Geochem. 41, 257–287. doi:10.2138/rmg.2000.41.9

Ruiz-Cruz, M.D., Sanz de Galdeano, C., 2012. Diamond and coesite in ultrahigh-pressure-ultrahigh-temperature granulites from Ceuta, Northern Rif, northwest Africa. Mineral. Mag. 76, 683–705. doi:10.1180/minmag.2012.076.3.17

Sargent, B.A., Forrest, W.J., Tayrien, C., McClure, M.K., Li, A., Basu, A.R., Manoj, P., Watson, D.M., Bohac, C.J., Furlan, E., Kim, K.H., Green, J.D., Sloan, G.C., 2009. Silica in Protoplanetary Disks. Astrophys. J. 690, 1193–1207. doi:10.1088/0004-637X/690/2/1193

Sato, T., Takada, H., Yagi, T., Gotou, H., Okada, T., Wakabayashi, D., Funamori, N., 2013. Anomalous behavior of cristobalite in helium under high pressure. Phys. Chem. Miner. 40, 3–10. doi:10.1007/s00269-012-0540-x

Schaffer, M., Schaffer, B., Ramasse, Q., Falke, M., Abou-Ras, D., Schmidt, S., Caballero, R., Marquardt, K., 2011. Optimized FIB Sample Preparation for Atomic Resolution Analytical STEM at Low kV - A Key Requirement for Successful Application. Microsc. Microanal. 17, 630–631. doi:10.1017/S1431927611004028

Sharma, S., Mammone, J., and Nicol, M. (1981). Raman investigation of ring configurations in vitreous silica. Nature, 292, 140–141.

Sharp, T.G., El Goresy, A., Wopenka, B., Chen, M., 1999. A post-stishovite SiO2 polymorph in the meteorite Shergotty: implications for impact events. Science 284, 1511–1513.

Sheldrick, G.M., 2008. A short history of *SHELX*. Acta Crystallogr. A 64, 112–122. doi:10.1107/S0108767307043930

Shigeaki Ono, K.H., 2002. Post-stishovite phase boundary in SiO 2 determined by in situ X-ray observations. Earth Planet. Sci. Lett. doi:10.1016/S0012-821X(02)00479-X

Smith, David C. 1984. "Coesite in Clinopyroxene in the Caledonides and Its Implications for Geodynamics." Nature 310 (5979): 641–44. doi:10.1038/310641a0.

Smyth, J., Hatton, C., 1977. Coesite-Sanidine Grospydite from Roberts-Victor Kimberlite. Earth Planet. Sci. Lett. 34, 284–290. doi:10.1016/0012-821X(77)90012-7

Smyth, J., Smith, J., Artioli, G., Kvick, A., 1987. Crystal-Structure of Coesite, a High-Pressure Form of Sio2, at 15 and 298 K from Single-Crystal Neutron and X-Ray-Diffraction Data - Test of Bonding Models. J. Phys. Chem. 91, 988–992. doi:10.1021/j100288a043

Smyth, J.R., Jacobsen S.D., and Hazen R.M. (2000). Comparative Crystal Chemistry of Orthosilicate Minerals. In R. Hazen and R. T. Downs, Eds., High-Temperature and High-Pressure Crystal Chemistry, Reviews in Mineralogy & Geochemistry, 41, 187-209.

Sobolev, N.V., Fursenko, B.A., Goryainov, S.V., Shu, J.F., Hemley, R.J., Mao, H.K., Boyd, F.R., 2000. Fossilized high pressure from the Earth's deep interior: The coesite-in-diamond barometer. Proc. Natl. Acad. Sci. U. S. A. 97, 11875–11879. doi:10.1073/pnas.220408697

Syassen, K. (2008). Ruby under pressure, High Pressure Research 28, 75-126

Teter, D.M., Hemley, R.J., Kresse, G., Hafner, J., 1998. High Pressure Polymorphism in Silica. Phys. Rev. Lett. 80, 2145–2148. doi:10.1103/PhysRevLett.80.2145

Thompson, R.M., Downs, R.T., 2010. Packing systematics of the silica polymorphs: The role played by O-O nonbonded interactions in the compression of quartz. Am. Mineral. 95, 104–111. doi:10.2138/am.2010.3241

Tsuchida, Y., Yagi, T., 1990. New pressure-induced transformations of silica at room temperature. Nature 347, 267–269. doi:10.1038/347267a0

Tsuchida, Y., Yagi, T., 1989. A new, post-stishovite highpressure polymorph of silica. Nature 340, 217–220. doi:10.1038/340217a0

Tsuchiya, T., Caracas, R., Tsuchiya, J., 2004. First principles determination of the phase boundaries of high-pressure polymorphs of silica. Geophys. Res. Lett. 31, L11610. doi:10.1029/2004GL019649

Tsuchiya, T., Tsuchiya, J., 2011. Prediction of a hexagonal SiO2 phase affecting stabilities of MgSiO3 and CaSiO3 at multimegabar pressures. Proc. Natl. Acad. Sci. U. S. A. 108, 1252–1255. doi:10.1073/pnas.1013594108

Van Valkenburg A Jr, Buie BF, 1945 Octahedral cristobalite with quartz paramorphs from Ellora Caves, Hyderabad State, India. American Mineralogist 30, 526-535

Veithen, M., Gonze, X., and Ghosez, Ph. (2005) Non-linear optical susceptibilities, Raman efficiencies and electrooptic tensors from first-principles density functional perturbation theory. Physical Reviews B, 71, 125107.

C. A. Volkert and A. M. Minor. 2007. Focused Ion Beam Microscopy and Micromachining. MRS Bulletin, 32(05):389–399,

Weber, I., Greshake, A., Bischoff, A., 2000. Low-Cristobalite in the Martian Meteorite Zagami, in: Lunar and Planetary Science Conference. Presented at the Lunar and Planetary Science Conference, p. 1342.

Wentzcovitch, R., Da Silva, C., Chelikowsky, J., Binggeli, N., 1998. A new phase and pressure induced amorphization in silica. Phys. Rev. Lett. 80, 2149–2152. doi:10.1103/PhysRevLett.80.2149

Williams D. B.and Carter C. B.. Transmission electron microscopy: a textbook for materials science. Springer, 1996. ISBN 9780306452475.

Williams, Q., Hemley, R., Kruger, M., Jeanloz, R., 1993. High-Pressure Infrared-Spectra of Alpha-Quartz, Coesite, Stishovite and Silica Glass. J. Geophys. Res.-Solid Earth 98, 22157–22170. doi:10.1029/93JB02171

Wyckoff, R.W.G. (1963) Crystal Structures 1, 2nd edition. Interscience Publishers, New York, New York, 7-83

Xavier Gonze, G.R., 2005. First-principle studies of the lattice dynamics of crystals, and related properties. Z. Für Krist. 220, 458–472. doi:10.1524/zkri.220.5.458.65077

Xiao, W., Chen, M., Xie, X., 2011. Shock-Produced Coesite in the Xiuyan Crater, China. Meteorit. Planet. Sci. 46, A256–A256.

Xu, J., Mao, H., Bell, P., 1986. High-Pressure Ruby and Diamond Fluorescence - Observations at 0.21 to 0.55 Terapascal. Science 232, 1404–1406. doi:10.1126/science.232.4756.1404

Yagi, T., Yamakata, M., 2000. Effect of hydrostaticity on the phase transformations of cristobalite. Phys. Meets Mineral. 242–255.

Yahagi, Y., Yagi, T., Yamawaki, H., Aoki, K., 1994. Infrared-Absorption Spectra of the High-Pressure Phases of Cristobalite and Their Coordination Numbers of Silicon Atoms. Solid State Commun. 89, 945–948. doi:10.1016/0038-1098(94)90357-3

Yang, R., Wu, Z., 2014. Elastic properties of stishovite and the CaCl2-type silica at the mantle temperature and pressure: An ab initio investigation. Earth Planet. Sci. Lett. 404, 14–21. doi:10.1016/j.epsl.2014.07.020

Zha, C.S., Mao, H.K., Hemley, R.J., 2000. Elasticity of MgO and a primary pressure scale to 55 GPa. Proc. Natl. Acad. Sci. U. S. A. 97, 13494–13499. doi:10.1073/pnas.240466697

(Eidesstattliche) Versicherungen und Erklärungen

(§ 8 S. 2 Nr. 6 PromO)

Hiermit erkläre ich mich damit einverstanden, dass die elektronische Fassung meiner Dissertation unter Wahrung meiner Urheberrechte und des Datenschutzes einer gesonderten Überprüfung hinsichtlich der eigenständigen Anfertigung der Dissertation unterzogen werden kann.

(§ 8 S. 2 Nr. 8 PromO)

Hiermit erkläre ich eidesstattlich, dass ich die Dissertation selbständig verfasst und keine anderen als die von mir angegebenen Quellen und Hilfsmittel benutzt habe.

(§ 8 S. 2 Nr. 9 PromO)

Ich habe die Dissertation nicht bereits zur Erlangung eines akademischen Grades anderweitig eingereicht und habe auch nicht bereits diese oder eine gleichartige Doktorprüfung endgültig nicht bestanden.

(§ 8 S. 2 Nr. 10 PromO)

Hiermit erkläre ich, dass ich keine Hilfe von gewerblichen Promotionsberatern bzw. -vermittlern in Anspruch genommen habe und auch künftig nicht nehmen werde.

Bayreuth, 19.12.2015

……

Ort, Datum, Unterschrift